Mechanical Behavior of Shell Casing and Separator of Lithium-ion Battery

by

Xiaowei Zhang

B.S., Automotive Engineering, Tsinghua University, Beijing (2009)
M.S., Mechanical Engineering, Tsinghua University, Beijing (2012)

Submitted to the Department of Mechanical Engineering
in partial fulfillment of the requirements for the degree of

Doctor of Philosophy in Mechanical Engineering

at the

MASSACHUSETTS INSTITUTE OF TECHNOLOGY

June 2017

MASSACHUSETTS INSTITUTE OF TECHNOLOGY
JUN 21 2017
LIBRARIES
ARCHIVES

©Massachusetts Institute of Technology 2017. All rights reserved.

Author..... Signature redacted .....
Department of Mechanical Engineering
March 31, 2017

Certified by.... Signature redacted .....
Tomasz Wierzbicki
Professor of Applied Mechanics
Thesis Supervisor

Certified by..... Signature redacted .....
Elham Sahraei
Assistant Professor of Mechanical Engineering, GMU
Thesis Supervisor

Accepted by..... Signature redacted .....
Rohan Abeyaratne
Chairman, Committee on Graduate Students, Mechanical Engineering

Zhuhai CosMX Battery Co. - EX1007
Zhuhai CosMX Battery Co. v. Ningde Amperex Tech. Ltd.

Mechanical Behavior of Shell Casing and Separator of Lithium-ion Battery

Xiaowei Zhang
Submitted to the Department of Mechanical Engineering
On March 31, 2017, in partial fulfillment of the requirements for the degree of
Doctor of Philosophy in Mechanical Engineering

Abstract

With the rapid growth of electric vehicle (EV) market, the mechanical safety of lithium-ion batteries has become a critical concern for car and battery manufacturers as well as the public. Lithium-ion battery cells consist of cathode, anode, separator and shell casing or aluminum plastic cover. Among them, the shell casing provides substantial strength and fracture resistance under mechanical loading, and the failure of the separator determines onset of internal short circuit of the cell. In the first part of this thesis, a plasticity and fracture model of the battery shell casing by taking the anisotropic plasticity and stress-state dependent fracture into account was developed. The shell casing model is calibrated and validated at both specimen and component levels. This shell casing model, together with homogenized jellyroll model could predict mechanical behavior of single cylindrical 18650 cell well and could serve for battery pack crash simulation purposes. Another part of this thesis is mechanical test, characterization and modeling of battery separators since the mechanical properties of separators are crucial to internal shorts of lithium-ion batteries. Mechanical properties of commercially available four typical separators that including polypropylene (PP), trilayer (PP-PE-PP), ceramic-coated and nonwoven separators were compared, such as in-plane tensile strength, out-of-plane compression strength and puncture strength. Two distinct failure modes of dry-processed separators under biaxial loading were observed in the tests and used to explain the differences in short circuit characteristics of same cells. A conservative defection-based failure criterion for predicting of onset of short from experimental data was proposed. Numerical model of separator was developed and it succeeded in predicting the response of PP separator under biaxial loading. Owing to the micro porous semi-crystalline nature of widely used PP separator, interrupted tests of PP separator under different in-plane tension including machine direction, transverse direction and diagonal direction were conducted in order to reveal deformation mechanism at the micrometer level. Through scanning electric microscopy (SEM) observation and X-ray diffraction of deformed regions from interrupted test specimens, deformation sequences of micro fibrils and lamellae blocks of PP separator are reported. Lastly, significant mechanical degradation of separator due to charge-discharge cycling was described.

Thesis Supervisor: Tomasz Wierzbicki
Title: Professor of Applied Mechanics

Thesis Supervisor: Elham Sahraei
Title: Assistant Professor of Mechanical Engineering, George Mason University

Acknowledgements

I would like to thank my advisor, Professor Tomasz Wierzbicki, for his continuous guidance and support through the years of my stay at MIT in the Impact and Crashworthiness Lab. I really appreciate the trust he gave to me in these years, especially the first two years when I was struggling with course, research and language. Many thanks are due to my co-advisor, Professor Elham Sahraei, for her insightful suggestions and crucial guidance. I am grateful to my committee members, Professor David Parks and Professor Xuanhe Zhao for their constructive comments.

It has been a great pleasure for me to work in ICL. I would like to thank all the members of ICL for their kind supports: Dr. Kai Wang, Dr. Stephane Marcadet, Dr. Yong Xia, Dr. Marcelo Paredes, Dr. Matthieu Dunand, Dr. Meng Luo, Dr. Kirki Kofiani, Dr. Seung Hyun Chung, Dr. Maysam Gorji, Mr. Keunhwan Pack, Mr. Colin Bonatti, Mr. Rami Abi Akl, Mr. Juner Zhu, Mr. Thomas Tancogne-Dejean, Mr. Hailing Luo, LT Brandy Dixon, LCDR Joseph Meier, LCDR Sagy Hakoon, LCDR Amber Mason. Special thanks to Barbara Smith for her assistance and inspiration of her colorful life.

I am grateful to all the members of MIT battery consortium for their financial support and regular feedback. Special thanks to Boston-Power for providing battery cells.

Finally, I would like to express my deepest thanks to my family for their unconditionally love and support, and to my wife, Xueliu Fan, without her, my life will be much harder.

Contents

1. Introduction 21

1.1 Plasticity and fracture model of shell casing 24

1.2 Mechanical properties of battery separators 26

1.3 Thesis outline 29

2. Test and Modeling of 18650 Shell Casing 33

2.1 Introduction 33

2.2 Plasticity modeling for the battery shell casing 34

2.2.1 Material 35

2.2.2 Description of the test method and preparation of the specimens 37

2.2.3 Calibration of Hill's 48 anisotropic plasticity model 41

2.2.4 Determination of hardening curve before and after necking 42

2.3 Fracture modeling for the battery shell casing 44

2.3.1 Introduction of Modified Mohr-Coulomb fracture model 44

2.3.2 Calibration of the MMC fracture model 46

2.4 Validation of the plasticity and fracture model at the "structural" level 52

2.4.1 Axial compression test 52

2.4.2 Lateral compression test 53

2.4.3 Three-point bending test 55

2.4.4 Internal pressure test 56

2.5 Discussion on different types of shear specimens 58

2.6 Application 59

2.7 Conclusion 63

3. Deformation and Failure Characteristics of Four Types of Lithium-ion Battery Separators 65

3.1 Introduction 65

3.2 Experimental methods and results 67

3.2.1 Tensile tests 67

3.2.2 Compression tests 71

3.2.3 Biaxial punch tests 73

3.3 Two failure modes in biaxial punch loading 77

3.4 Discussion on formation of distinct short circuits 79

3.5 Conclusion 82

4. Deformation Mechanism and Numerical Modeling of Dry-processed PP Separator 85

4.1 Introduction 85

4.2 Strain rate and thermal properties of PP separator 86

4.3 Chemical bond characterization and crystalline orientation 89

4.4 Micro fibril deformation sequence under uniaxial loading 91

4.5 Structural anisotropy vs. material anisotropy 111

4.6 Fibril deformation under out-of-plane compression 112

4.7 Finite Element Modeling of PP Separator 113

4.8 Summary 117

5. Mechanical Degradation of Battery Separators Under Charge-Discharge Cycles 119

5.1 Introduction 119

5.2 Experimental 120

5.3 Results and Discussion 122

5.4 Concluding Remarks 130

6. Summary and Future Directions 131

6.1 Summary of main results 131

6.2 Future research 133

6.2.1 Numerical modeling of the separator with other types of modeling strategy 133

6.2.2 Test and modeling of electrodes 134

6.2.3 Coupling of thermal and electrochemical properties 134

6.2.4 Solid state battery study 134

7. Bibliography 135

List of Figures

Figure 1-1 Evolution of the global electric car stock, 2010-15 (Courtesy of IEA [4], © OECD/IEA 2016 Global EV Outlook, IEA Publishing. License: www.iea.org/t&c) 22

Figure 1-2 An electric vehicle after fire accident (courtesy of ref [7]) 23

Figure 1-3 Components of battery cell 23

Figure 1-4 Cross section view of cathode and anode, middle layer is aluminum and copper foil respectively. (a) cross section of cathode; (b) cross section of anode 23

Figure 1-5 Three-point bending test setup (left) and force deflection curve (right) [8]. Reproduced with permission. © 2013 Elsevier Ltd 25

Figure 1-6 Separator rolls of Celgard (left: courtesy of celgard.com) and ceramic-coated separators (right: courtesy of celgard.com). © Celgard.com, 2017 26

Figure 1-7 Manufacturing process of polymeric separators. (a) extrusion and film blowing process (courtesy of ref [41], with permission. Copyright © 2007, Elsevier); (b) cold and hot strecthing; (c) wet-processed maching process; (d) SEM of dry-processed separator (courtesy of ref [39]); (e) SEM of wet-processed separator (courtesy of ref [39]). Reproduced with permission. Copyright © 2004, American Chemical Society 27

Figure 2-1 Illustration of a typical deep drawing process 35

Figure 2-2 Non-uniform thickness distribution of the shell casing. (a) position in casing; (b) thickness distribution chart 36

Figure 2-3 Corroded shell casing after 3 months exposure to water 37

Figure 2-4 Specimen preparation from the flatted shell casing in different material orientations (0°, 45° and 90° to the deep drawing direction) 38

Figure 2-5 Geometry of the dogbone specimen (dimension in mm) and specimens before test. (a) along axial, diagonal direction (left) and hoop direction (right); (b) specimens along axial (left), diagonal (middle) and hoop direction (right) 38

Figure 2-6 Engineering stress versus strain curve (left) and fractured dogbone specimens (right) 39

Figure 2-7 Geometry of the window-shaped specimen (left) and uniaxial tension test setup (right) 40

Figure 2-8 Comparison of stress-strain curves of uniaxial tension (left) and fractured window-shape specimen (right) 40

Figure 2-9 Swift law and Voce law fitting of hardening curve 43

Figure 2-10 FE model of notched specimen 44

Figure 2-11 Prediction of force-displacement with Swift law, Voce law and optimized hardening curve for notched specimen 44

Figure 2-12 Specimens designed for MMC model calibration: (a) notched specimen; (b) specimen with central hole; (c) butterfly tensile specimen; (d) punched specimen; (e) simple shear specimen 48

Figure 2-13 Comparison of force-displacement curves between test and simulation: (a) notched specimen; (b) specimen with central hole; (c) butterfly tension specimen; (d) punch specimen; (e) simple shear specimen 51

Figure 2-14 The MMC fracture envelopes for battery shell casing 51

Figure 2-15 Concertina folding of shell casing (left) and force-displacement curve of axial compression of shell casing (right) 53

Figure 2-16 Force-displacement of lateral compression of shell casing 54

Figure 2-17 Models with or without endcap 54

Figure 2-18 Sequence of lateral compression (contour: Mises stress) 54

Figure 2-19 Test setup of three-point bending test and force-displacement curve 55

Figure 2-20 Deformation of open end of the shell casing (contour: Mises stress) 55

Figure 2-21 Setup of hydraulic bulge test 57

Figure 2-22 Assemble of the piston 57

Figure 2-23 Force-displacement curve of hydraulic bulge test 57

Figure 2-24 Pressure load of FE model 57

Figure 2-25 Comparison of fracture in test and simulation (contour: plastic equivalent strain) 57

Figure 2-26 Local buckling of butterfly shear specimen 59

Figure 2-27 Local buckling of torsion specimen in simulation (contour: plastic equivalent strain) 59

Figure 2-28 Concept design of anti-buckling device for torsion test 59

Figure 2-29 Simple shear specimen with geometry scaled from Reyes et al. [62] 59

Figure 2-30 Comparison of force-displacement curve of simple shear test 59

Figure 2-31 Stress-strain curve of jellyroll 61

Figure 2-32 Comparison of test and simulation of three-point bending test of 18650 battery 62

Figure 2-33 Bending of (a) jellyroll only, (b) shell casing only, (c) whole battery 62

Figure 2-34 Comparison of test and simulation of indentation test of 18650 battery 62

Figure 2-35 Indentation of (a) jellyroll only, (b) shell casing only, (c) whole battery 62

Figure 3-1 (a) Illustration of MD, TD, +DD, -DD a separator roll; nominal stress-strain of (b) dry-processed PP separator, (b) dry-processed trilayer separator, (c) wet-processed ceramic-coated separator, (e) nonwoven separator in the four directions 68

Figure 3-2 Comparison of failure strain and failure mode in MD, TD, DD in uniaxial tensile test. (a) comparison of fracture strain; (b) different failure modes in MD, TD, and DD (from left to right) 71

Figure 3-3 Compression test experiment. (a) test setup and image from DIC camera; (b) specimen before test; (c) PP separator after test; (d) ceramic-coated separator after test 72

Figure 3-4 Nominal stress strain curves of the four separators 73

Figure 3-5 Biaxial punch test setup. (a) teflon punch head with diameter of 25.4 mm, 12.7 mm, 6.4 mm and 3.2 mm (from left to right); (b) biaxial loading fixture 75

Figure 3-6 Force-displacement curves of punch test (a) PP, (b) trilayer, (c) ceramic coated, (d) nonwoven and separators after failure (e) PP, (f) trilayer, (g) ceramic coated, (h) nonwoven (punch head diameter: 1/4 inch) 76

Figure 3-7 SEM image and Photos of separators under punch loading. (a) SEM image of PP separator; (b) Mode A Failure; (c) Mode B Failure; (d) additional views of transparent area before failure in Mode B 77

Figure 3-8 Force-displacement curves from punch loading of PP and trilayer separators with different punch sizes. (a) PP separator; (b) trilayer separator..... 79

Figure 3-9 A hard short easily detected at 3 mm displacement (a), original global curve; versus a soft short at 1.5 mm displacement (b), zoomed voltage 80

Figure 3-10 Short circuit area due to Mode A failure (a) left, versus the area in a Mode B Failure (b) right 81

Figure 3-11 Onset of thinning and formation of transparent area in the PP separator 82

Figure 4-1 Market size prediction of wet and dry-processed separator in China (data from qb-lib.com)..... 85

Figure 4-2 Strain rate effect in MD, TD and DD of PP separator. (a) MD; (b) TD; (c) DD; (d) summary of strain rate effect..... 87

Figure 4-3 Stress strain curve of PP separator in MD, TD and DD under different temperatures. (a) MD; (b) TD; (c) DD..... 88

Figure 4-4 Temperature dependence of storage modulus, loss modulus and tangent delta in MD and TD. (a) MD; (b) TD..... 89

Figure 4-5 FTIR spectrum of PP separator, matched well with isotactic PP spectrum 90

Figure 4-6 Wide and small angle X-ray diffraction. (a) wide angle XRD; (b) small angle XRD 91

Figure 4-7 Lorentz corrected WAXS intensity profile 91

Figure 4-8 SEM micrograph of PP separator of surface and through thickness view. (a) 3D view of separator film; (b) surface SEM (different scale bar); (c) cross section view along MD (different scale bar, ND is normal direction); (d) cross section view along TD (different scale bar, ND is normal direction) 93

Figure 4-9 Fracture due to beam damage 94

Figure 4-10 SEM samples from interrupt test specimens 94

Figure 4-11 Interrupted test setup (250-N grip and 100-N load cell) and loading profile with loading and unloading speed 25 min/min 94

Figure 4-12 Force-displacement curves of interrupted test along MD 95

Figure 4-13 SEM micrograph of interrupted tests along MD with different maximum strains and scale bars. (a) engineering strain = 2.9%; (b) engineering strain = 8.6%; (c) engineering strain = 22.9%; (d) engineering strain = 34.3%; (e) engineering strain = 45% (fractured) 97

Figure 4-14 Wide and small X-ray scattering of interrupted tests along MD with different maximum strains and scale bars. (a) engineering strain = 2.9%; (b) engineering strain = 8.6%; (c) engineering strain = 22.9%; (d) engineering strain = 34.3%; (e) engineering strain = 45% (fractured) 98

Figure 4-15 Force-displacement curves of interrupted test along TD 99

Figure 4-16 SEM micrograph of interrupted tests along TD with different maximum strains and scale bars. (a) engineering strain = 1.4%; (b) engineering strain = 2.7%; (c) engineering strain = 5.7%; (d) engineering strain = 11.4%; (e) engineering strain = 22.8%; (f) engineering strain = 34.2%; (g) engineering strain = 62.8% (fractured) 101

Figure 4-17 Wide and small X-ray scattering of interrupted tests along TD with different maximum strains and scale bars. (a) engineering strain = 1.4%; (b) engineering strain = 2.7%; (c) engineering strain = 5.7%; (d) engineering strain = 11.4%; (e) engineering strain = 22.8%; (f) engineering strain = 34.2%; (g) engineering strain = 62.8% (fractured) 104

Figure 4-18 Force-displacement curve of interrupted test along DD 104

Figure 4-19 SEM micrograph of interrupted tests along TD with different maximum strains and scale bars. (a) engineering strain = 2.9%; (b) engineering strain = 11.4%; (c) engineering strain = 22.8%; (d) engineering strain = 34.2%; (e) engineering strain = 51.4%; (f) engineering strain = 60% (fractured)..... 106

Figure 4-20 Wide and small X-ray scattering of interrupted tests along TD with different maximum strains and scale bars. (a) engineering strain = 2.9%; (b) engineering strain = 11.4%; (c) engineering strain = 22.8%; (d) engineering strain = 34.2%; (e) engineering strain = 51.4%; (f) engineering strain = 60% (fractured) 108

Figure 4-21 Localization of microstructures in DD tensile. (a) engineering strain = 2.9%; (b) engineering strain = 34.2%; 109

Figure 4-22 Illustration of the deformation sequences of fibrils and lamellae under MD, TD and DD loading. (a) original; (b) under MD loading; (c) under TD loading; (d) under DD loading..... 110

Figure 4-23 Structural anisotropic study. (a) 2D reconstruction of PP separator (SEM picture from ref [39]. Reproduced with permission. Copyright © 2004, American Chemical Society); (b) 3D reconstruction of PP separator 112

Figure 4-24 SEM micrograph after out-of-plane compression..... 113

Figure 4-25 Simulation of uniaxial tensile and compressive loading of separators. (a) tensile loading in TD and MD; (b) tensile loading in DD; (c) through-thickness compression 115

Figure 4-26 Punch loading simulation and comparison with test: (a) punch test simulation with different punch size; (b) comparison between test and simulation with different punch heads..... 116

Figure 4-27 Side-view comparison between test and simulation from vertical planes along MD and TD 117

Figure 5-1 Volume change cycled cell compared with new cell 121

Figure 5-2 Battery components after 1200 cycles 121

Figure 5-3 Punch test setup with a teflon punch head of 12.7 mm in diameter..... 122

Figure 5-4 Engineering stress-strain curve of separators with different cycles in MD, TD and DD. (a) MD; (b) TD; (c) DD 123

Figure 5-5 Punch test results for separators with different punch size. (a) punch diameter: 25.4 mm; (b) punch diameter: 12.7 mm; (c) punch diameter: 6.4 mm; (d) punch diameter: 3.175 mm; (e) normalized failure force vs cycle number for different punch head sizes 125

Figure 5-6 Lateral indentation results of cells with 0 and 1200 cycles 126

Figure 5-7 SEM pictures of a fresh (0 cycled) separator. (a) structure of a fresh (0 cycled) separator; (b) surface SEM of 0 cycled separator (PP layer); (c) cross-section view of PP and PE layer of 0 cycled separator along MD; (d) cross-section view of PP layer 0 cycle 127

Figure 5-8 SEM picture of 0 and 1200 cycled separators. (a) cross-section view of PP and PE layer of 1200 cycled separator along MD; (b) cross-section view of PP layer 1200 cycled separator along MD; (c) cross-section view of PE layer of 1200 cycled separator along MD (particle in circle); (d) cross-section view of PE layer 1200 cycled separator along TD (particle in circle) 128

Figure 5-9 Wide angle XRD images of (a) separator with 0 cycle and (b) separator with 1200 cycles 129

Figure 5-10 FTIR spectrum of 0 and 1200 cycled separators 130

List of Tables

Table 2-1 Chemical composition of the shell casing 37

Table 2-2 Hill'48 coefficients determined from Lankford coefficient 41

Table 2-3 Lankford coefficients determined from uniaxial tensile test 42

Table 2-4 Combined Swift and Voce hardening law parameters 44

Table 2-5 Parameters of jellyroll model 61

Table 3-1 Separator specifications 67

Chapter 1

Introduction

The rapid increase in power and energy density of lithium-ion batteries makes the lithium-ion battery wide spread in the consumer electronics since the introduction of the first commercialized cell by Sony in 1991 [1–3]. After the release of GM EV1 and especially, Tesla Roadster and Model S, the electric vehicle market is blooming. The Tesla Model S showed the world the great capability of small 18650 cylindrical rechargeable lithium-ion cells and proved the simplicity and excellent acceleration performance that electric vehicles could achieve. At the moment of this thesis, almost all the major automotive manufacturers have their battery electric vehicle (EV) models either on market or planned to release in near future, such as GM's Bolt, Volkswagen's e-Golf, Ford's Focus Electric, Nissan's Leaf, Tesla's Model S, Model X and Model 3, Mitsubishi's I-Miev, BMW's I series, Mercedes-Benz's B class, BYD Qin, as well as new models from startups, Faraday Future 91, Lucid Air. As shown in Figure 1-1, the China, US, Western Europe and Japan markets are the biggest EV markets due to the facts of global warming, requirement of sustainable development and reduction of fossil fuel consumption as well as strong supports from governments [4,5]. The prediction of the EV market in coming years indicates exponentially growth of annual sale and will reach to 35% of global new car in production [6].

However, with the development of electric vehicle market, the safety of lithium-ion battery has become a critical concern for the industry and the media. Figure 1-2 shows a vehicle after fire accident of battery [7]. Due to lack of the knowledge of battery cells' mechanical performance under crash loading, all the EV companies put their battery packs under passenger seat which are believed to be outside the crumple zone. However, this would constrain the car body design, the Environmental Protection Agency (EPA)-rated range and further light weighting. Most of the researchers in the lithium-ion battery community are working on improving the electrochemical properties of the battery, ie, increasing the energy density, power density and charge-discharge cyclic ability. Meanwhile very few

research groups from academia are working on testing and modeling the mechanical behavior of the cells or their components. Those groups mainly include MIT's Wierzbicki's lab, Princeton University's Arnold's lab, University of Michigan's Pan's group and Michigan state university's Xiao's group [8–16]. All these groups are still focusing on testing the battery components and developing homogenized modeling of the cells, and applicable material models for battery components are slowly emerging.

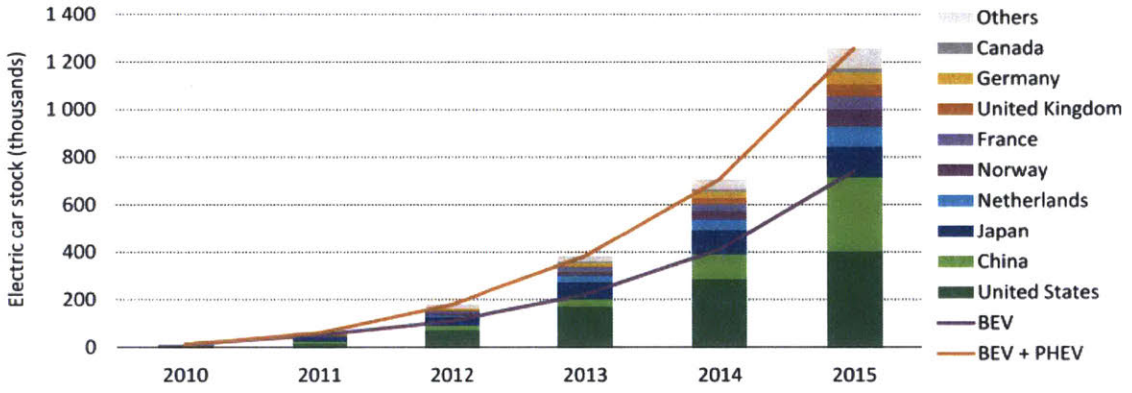


Figure 1-1 Evolution of the global electric car stock, 2010-15 (Courtesy of IEA [4], © OECD/IEA 2016 Global EV Outlook, IEA Publishing. License: www.iea.org/t&c)

Lithium-ion battery cell consists of cathode, anode, separator, electrolyte and shell casing or plastic cover as shown in Figure 1-3. The cathode is a double-side active-particle ($LiNi_xMn_yCo_zO_2$, etc) coated aluminum thin film, where central aluminum foil works as current collector and determines the total in-plane mechanical strength of cathode, as shown in Figure 1-4a [17]. The copper current collector works the same way in graphite-coated anode in terms of in-plane mechanical strength, as shown in Figure 1-4b. Most commonly used lithium-ion battery separators are porous polymeric films, such as polyethylene (PE) and polypropylene (PP) or their combination (trilayer PP-PE-PP) with a thickness of $16\sim30\ \mu m$. The separator works as an electron barrier between cathode and anode to prevent internal short circuit of lithium-ion battery. Tearing and failure of separator could lead to thermal runway of the cell and potential fire accidents. The shell casing of prismatic or cylindrical cells with a thickness of around 0.3 mm provides substantial strength and fracture resistance under mechanical loading.



Figure 1-2 An electric vehicle after fire accident (courtesy of ref [7])

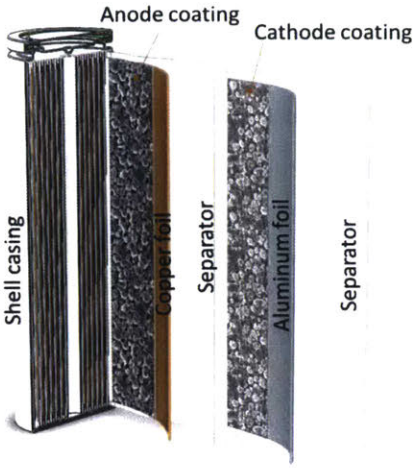
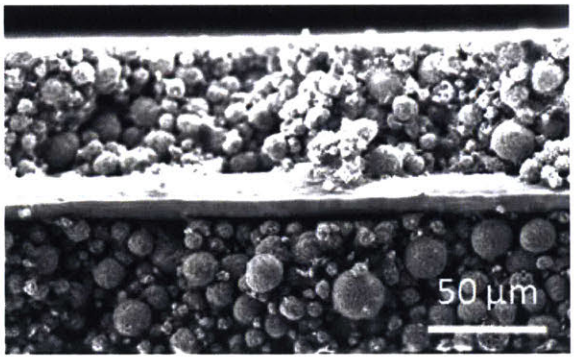
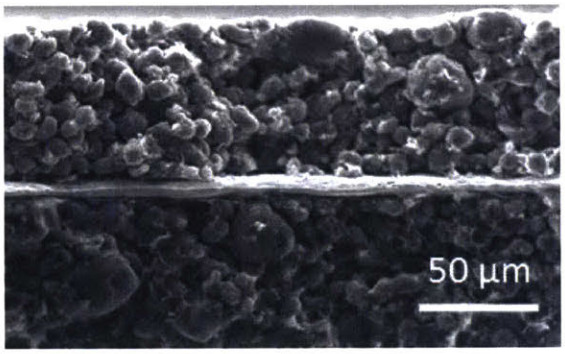


Figure 1-3 Components of battery cell



(a)



(b)

Figure 1-4 Cross section view of cathode and anode, middle layer is aluminum and copper foil respectively. (a) cross section of cathode; (b) cross section of anode

The components of cell can be classified into two groups based on their functionalities. The cathode and anode are directly related the electrochemical performance of the cell, such as power density and energy density. The separator and shell casing are mainly responsible for mechanical integrity and safety. The objective of this thesis is mechanical testing and modeling of the shell casing and separator, which are largely related to mechanical safety. The battery components have multi-scale features: the shell casing, the

cathode and anode have lengths of hundreds millimeters (100 mm) and a thickness of less than hundreds micrometers (100 μm). To make things more complicated, the cathode, anode and separator themselves have either micro particles or micro fibrils inside. As shown in Figure 1-4 and Figure 1-6, the particles size of the cathode and anode coating is 10 μm and the size of pores in the separator is around 100 nm, which is around nine-order difference to its length (100 mm). Thus, it requires great efforts to understand the deformation mechanisms in such a different length scales, which is the main challenge of this thesis.

1.1 Plasticity and fracture model of shell casing

As mentioned above, the shell casing carries the majority loading when a cell is under mechanical loading/deformation. Figure 1-5 shows a sudden drop in force when the shell casing fractured under three-point bending test. After its failure, the cell took much less load and shortly went to internal shorts [9]. To obtain the plasticity properties of cylindrical shell casing, researchers usually cut and flattened the casing first and then conduct uniaxial tensile tests. They took the shell casing as an isotropic material and assumed a constant fracture strain value when they create finite element models of a battery cell for crash simulation purposes [9,18]. However, unlike the widely-seen sheet metal, the shell casing is usually made of deep-drawn process, which is very thin and has significant manufacturing-induced anisotropy. Due to this process, final thickness of the shell casing is different from position to position, which will be shown in detail in Chapter 2. Several points need to be checked here: 1), if the flattening process brings pre-damage effects during the preparation of the uniaxial tensile specimen, ie, dogbone specimen; 2), how to consider the anisotropic properties; 3), how to determine the fracture locus.

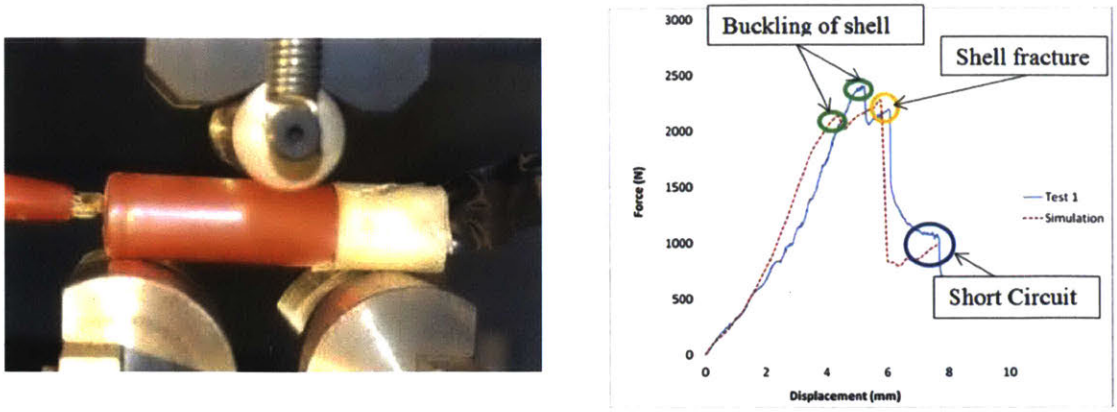


Figure 1-5 Three-point bending test setup (left) and force deflection curve (right) [8]. Reproduced with permission. © 2013 Elsevier Ltd

The work here is on prediction of ductile failure of shell casing. Fracture prediction of ductile metals has been intensively studied over the past several decades with the strong demands from sheet metal forming and crash analysis field. The fracture models can be roughly classified into two types: micromechanics-based Gurson type models and phenomenological models. The former class takes the void growth, nucleation and coalescence into account, by saying that fracture starts when critical void volume fraction reached. The pioneer works were done by McClintock [19], Rice and Tracey [20], Gurson [21] and later, the model was modified by Tvergaard and Needleman [22], Nahshon and Hutchinson [23] to enhance the prediction of original Gurson model for void coalescence and shear damage (the micromechanics mechanism no longer holds for Nahshon and Hutchinson's modification [24]). Among the phenomenological fracture models, a popular one was developed through Bao and Wierzbicki's experimental observation of the stress triaxility (ratio of hydrostatic stress over von Mises stress) depended fracture strain [25], and introduction the effect of third stress invariant (Lode angle) by Xue [26] and later interpretation of Mohr-Coulomb model in mixed strain space with so called Modified Mohr-Coulomb model (MMC) by Bai and Wierzbicki [27]. There are also empirical models, such as Johnson-Cook kinds of model [28].

The comparison of the prediction of these model were nicely done by Dunand and Mohr [29] and Bai and Wierzbicki [30]. In this thesis, the MMC fracture model is used because of its ability of prediction and simplicity of calibration [31–36]. The so called 18650 cell has a height

of 65 mm, a diameter of 18 mm and an average thickness of 0.26 mm, which brings significant difficulties in designing and testing specimens from this relatively small casing.

1.2 Mechanical properties of battery separators

The separator is another important component inside a lithium-ion battery, which lays in between cathode and anode in Figure 1-3 and Figure 1-6. It allows free transfer of electrolyte and lithium-ion and works as a barrier for electrons. The failure of separator may lead to catastrophic failure of cells, such as the recent global recall of Samsung's Galaxy Note 7. An ideal separator should have infinite electronic resistivity, zero ionic resistance and be infinitely thin and strong. There are several critical parameters for separators, such as pore size, permeability, thermal and chemical stability, electrochemical properties and mechanical strength together with different characterization techniques [37,38]. Four different types of separators are currently used in the market: conventional polymeric microporous membranes (mostly used), nonwoven mat separators, composite membrane where inorganic particles are coated outside and electrolyte membranes (for solid state lithium-ion cell) [39–41]. The conventional polymeric separators are mode from either dry process or wet process, where dry-processed one is highly anisotropic (strength level in machine direction (rolling direction) is much higher than that in transverse direction) and wet-processed one is close to isotropic (strength levels are comparable along these two directions.

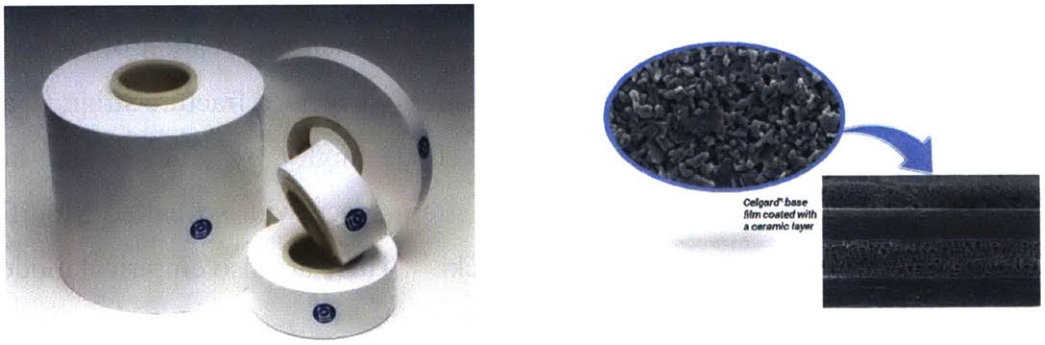


Figure 1-6 Separator rolls of Celgard (left: courtesy of celgard.com) and ceramic-coated separators (right: courtesy of celgard.com). © Celgard.com, 2017

It is still worth mentioning the manufacturing process of battery separators in certain detail since it brings significant differences to final products. Majority of related references are seen in patents, for example, patents filed by Celgard LLC, one of the biggest battery separator suppliers. Figure 1-7 shows the dry and wet manufacturing processes and their corresponding SEM images of micro structures [41–46]. The commonly used polymeric separators are either made from polyethylene (PE) or polypropylene (PP). The manufacturing process for dry-processed separators starts with melt and extrusion of

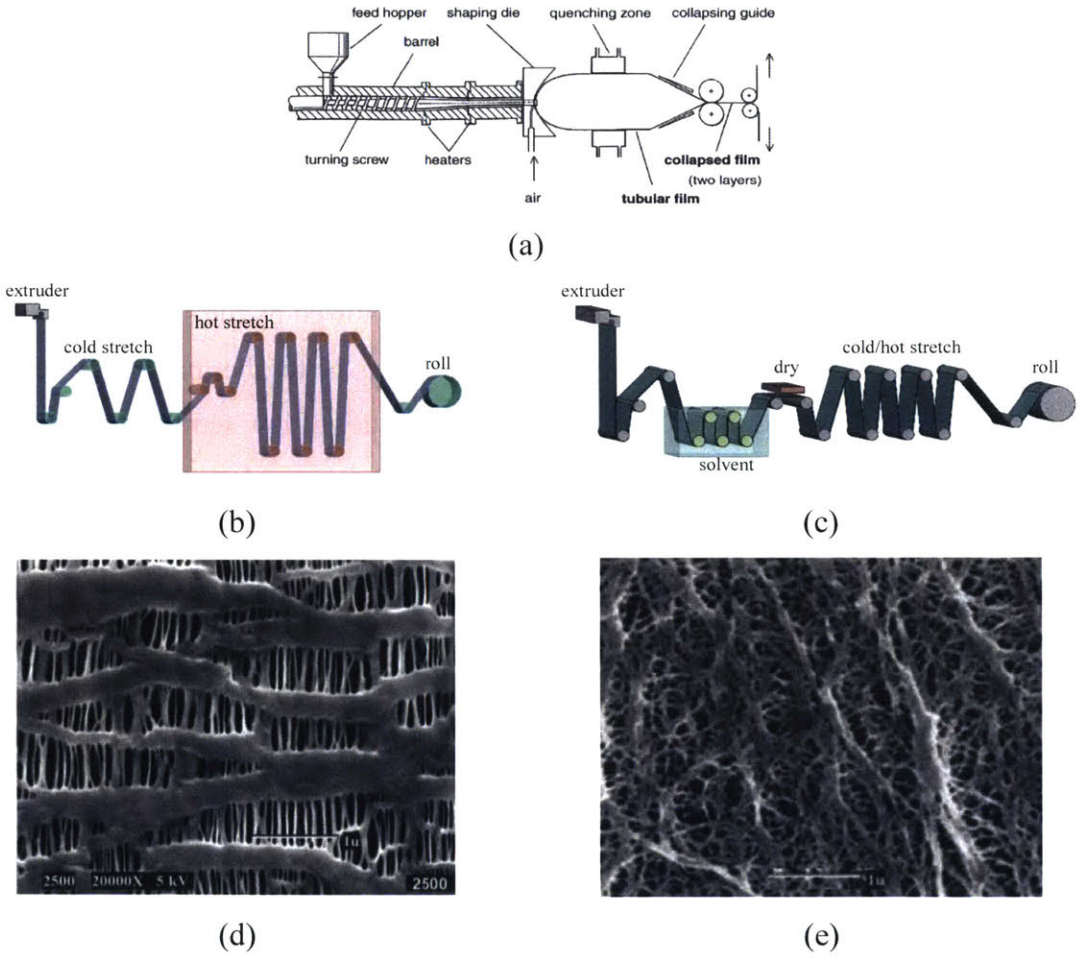


Figure 1-7 Manufacturing process of polymeric separators. (a) extrusion and film blowing process (courtesy of ref [41], with permission. Copyright © 2007, Elsevier); (b) cold and hot strecthing; (c) wet-processed maching process; (d) SEM of dry-processed separator (courtesy of ref [39]); (e) SEM of wet-processed separator (courtesy of ref [39]). Reproduced with permission. Copyright © 2004, American Chemical Society

PP or PE resin, as seen in Figure 1-7a-c. Then the non-porous precursor film with regular orientation and alignment of crystal lamellae is obtained from either film blowing process or cast film extrusions. According to Tabatabaei et al. [47], cast film extrusion could offer better thickness uniformity, which is preferable for generation of desired pore size distribution during later stretching process. The orientated micro pores that are needed for lithium-ion battery separator are processed during cold and hot stretching of the non-porous precursor film with different draw ratio under certain temperature in both machine direction (MD) and transverse direction (TD), as seen in Figure 1-7 (d). In comparison, in the wet process, called phase inversion process, PP or PE resin is first mixed with plasticizer or processing oil and then extruded into gel-like film. The film then goes through solvent where the plasticizer is dissolved and the porous film is formed. Usually, slightly stretching in MD and TD of this porous film is helpful to increase the size of the pores. The multilayer of polymeric separator, PP-PE-PP, is usually made through co-extruding of multilayered PP and PE precursor or heat-welding and followed by the same cold and hot stretching mentioned above [46,48]. The trilayer separator has better thermal properties than single layer polymeric separator by combining the properties of low-temperature PE layer shutdown and high temperature integrity of outer PP layers. In recent years, with requirement of the high energy and high power density cell, ceramic-coated polymeric separator was developed to improve the thermal performance of conventional polymeric separator because polymeric layers only will shrink in a large amount when the temperature in the cell raises to a much higher temperature and bring direct contact of cathode and anode and lead to internal shorts thereafter. The coating layer on polymeric films are processed by first applying the slurry that consists of ceramic particles, like aluminum oxide (Al_2O_3), water-insoluble polyvinylidene fluoride (PVDF) and water-soluble binder on the surfaces of polymeric polymer and then drying in the oven [49,50]. Another group of lithium-ion battery separators are nonwoven ones that are usually made of organic and inorganic fibers. The manufacturing process includes paper making, electrospinning process etc. [38–40,51,52]. The nonwoven separator has good thermal stability but poor mechanical properties. Detailed mechanical properties will be seen in Chapter 3. At the time of this thesis, the dry-processed separators with or without ceramic coatings are still the most commonly seen in EV lithium-ion batteries due to its low cost and effectiveness.

Understanding the mechanical properties of battery separators and providing effective material model for industrial practice are the focus of this thesis. By comparing mechanical properties of different types of separators that are commercially available for lithium-ion batteries and by examining the deformation mechanism at micro level, a better understanding of the internal shorts due to mechanical loading yields and will provide useful guidance for EV battery separator selection.

1.3 Thesis outline

The thesis is devoted to a comprehensive test and numerical study of battery cell components related and important for mechanical safety: shell casing and separator. The thesis is decomposed to six chapters with topics of shell casing first and then separator.

After the introduction of lithium-ion battery safety, shell casing and separator, Chapter 2 provides a comprehensive test program on commercially available empty shell casing of 18650 lithium-ion cylindrical cells. Part of the tests was used to determine plasticity and fracture properties from sub-size specimens cut from the lateral part of the cans. The other part served to validate the plasticity and fracture models under various loadings. Strain and displacement were determined by means of the DIC (Digital Image Correlation) method. Detailed finite element (FE) models were constructed for each type of miniature specimens as well as the entire shell casing. Numerical simulations were run for each test to extract information on local stress and strain states. The associated flow rule was used to simulate the plasticity behavior and the Modified Mohr-Coulomb (MMC) fracture model was adopted to predict the crack initiation of shell casing. The results of simulation confirm that the present plasticity and fracture models could predict the global plastic behavior of the cells under different loading conditions and also show that the initiation and propagation of cracks in shell casing were captured correctly. The jellyroll model with volumetric hardening feature was introduced to compare the performance of empty shell casing, bare jellyroll and the complete battery cell. It shows that in many loading situations, for example, three-point bending of the cylindrical cells, the metallic shell casing provides most of the mechanical resistance.

Chapter 3 is on comparison of the mechanical properties, such as strength and failure, of four types of commonly used battery separators and provides a comprehensive test procedure on separator mechanical evaluation. This includes two dry-processed polypropylene (PP) and trilayer separators, a wet-processed ceramic-coated separator, and a nonwoven separator. In detail, uniaxial tensile tests were performed along machine direction (MD), transverse direction (TD) and diagonal direction (DD). Also, through-thickness compression tests and biaxial punch tests were conducted. Comprehensive mechanical tests revealed interesting deformation and failure patterns under extreme mechanical loads. With the discovery of two distinct deformation and failure mechanisms under punch loading, we could explain presumably sporadic displacement to onset of short circuit under local penetration tests (nail or conical punch), where in exactly similar cell and test set-ups one cell goes to thermal runaway while the other shows minimal reactions. Additionally, by investigation of failure modes, we explained the process of formation of local "soft short circuits" in cells with undetectable failure. We proposed a criterion for predicting onset of soft short from experimental data.

Through the practice in Chapter 3, the stress-strain curves from all the tests are more or less enough for numerical simulation purposes. However, detailed information such as the cause of high in-plane anisotropy for dry-processed separators and the deformation mechanism of semi-crystalline structure which gives the insight of onset of short circuit is still not covered. Chapter 4 picks the most common and simple dry-processed single PP separator and provides a detailed characterization and deformation study of fibrils and lamellae through SEM micrograph and X-ray diffraction (XRD) from interrupted tensile test with different strains. From the SEM micrograph of surface and cross section, the micro structure of the separator is revealed and the contribution to highly in-plane anisotropic properties by structural anisotropy and material anisotropy is distinguished from numerical simulations with assumption of isotropic material of micro fibrils and lamellae. The interrupted test and corresponding SEM micrograph as well as wide and small angle XRD shows the deformation sequence of crystalline and amorphous parts, evolution of pores and fragmentation, which brings the understanding of separator failure at micrometer level.

Several characterization technics are also applied to the PP separator. Temperature effect of PP separator was studied with dynamic mechanical analyzer (DMA). Strain rate effect was captured with Instron tensile machine. Chemical bond information was obtained by Fourier transformation infrared spectroscopy (FTIR). The distribution and orientation of crystalline inside PP separator is achieved by wide angle X-ray scattering (WAXS) and small angle X-ray scattering (SAXS).

Chapter 5 discusses the aging/degradation of a dry-processed trilayer separator. The aging of lithium-ion batteries that related to capacity loss, such as fading of electrodes and loss of electrolytes, have been intensively studied. The widely used polymeric separators sandwiched between cathode and anode, which do not directly contribute to electrochemical properties of the cell, are usually considered as chemically, thermally and structurally stable materials. In this chapter, the degradation of a dry-processed trilayer separator due to charge-discharge cycles is investigated. By comparing the properties of the separators from disassembled cells after different numbers of charge-discharge cycles, it is found that the separators underwent higher cycles failed with much lower punch force and smaller displacement. Cell level tests also indicate that the displacement and force to short circuit under lateral indentation for an elliptic cell after 1200 cycles are smaller than those of a 0 cycle cell. Although, the SEM images of cross section of separators show no significant pore size and pattern change after 1200 cycles, the reduction of strength level could be potentially caused by chain split and physical related aging.

Chapter 2

Test and Modeling of 18650 Shell Casing

2.1 Introduction

Shell casing of lithium-ion batteries must perform under multiple tasks. It provides the first level of thermal and mechanical protection to the jelly roll, they must perform well under verity of abuse loading, and it must be light and easy to manufacture. The cell can be made from extruded aluminum tubes with laser welded endcap. More commonly, a multi-stage deep drawing technology is used for both steel and aluminum thin sheets. The supplier of shell casing provided minimum or no information on the mechanical properties of raw material used or the final product. Such information is critical to assess performance limit of cells in terms of resistance to mechanical loading and fracture during accidental load and/or compliance with safety standards such as SAE J2464 [53].

While no details on shell casing fracture emerged from reports on full scale crash accidents, the laboratory test provided sufficient evidence that this is a valid and serious failure mode. Sahraei and Hill [54] performed tests on axially compressed cylindrical cells during which a longitudinal crack was developed from a local bulge. Fracture on the tensile side of shell casing was observed in three-point bending test [9,55]. Sahraei et al. [56] described a compression tests on large format cylindrical cell. The cell exploded, tearing the shell casing into small pieces. Finally, Xia et al. [57] performed numerical simulation of the 18650 cell under symmetric and eccentric load by a sharp punch. The symmetrically loaded cell casing ruptured under 6 mm indentation depth. Fracture of eccentrically loaded cell occurred much earlier, when the punch travelled only 1.6 mm. Considering the existing evidence and potential hazard associated with spreading gases, spill of the electrolyte and possible fire from the bursting cell to the neighboring ones, a proper attention should be given to this problem by the battery safety community.

The objective of the present chapter is to determine plastic and fracture properties of the shell casing material using the most modern technology developed in the Impact and Crashworthiness Lab of MIT [25,27,29,36,58,59]. This effort consisted of an extensive experimental program, model calibration and component validation. Almost 100 empty shell casings were tested to complete the stated task. For that purpose, a procedure developed over the past seven years by the investigating team has been substantially modified. First, the virgin steel sheet, from which the casings were made was not available. Specimens had to be cut from the actual shell casing, which restricted its size and shape to a certain degree. Secondly, the shell casing material has undergone relatively large strain during the deep drawing process. These strains are distributed non-uniformly along the length of the cell. The anisotropic properties arising first from the rolling process of the sheets and then deep drawing process are substantial and were taken in to account. Finally, there is a considerable variation in thickness of the can form 0.253 mm to 0.29 mm at the ends. The endcap on the other hand was not subjected to any strain histories and represents the virgin material. The size of the endcap is too small to cut any specimens. All the above features made the testing and calibration procedure much more difficult as compared to previous work in the lab on thin automotive sheets. From this point of view, the present chapter is indeed innovative in terms of both test procedures and numerical simulations.

2.2 Plasticity modeling for the battery shell casing

The commercially available shell casing of the 18650 cells is approximately 18 mm in diameter and 65 mm in length and made from low carbon steel. The cylindrical cells are widely used as batteries for laptop and portable power. Such cells are also powering the Tesla Model S. The shell casing is made by deep drawing, which can reduce the cost compared with the extruding one with welded endcap.

2.2.1 Material

A typical deep drawing process consisting of several steps from a flat circular sheet to the final shape is shown in Figure 2-1. The deep drawing process results in considerable accumulated plastic strain, leading to the deformation induced anisotropic of the sheet that can be determined experimentally. Therefore, due to the anisotropic properties of the virgin rolled sheet and deformation induced anisotropy, the thickness of the shell casing varies along both axial direction and hoop direction of the casing, as shown in Figure 2-2. The area with maximum thickness is around the open end of the can and minimum thickness is approximately in the middle. Such a distribution of thickness was also reported in the literature for deep drawn shell casing [60]. The average wall thickness is 0.26 mm. The chemical composition, determined by Pierre-Olivier Santacreu of Aperam is summarized in Table 2-1.

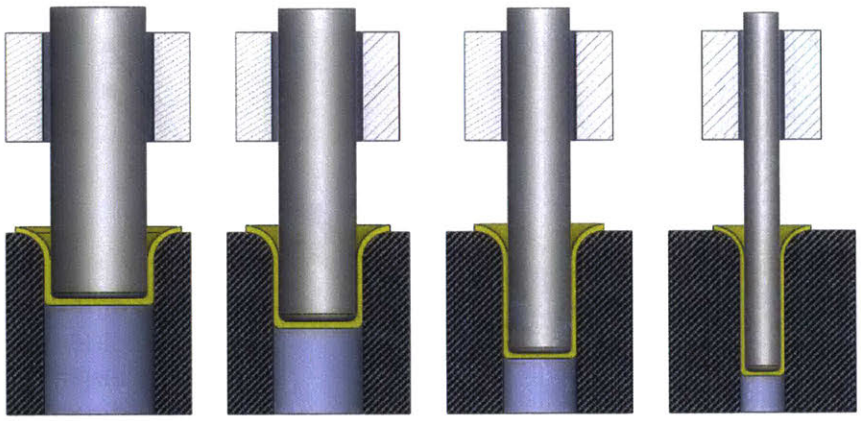
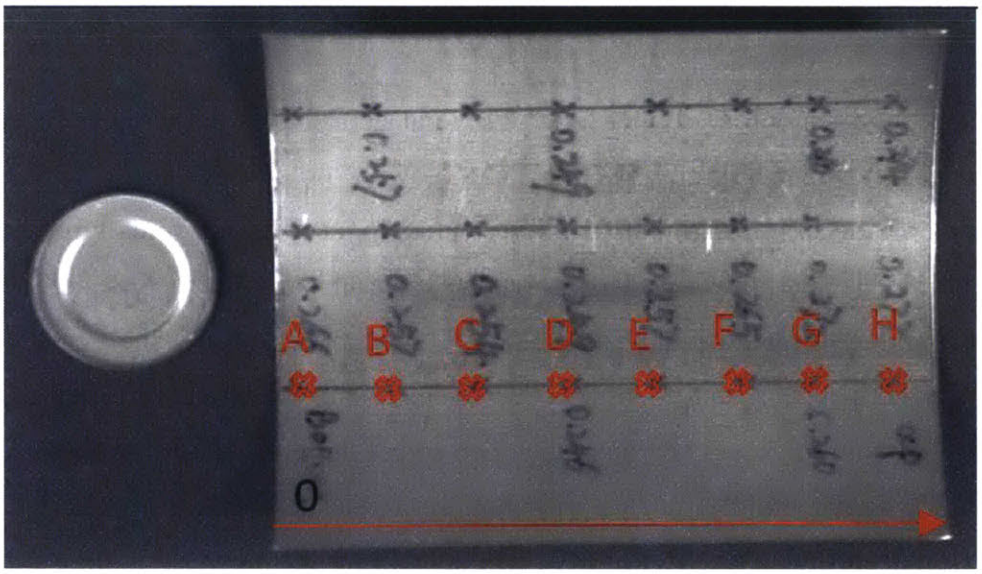
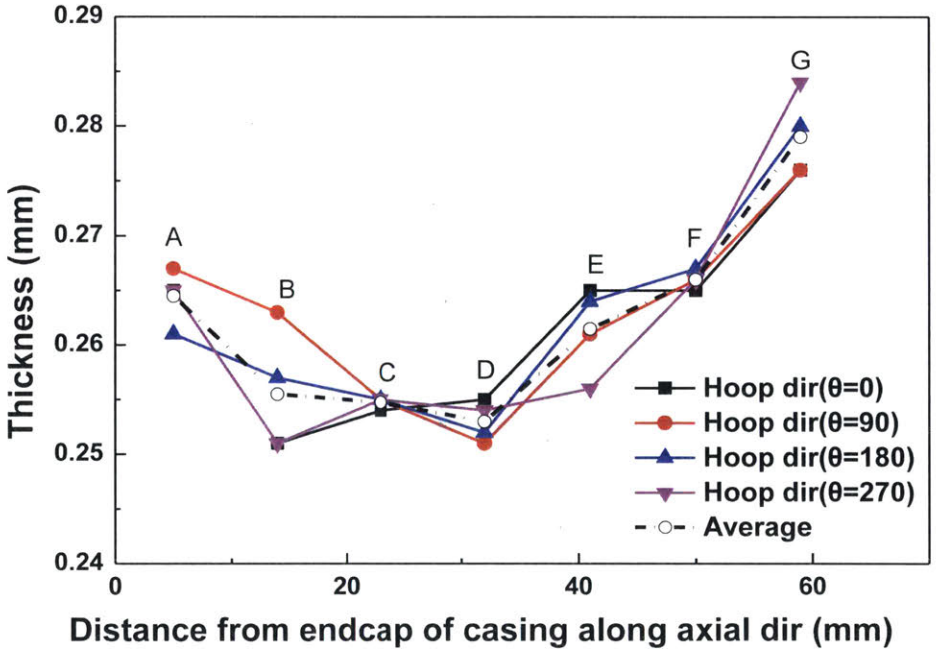


Figure 2-1 Illustration of a typical deep drawing process



(a)



(b)

Figure 2-2 Non-uniform thickness distribution of the shell casing. (a) position in casing; (b) thickness distribution chart

Table 2-1 Chemical composition of the shell casing

Element	Mn	P	Ni	Cr	Cu	Mo	V	Ti	Co
Percentage	0.16	0.008	1.36	0.056	0.012	0.002	0.003	0.003	0.006

The shell casing, received from supplier has a very thin layer of coating on the outer surface. The inner surface is uncoated and thus is susceptible to corrosion. The corrosion test was performed by removing a small area of local coating and emerging the specimen for three months in drinking water. The resulting massive corrosion is shown in Figure 2-3. All specimens were extracted from the same package of the battery cell (100 pieces) and can be assumed to have the same mechanical properties.



Figure 2-3 Corroded shell casing after 3 months exposure to water

2.2.2 Description of the test method and preparation of the specimens

To study the plastic behavior of the shell casing, the endcap was removed first and then cut lengthwise and flattened, as shown in Figure 2-4. Dogbone-shaped specimens were cut from three different orientations on flattened sheet (axial or deep drawing direction, hoop direction and diagonal direction) using a milling machine. The specimen geometry (Figure 2-5a) is different from that in ASTM-E8M standard (sheet type), due to the limited length and diameter of the shell casing. Since the dimension of the flattened sheet of the shell casing is 65 mm in length and 56 mm in width (hoop direction), the geometry of dogbone along hoop direction is 10 mm shorter than in axial and diagonal direction. Figure 2-5b shows the specimens after cutting and relatively large spring back was observed for specimens along diagonal and hoop direction. Digital Image Correlation (DIC) was used

to measure the local strain, displacement and Lankford ratio (Vic 2D, version 2009). The specimens were tested on a table-top uniaxial loading machine (Instron Model 5940 with load capability 2 kN).

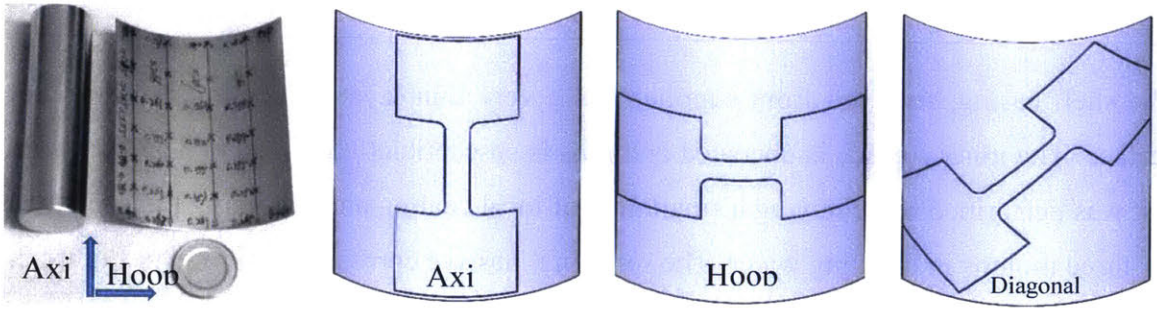
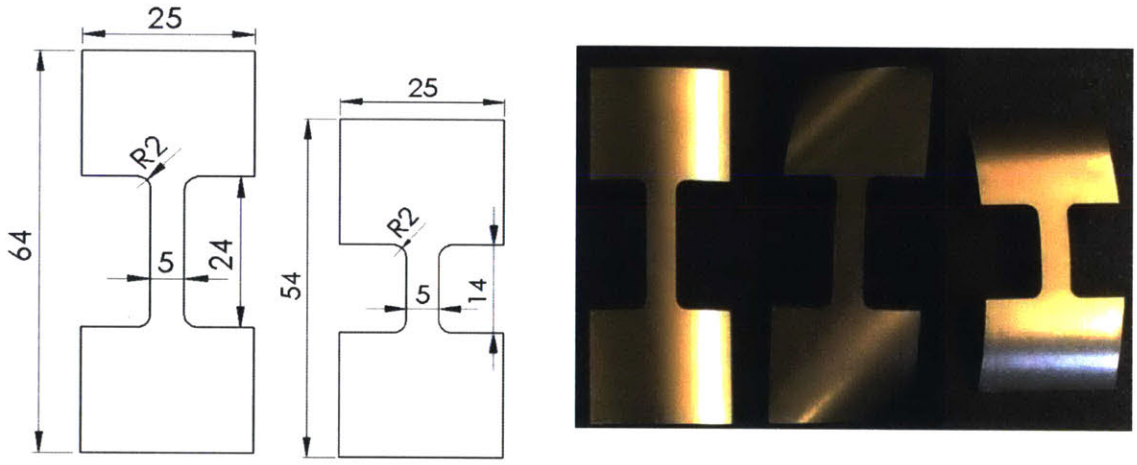


Figure 2-4 Specimen preparation from the flatted shell casing in different material orientations (0°, 45° and 90° to the deep drawing direction)



(a) (b)

Figure 2-5 Geometry of the dogbone specimen (dimension in mm) and specimens before test. (a) along axial, diagonal direction (left) and hoop direction (right); (b) specimens along axial (left), diagonal (middle) and hoop direction (right)

Figure 2-6 shows the engineering stress-strain curves in three directions from 6 tests (2 in each direction). The displacement for calculating engineering strain was measured from positions closed to the end of the gauge section (gauge length is 8 mm for specimens along hoop direction and 18 mm for the other two). The cross section was assumed as 0.26 mm when calculating the engineering stress. The repeatability of the test is relatively good,

even though the thickness of the flattened sheet varies from specimen to specimen and varies from region to region within specimen. The nominal Young's modulus is 160 GPa (due to non-uniform thickness) and the average flow stress is 500 MPa.

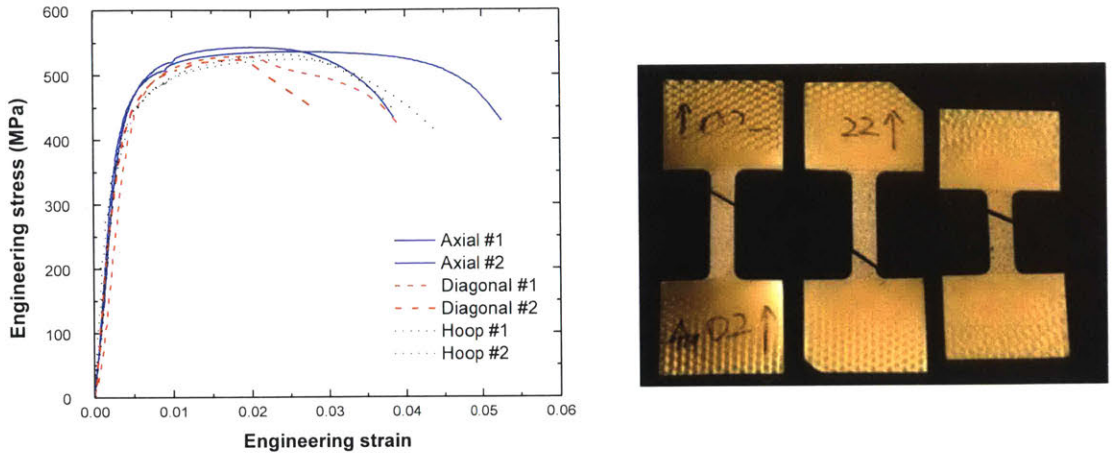


Figure 2-6 Engineering stress versus strain curve (left) and fractured dogbone specimens (right)

The flattening process may bring a certain amount of pre-damage to the final specimen. To study the flattening effect, alternative uniaxial tensile tests were conducted. Window-shaped specimens were cut directly from the shell casing without flattening, as shown in Figure 2-7 (left). The geometry of the gauge section of the specimen is approximately the same as the above dogbone specimen. Figure 2-7 (right) shows the setup of the uniaxial tension test of the window-shaped specimen. To calculate the engineering stress-strain curve of the specimen, exact area of the initial gauge section was obtained from geometric model and the DIC method was used to get the local strain. The comparison of window-shaped specimen and dogbone specimen is shown in Figure 2-8. The result shows that there is only a slight hardening effect due to the flattening process.

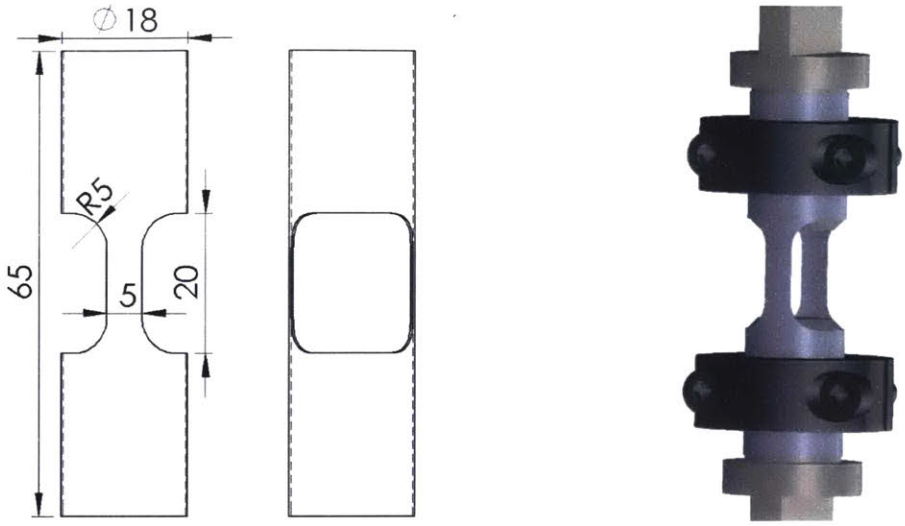


Figure 2-7 Geometry of the window-shaped specimen (left) and uniaxial tension test setup (right)

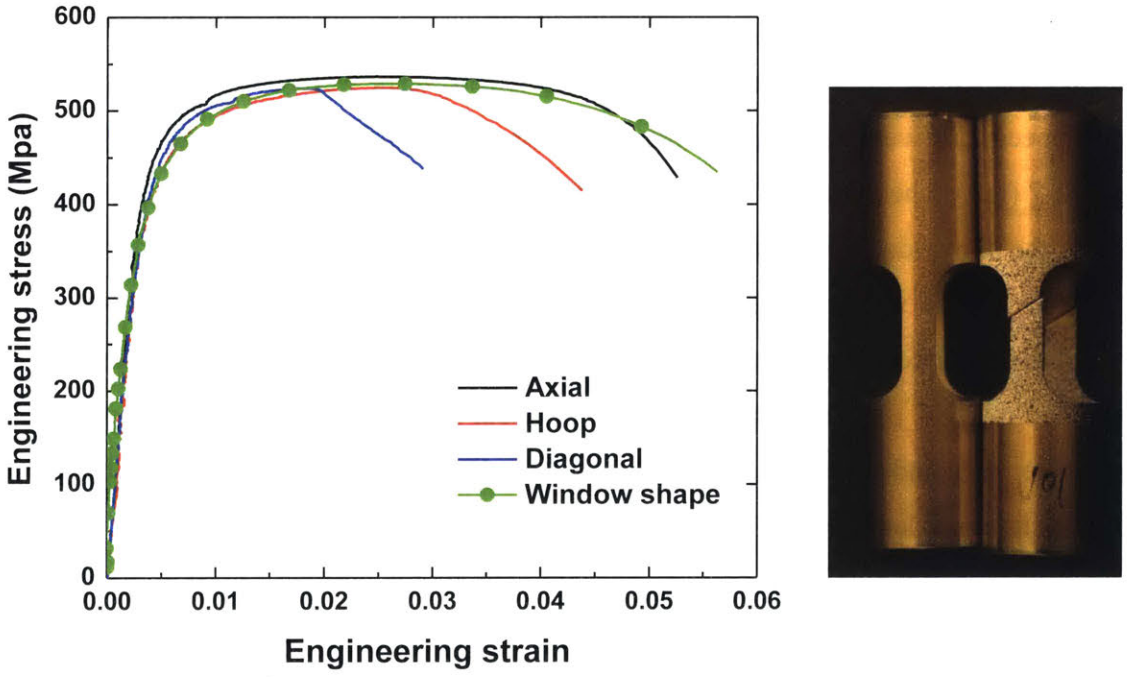


Figure 2-8 Comparison of stress-strain curves of uniaxial tension (left) and fractured window-shape specimen (right)

2.2.3 Calibration of Hill's 48 anisotropic plasticity model

Hill'48 anisotropic yield surface with associated flow rule and isotropic hardening law was used to model the shell casing material.

$$f(\boldsymbol{\sigma}, \bar{\varepsilon}_p) = \bar{\sigma}_{hill}(\boldsymbol{\sigma}) - k(\bar{\varepsilon}_p) = 0 \tag{2-1}$$

$$\bar{\sigma}_{hill} = \sqrt{F(\sigma_y - \sigma_z)^2 + G(\sigma_z - \sigma_x)^2 + H(\sigma_x - \sigma_y)^2 + 2L\tau_{yz}^2 + 2M\tau_{zx}^2 + 2N\tau_{xy}^2} \tag{2-2}$$

$\bar{\sigma}_{hill}$ denotes the Hill'48 equivalent stress, $\bar{\varepsilon}_p$ is the corresponding work-conjugate equivalent plastic strain, $\boldsymbol{\sigma}$ is Cauchy stress tensor, and k is deformation resistance, which is a function of $\bar{\varepsilon}_p$. x, y and z is the direction along axial, transverse and thickness direction of the flattened sheet. The Hill'48 parameters, $F \sim H$, were calculated from Lankford ratio by assuming the associated flow rule and planar anisotropy, as shown in Table 2-2. The normality condition for Hill'48 is written as

$$d\boldsymbol{\varepsilon}_p = d\bar{\varepsilon}_p \frac{\partial f}{\partial \boldsymbol{\sigma}} \tag{2-3}$$

Lankford ratio is defined by $r = d\varepsilon^p_{width}/d\varepsilon^p_{thickness}$. The logarithmic plastic strain along tension and transverse direction can be determined using DIC, Poisson's ratio and Young's modulus. By assuming the plastic incompressibility, the plastic strain along thickness was then obtained. The summary of the Lankford ratio is in Table 2-3.

Table 2-2 Hill'48 coefficients determined from Lankford coefficient

F	G	H	L	M	N
0.65	0.56	0.43	1.5	1.5	1.37

Table 2-3 Lankford coefficients determined from uniaxial tensile test

	α=0°	α=45°	α=90°	r_{avg}
r	0.77	0.62	0.66	0.683

2.2.4 Determination of hardening curve before and after necking

The two most commonly used fit of the hardening curve are the Swift power hardening law,

$$K_s = A(\varepsilon_p + \varepsilon_0)^n \tag{2-4}$$

and the Voce law

$$K_v = B - C * exp(-D * \varepsilon_p) \tag{2-5}$$

In the pre-necking, uniform deformation stage, both Swift and Voce laws can provide a reasonably good fit of the test data (Figure 2-9). The corresponding Swift and Voce law parameters, determined by the minimizing mean square difference between test and Eq. (2-4) and (2-5) are given in Table 2-4. As an input file in numerical simulation, the actual test data was used in the range up to necking ($\varepsilon_p < 0.02$). Once necking occurs, the extrapolated stress-strain curve cannot be used anymore due to three dimensional state of stress in the necked region. To determine the post-necking stress-strain efficiently, a one-parameter linear-combination of Swift-Voce law fitting function was used

$$K_{opt} = \alpha K_s + (1 - \alpha)K_v \tag{2-6}$$

where α is the linear weighting function. In order to determine the parameter α, an inverse method was utilized by best fitting the force-displacement curves from simulation and corresponding test [31,32,36,59,61]. Dunand [59] recommended to use notched specimen to obtain α instead of dogbone specimen for the necking since fracture region of a notched specimen

was identical compared with that of a dogbone specimen. The geometry of the notched is shown in Figure 2-12a, which is cut along axial direction of the shell casing using milling machine. A detailed FE model (half model with fine solid mesh of 0.033 mm×0.08 mm×0.02 mm in the gauge section, 6 elements through thickness and with element type of C3D8R), exploiting the symmetry of the geometry specimen, was built for notched tensile test in Abaqus/Explicit (Figure 2-10). The Hill'48 plasticity and associated flow rule were implemented through a user subroutine with disabled fracture option. Both the Swift law and Voce law parameters as well as the optimized α are given in Table 2-4. Figure 2-11 shows the comparison between simulation and test. The Swift law fit over-predicts the stain hardening and the Voce law fit under-predicts the strain hardening. The optimized hardening curve, was manually optimized giving $\alpha = 0.5$. Swift law was then adapted to refit the optimized hardening curve to obtain a new pair of A = 680 MPa and n = 0.047 for calibration of MMC fracture model in Section 2.3.

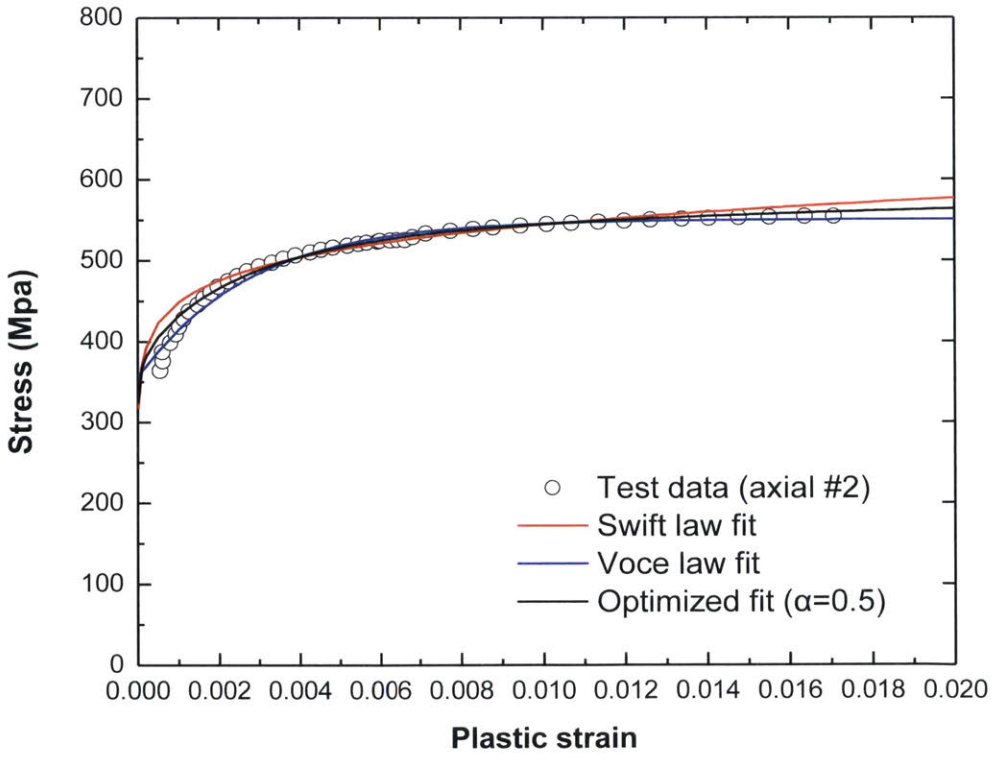


Figure 2-9 Swift law and Voce law fitting of hardening curve

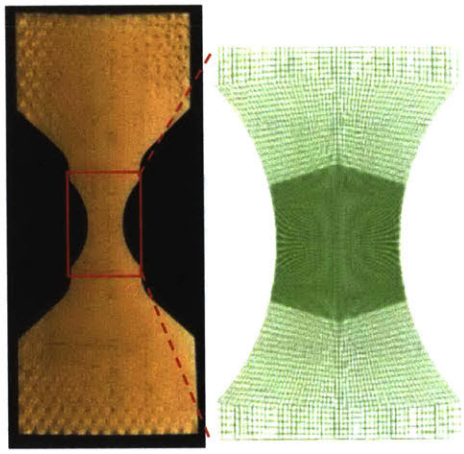


Figure 2-10 FE model of notched specimen

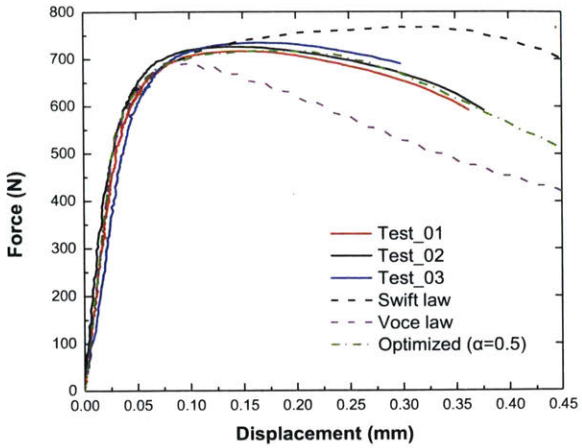


Figure 2-11 Prediction of force-displacement with Swift law, Voce law and optimized hardening curve for notched specimen

Table 2-4 Combined Swift and Voce hardening law parameters

A	ε_0	n	B	C	D	α
800	0	0.084	356	194.5	360	0.5

2.3 Fracture modeling for the battery shell casing

2.3.1 Introduction of Modified Mohr-Coulomb fracture model

Previous work of the investigating team illustrates that Modified Mohr-Coulomb (MMC) fracture model with stress triaxiality and Lode angle dependence, proposed by Bai and Wierzbicki [27] can provide successful prediction of fracture under complicated loading condition [29,31,32,36,62]. For the benefit of the battery modeling community, it will be helpful to recall the definition of stress triaxiality and Lode angle.

The stress state in a material element is fully described by three principal stresses or three invariants of the stress tensor, the first invariant of stress tensor (I_1) and the second and third invariants of the stress deviator (J_2, J_3)

$$\mathrm{I}_1 = \mathrm{tr}(\boldsymbol{\sigma}), \qquad \mathrm{J}_2 = \frac{1}{2}\boldsymbol{\sigma}' : \boldsymbol{\sigma}', \qquad \mathrm{J}_3 = \det(\boldsymbol{\sigma}') \tag{2-7}$$

where $\boldsymbol{\sigma}'$ donates the deviator of Cauchy stress tensor. For fracture description, it is convenient to work with dimensionless parameters, the stress triaxiality η and the Lode angle θ. The stress triaxiality is defined as mean stress σ_m over von Mises equivalent stress $\bar{\sigma}_{Mises}$,

$$\eta = \frac{\sigma_m}{\bar{\sigma}_{Mises}} \tag{2-8}$$

The Lode angle parameter θ is a function of the second and third stress invariants,

$$\theta = \frac{1}{3}\cos^{-1}\left(\frac{3\sqrt{3}}{2}\frac{\mathrm{J}_2}{\mathrm{J}_2^{3/2}}\right) \quad (0 \le \theta \le \frac{\pi}{3}) \tag{2-9}$$

In the MMC fracture model, a modified definition of the Lode angle is used,

$$\bar{\theta} = 1 - \frac{6\theta}{\pi} \quad (-1 \le \bar{\theta} \le 1) \tag{2-10}$$

so that the range of $\bar{\theta}$ is from -1 to 1.

The damage accumulation rule for MMC model is captured by defining the damage indicator function $D(\bar{\varepsilon}_f)$, where each increment of the equivalent plastic strain ε_f is normalized with the respect of the current value of fracture locus,

$$D(\bar{\varepsilon}_f) = \int_0^{\bar{\varepsilon}_f} \frac{d\bar{\varepsilon}_f}{\hat{\varepsilon}_f(\eta,\bar{\theta})} \tag{2-11}$$

Crack is assumed to initiate when D reaches unity. For proportional loading, where both η and$\bar{\theta}$ are constant, Eq. (2-11) yields

$$\bar{\varepsilon}_f = \hat{\varepsilon}_f(\eta, \bar{\theta}) \tag{2-12}$$

where $\hat{\varepsilon}_f(\eta, \bar{\theta})$ is so called fracture locus for proportional loading. A specific form of the fracture locus follows from the classical Mohr-Coulomb fracture model. Transforming the local fracture criterion on the fracture plane into the space of $(\eta, \bar{\theta}, \bar{\varepsilon}_f)$, the following fracture criteria is obtained

$$\hat{\varepsilon}_f(\eta, \bar{\theta}) = \left\{ \frac{A}{c_2} \left[c_3 + \frac{\sqrt{3}}{2-\sqrt{3}} (1 - c_3) \left(\sec\left(\frac{\bar{\theta}\pi}{6}\right) - 1 \right) \right] \times \left[\sqrt{\frac{1+c_1^2}{3}} \cos\left(\frac{\bar{\theta}\pi}{6}\right) + c_1 \left(\eta + \frac{1}{3} \sin\left(\frac{\bar{\theta}\pi}{6}\right) \right) \right] \right\}^{-\frac{1}{n}} \tag{2-13}$$

where A = 680 MPa and n = 0.047 are the parameters from refitted optimized hardening curve, and c_1, c_2, c_3 are three parameters of MMC model needed to be calibrated from fracture tests with different combination of stress triaxiality η and normalized Lode angle $\bar{\theta}$.

2.3.2 Calibration of the MMC fracture model

The MMC fracture model involves three parameters, so at least 3 types of tests are needed to fully calibrate the MMC model. A hybrid experiment-numerical method was developed by Dunand et al. [59], which reconstructed the test in finite element environment by fitting the force-displacement curve and extracting the history of $\eta(t)$, $\bar{\theta}(t)$ and $\bar{\varepsilon}_f(t)$ from the critical element (usually with maximum equivalent plastic strain) up to the measured displacement to fracture in test. The damage indicator was calculated according to Equation (2-11) and a set of (c_1, c_2, c_3) was optimized following this algorithm,

$$[c_1, c_2, c_3\,] = \arg\min_{c_1,c_2,c_3} \sum_{i=1}^{N} \left(1 - D_i^f(\eta(t), \bar{\theta}(t), \bar{\varepsilon}_f(t), c_1, c_2, c_3)\right)^2 \tag{2-14}$$

Considering the limitation of the flattened shell casing (length 65 mm, width 54 mm and extremely thin shell thickness 0.26 mm), it is not possible to fabricate any grooved specimens or specimens with reduced thickness in gauge section. Five types of uniform

thickness specimens were chosen, shown in Figure 2-12. The specimens with central hole, notched specimens and butterfly tensile specimens were cut along axial direction. The rectangular sheet (Figure 2-12d) was clamped on a circular die with inner diameter of 29.9 mm and loaded by a hemispherical punch head with diameter of 25.4 mm. To limit the friction, five oil-lubricated 90 μm thick Teflon layers were put between punch head and specimen during each test. A simple shear specimen, shown in Figure 2-12e, was cut directly from shell casing without flattening procedure with geometry scaled from Reyes et al. [63]. The grips for shear test are the same as those in Figure 2-7. The stress triaxiality of these tests range approximately from 0.15 to 0.66. All the tests were performed using the 2-kN Instron Model 5940 except the butterfly tensile specimens, which were conducted using a custom-made dual actuator loading frame. Each type of test was repeated three times.

The test results from the five types of tests are shown in Figure 2-13 by solid lines. Because the thickness is not uniformly distributed, several test data are plotted to illustrate the repeatability. Using the hybrid method stated above, corresponding FE model of each type of test was built in Abaqus/explicit. Matlab code was used to solve the Eq. (2-14). The parameters of MMC model were then obtained ($c_1 = 0.20, c_2 = 425\ MPa, c_3 = 0.90$) and used as input parameters in subsequent numerical validation. The 3D fracture locus defined by the Eq. (2-13) is plotted in Figure 2-14. A user subroutine (VUMAT) with Hill'48 yield function and associated flow rule and MMC fracture model was implemented in Abaqus/Explicit [64]. A comparison of measured and calculated force-displacement curves demonstrate the good agreement of experiments and FE model with Hill'48 yield function and associated flow rule and calibrated MMC parameters, see Figure 2-13. It is worth mentioning that for simulating the simple shear specimen, the hardening curve from the flattening material was used by exploiting the results from Section 2.2. Usually, to illustrate the accuracy of the plasticity model, local logarithmic strains from test and simulation were also compared [32,59]. Only the evolution of local strain from notched specimen was compared in this study and the solid lines in Figure 2-13(a) indicates the mismatch due to the non-uniform thickness while the local logarithmic strain was determined from two points in the center of notched specimen with initial distance of 2 mm using DIC method.

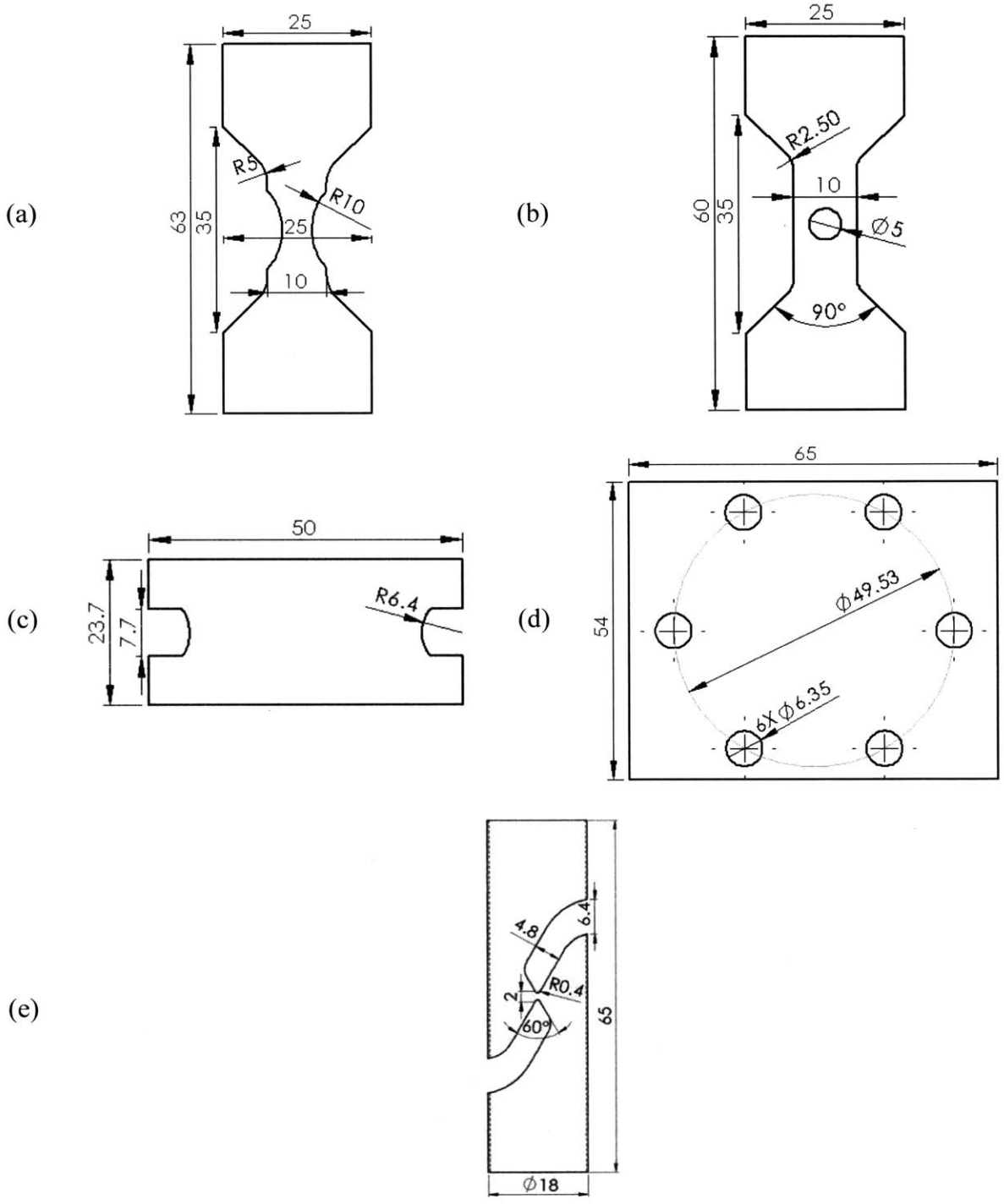
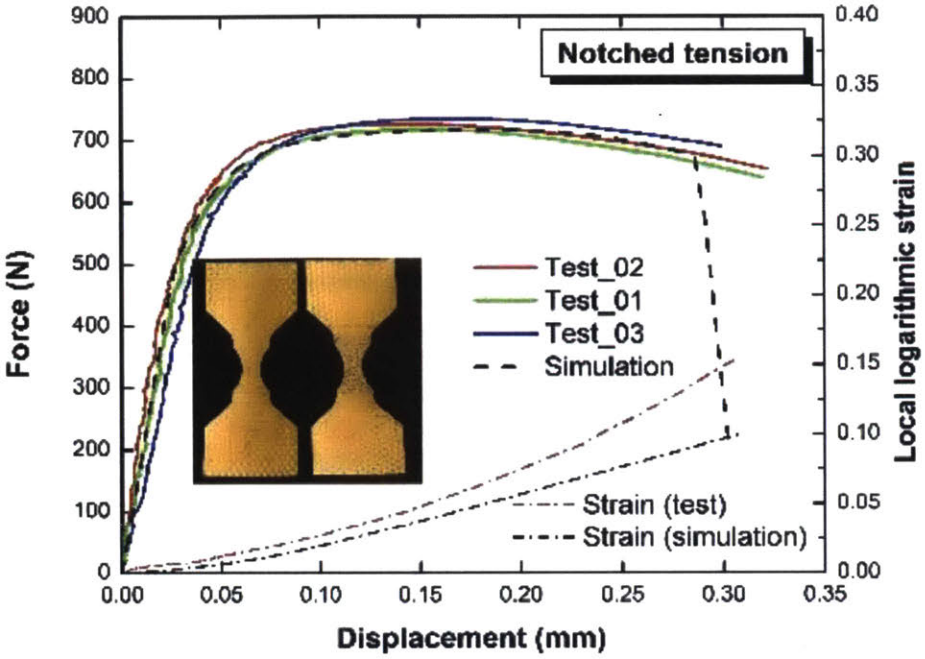
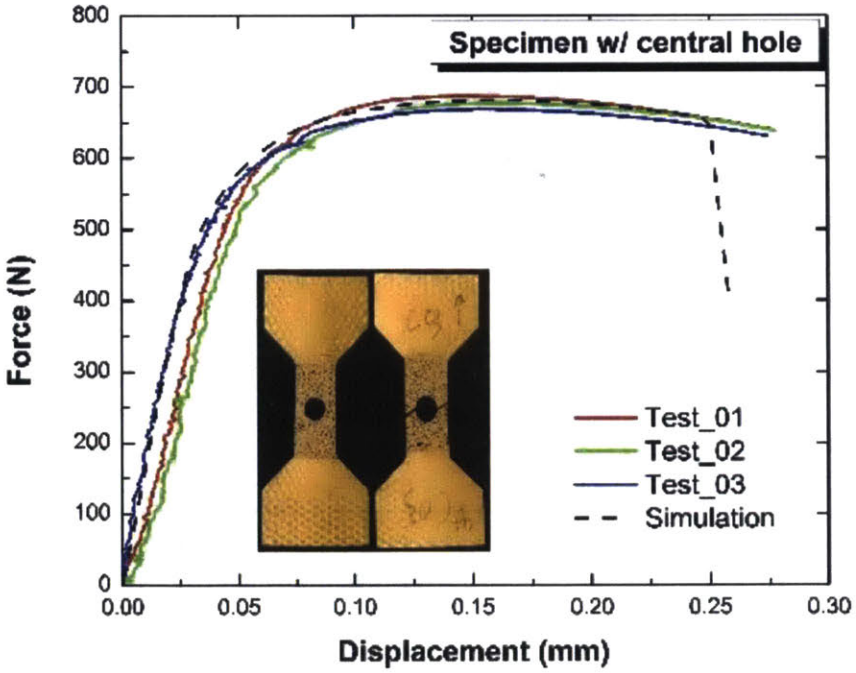


Figure 2-12 Specimens designed for MMC model calibration: (a) notched specimen; (b) specimen with central hole; (c) butterfly tensile specimen; (d) punched specimen; (e) simple shear specimen

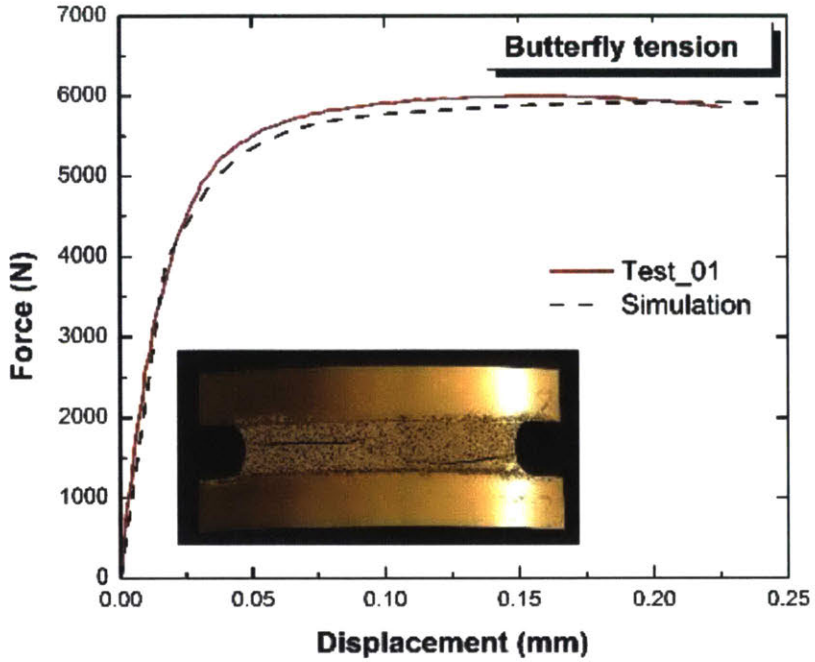
(a)


Notched tension
Force (N)
Local logarithmic strain
Displacement (mm)
Test_02
Test_01
Test_03
Simulation
Strain (test)
Strain (simulation)

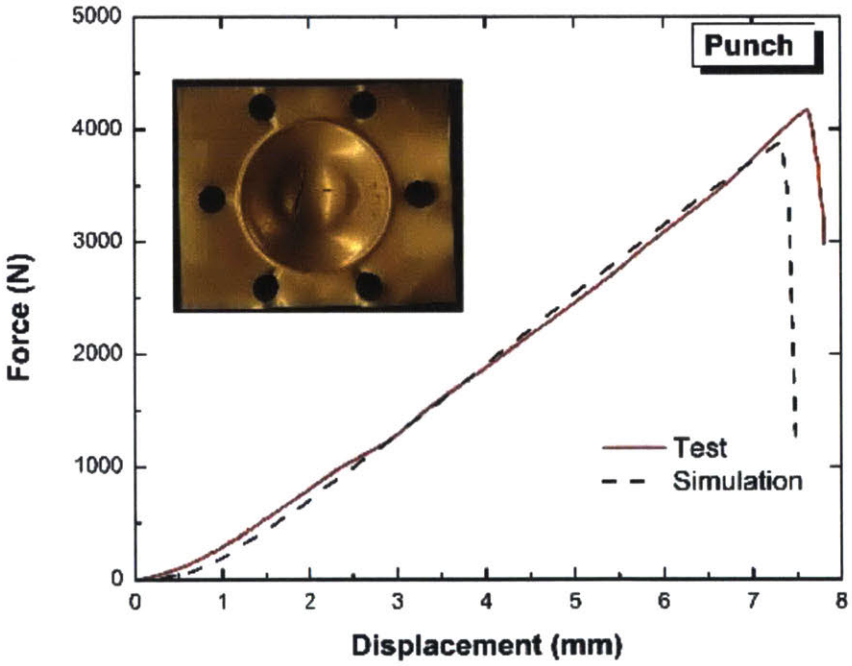
(b)


Specimen w/ central hole
Force (N)
Displacement (mm)
Test_01
Test_02
Test_03
Simulation

(c)


Butterfly tension
Test_01
Simulation
Force (N)
Displacement (mm)
0
1000
2000
3000
4000
5000
6000
7000
0.00
0.05
0.10
0.15
0.20
0.25

(d)


Punch
Test
Simulation
Force (N)
Displacement (mm)
0
1000
2000
3000
4000
5000
0
1
2
3
4
5
6
7
8

(e)

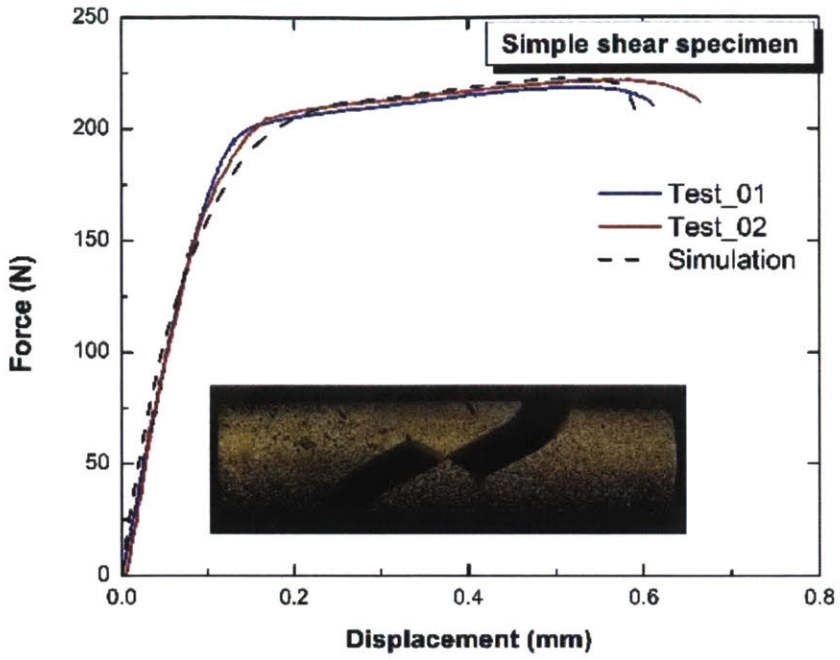


Figure 2-13 Comparison of force-displacement curves between test and simulation: (a) notched specimen; (b) specimen with central hole; (c) butterfly tension specimen; (d) punch specimen; (e) simple shear specimen

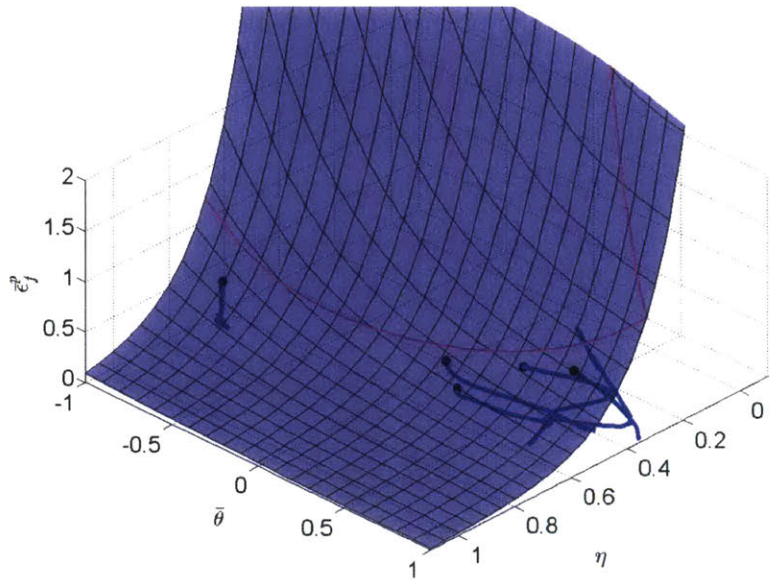


Figure 2-14 The MMC fracture envelopes for battery shell casing

2.4 Validation of the plasticity and fracture model at the "structural" level

To validate the plasticity and fracture model built in Section 2.3, four types of experiments on empty shell casing were performed. All of these types of tests are common loading cases of mechanical abuse of battery cells. The endcap in all tests were not removed.

2.4.1 Axial compression test

Several tests on axial compression of the can were performed. Measured load-displacement response was seen in Figure 2-15. During the test, no fracture was observed. Therefore, only the plasticity model can be validated at this stage. A relatively accurate FE model of the shell casing including endcap was built with thickness varied only along axial direction according to the geometry measured in Figure 2-2. The geometry of endcap, which is not flat (Figure 2-2), was carefully measured. In the FE model, the body of the shell casing was taken as anisotropic along axial and hoop direction, while the endcap was assumed be to isotropic. Two models were constructed, one with shell element (element type: S4R and mesh size 0.2 mm×0.2 mm) and the other with solid element (element type: C3D8R and mesh size: 0.2 mm×0.2 mm×0.032 mm). Figure 2-15 shows the comparison of the experiment and FE simulation. The numerical simulation predicts higher peak force, which is normal for a mathematically perfect axisymmetric model. For the second and third peak, both the shell element and solid element model agree with experiment well.

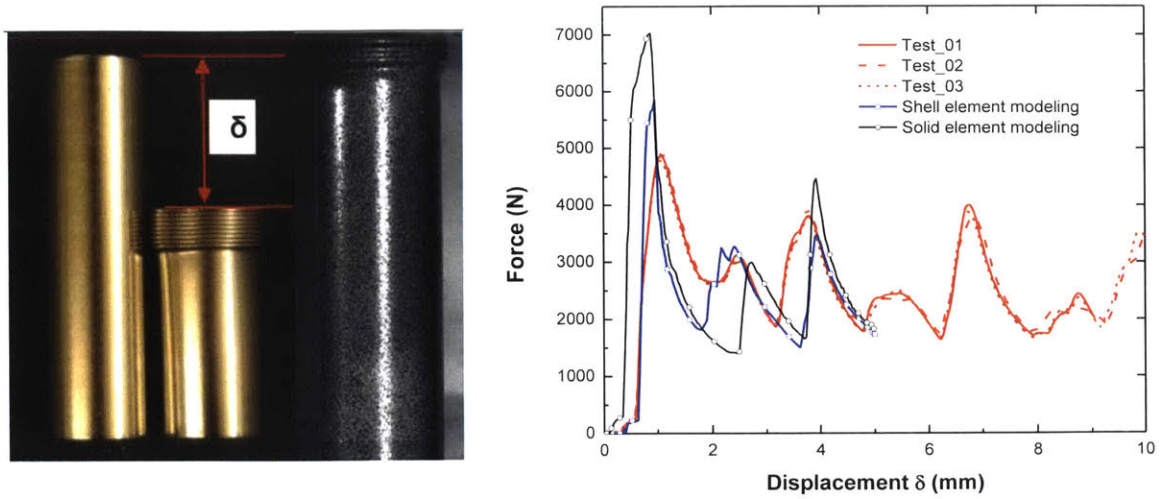


Figure 2-15 Concertina folding of shell casing (left) and force-displacement curve of axial compression of shell casing (right)

2.4.2 Lateral compression test

The shell casing was also subjected to lateral compression between two flat plates. The force-displacement curve is plotted in Figure 2-16. No fracture was observed. The previous FE model with shell element (element type: S4R) was used to simulate the compression process. The main contribution for the displacement mismatch in Figure 2-16 is due to the modelling of the endcap, which has complicated geometry. Two additional simulations were run by using the same model but one with endcap being removed (Model A) and the other with endcap only (Model B) as shown in Figure 2-17. The model B that with endcap only was cut from the position of 6 mm from the edge of endcap rather than the edge with the purposes of defining the boundary condition conveniently. From Figure 2-16, the force level of the shell casing with endcap removed is greatly reduced, and the endcap play a major role in resisting the lateral compression of shell casing. Figure 2-18 shows two special compression instances with each frame corresponding to a marked number in Figure 2-16.

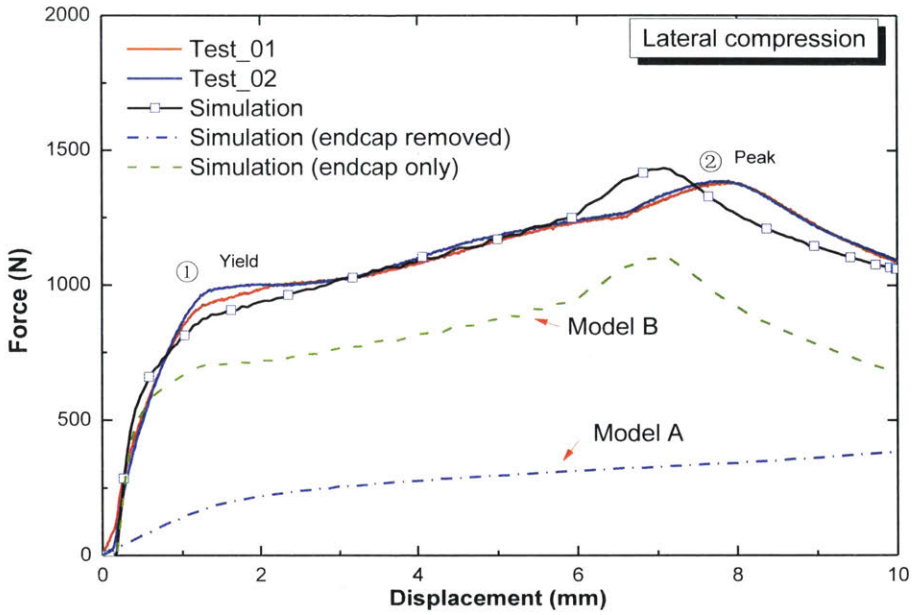


Figure 2-16 Force-displacement of lateral compression of shell casing



Figure 2-17 Models with or without endcap

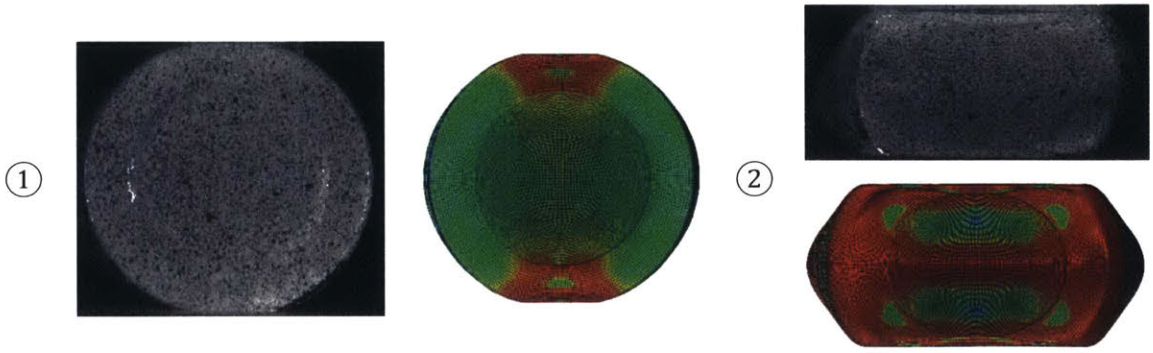


Figure 2-18 Sequence of lateral compression (contour: Mises stress)

2.4.3 Three-point bending test

Three-point bending test is also a typical loading case for battery cell [9,55]. The test setup is shown in Figure 2-19 (left), where the radius of the cylindrical indenter is 10 mm, and the radii of supporting cylinders are 24 mm. The distance between the two supporting cylinders is 58 mm. No fracture was observed even when the displacement of indenter reached 20 mm, 2 mm larger than the diameter of the casing. The model with shell element in Section 2.4.1 was used to simulation the test. The fiction coefficient was set to 0.2. The comparison of force-displacement of test and simulation is shown is Figure 2-19 (right). This also validated the plasticity model of shell casing. Since the endcap of shell casing was not removed in the test, the deformation of both ends was not symmetric in Figure 2-20.

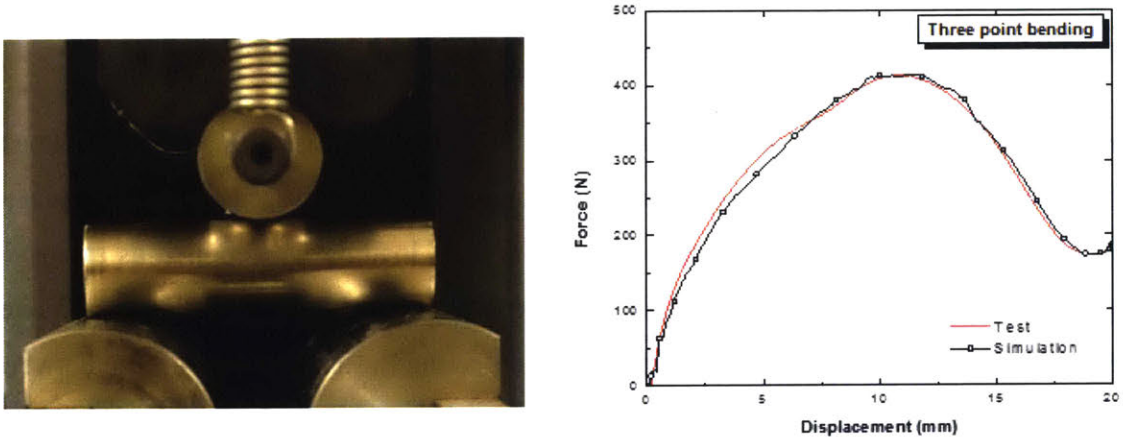


Figure 2-19 Test setup of three-point bending test and force-displacement curve

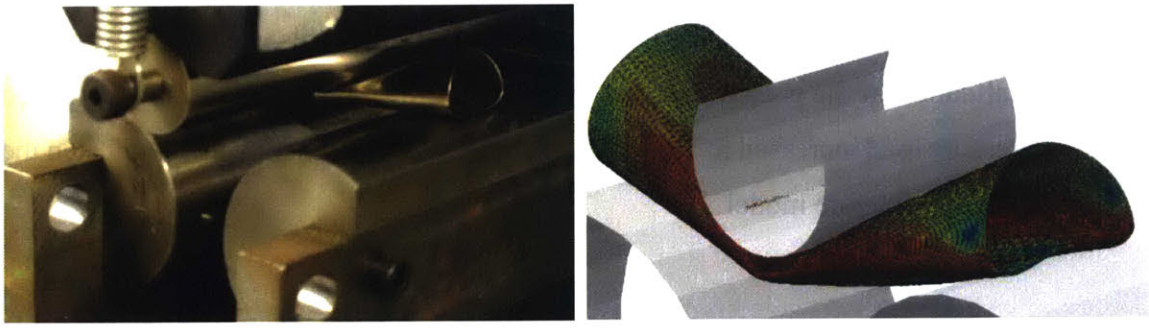


Figure 2-20 Deformation of open end of the shell casing (contour: Mises stress)

2.4.4 Internal pressure test

A hydraulic bulge test using water was introduced, and the setup is shown in Figure 2-21. The shell casing was filled with so called de-aired water, which is commonly used in rock and soil tests and is assumed to be incompressible. A piston with a steel seal plug to release the spare water was assembled in the open end. The piston is designed to have water outlet in the center and two notches to install O-ring to prevent leakage during the test, as shown in Figure 2-22. The piston sits on a flat plate and the side with endcap was subjected to compression by another flat plate. The O-ring was designed to prevent water from leaking out during the test. The clearance between the edges of shell casing and piston prevents support from piston. The experimental force-displacement curve is shown in Figure 2-23, where the displacement was measured from the endcap during the test. The test was performed up to the point of bursting fracture.

To simulation this test, a fine FE model of the shell casing with varied thickness distribution along axial direction (Figure 2-2 average curve) was used and the calibrated MMC fracture model was implemented. In the model, loading was applied as an inside pressure as shown in Figure 2-24, which was calculated from the force in Figure 2-23 over the area of the piston (diameter: 17.45 mm) by neglecting the small friction force between O-ring and shell casing. From the simulation, it is observed that slant fracture occurred when the pressure reached maximum value from test, see Figure 2-25. It is worth noting that this kind fracture can seldom happen in practice because battery cell has cap valve to release internal pressure (typically less than 3 MPa). However, this type of test provides important validation of the present fracture model. That fracture of shell casing happened when the pressure load increased to 15.6 MPa in numerical simulation, which indicated the accuracy of MMC fracture model.

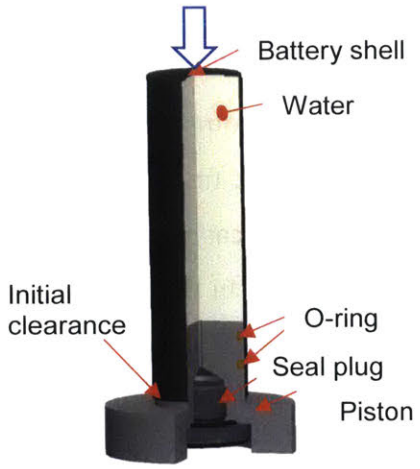


Figure 2-21 Setup of hydraulic bulge test

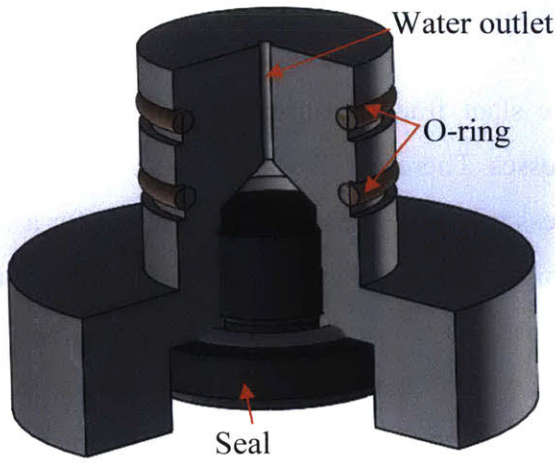


Figure 2-22 Assemble of the piston

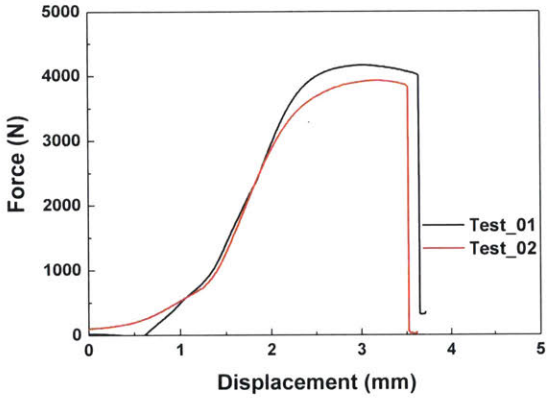


Figure 2-23 Force-displacement curve of hydraulic bulge test

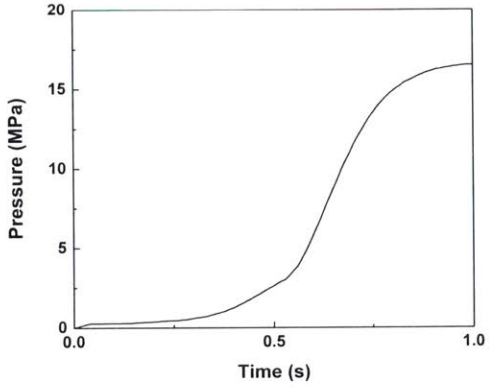


Figure 2-24 Pressure load of FE model

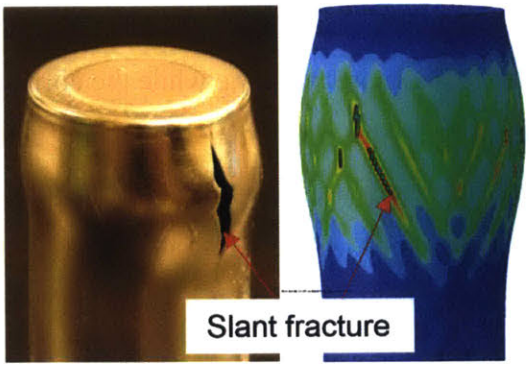


Figure 2-25 Comparison of fracture in test and simulation (contour: plastic equivalent strain)

2.5 Discussion on different types of shear specimens

The slant fracture observed in the hydraulic bulging test results from the local shear stresses. Therefore, the shear tests are very important in determining the fracture locus with stress triaxiality below 0.3. Shear test for a very thin cylindrical shell casing is difficult to design. In-plane shear and torsion tests are two most common tests. In the past, various geometries of in-plane shear specimens, such as butterfly specimens [58,59] and simple shear specimens [25] was used. To obtain unique fracture region, grooved gauge section for shear test were commonly seen, which is not possible for very thin specimens. Four different shear tests were attempted in this research. A butterfly specimen cut along axial direction of shell casing with the same geometry as butterfly tension specimen in Figure 2-12c was subjected to shear test. Local buckling was observed before fracture in Figure 2-26. Torsion test was also considered to determine fracture under stress triaxiality close to zero. Simulation was done before real test that reveled local buckling even for very short 7 mm gauge section (Figure 2-27). A conceptual design of an anti-buckling device for torsion test is shown in Figure 2-28. Two inside steel cylinders and one outside ring are used to prevent both inside and outside buckling. A corresponding simulation was run in Abaqus/Explicit and no buckling occurred by using the anti-buckling device. Such test is planned to be conducted in future. As an alternative, a new type of simple shear test specimen was cut from flattened shell casing according to the geometry from Reyes et al. [63], in Figure 2-29. The gauge section is only 2mm because larger gauge length would bring tension failure instead of shear failure. The comparison of simple shear test result and simulation is shown in Figure 2-30. The force level is almost the same while the corresponding displacement is mismatched. The main reason for the mismatch is that the gauge section developed a complex curvature pattern after machining due to the spring back of the specimen as seen in Figure 2-30. The above three types of shear test are clearly not suitable for thin sheets or shell casing. Lastly, simple shear specimen that is cut directly from shell casing without flattening procedure was used for shear test.

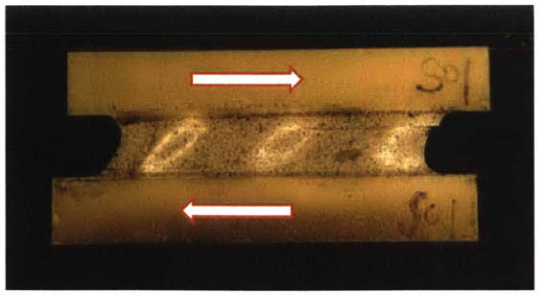


Figure 2-26 Local buckling of butterfly shear specimen

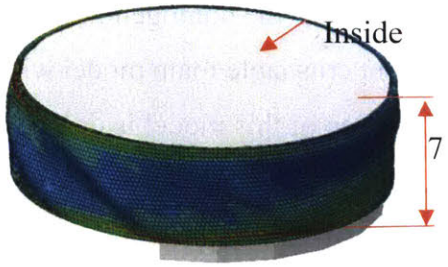


Figure 2-27 Local buckling of torsion specimen in simulation (contour: plastic equivalent strain)

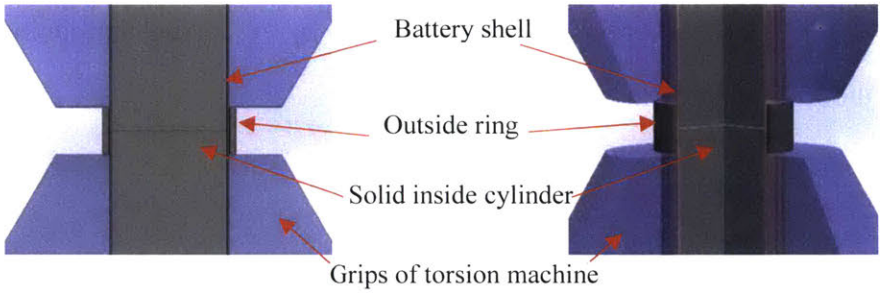


Figure 2-28 Concept design of anti-buckling device for torsion test

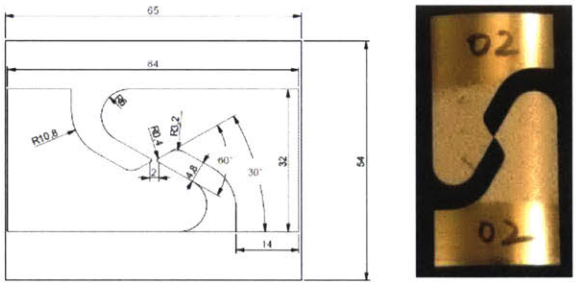


Figure 2-29 Simple shear specimen with geometry scaled from Reyes et al. [62]

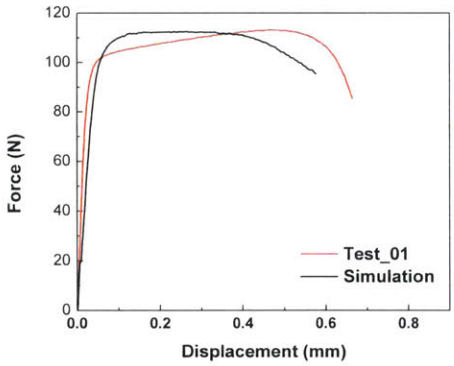


Figure 2-30 Comparison of force-displacement curve of simple shear test

2.6 Application

The shell casing model together with jellyroll model were assembled and applied to predict the 18650 battery under three-point bending and lateral indentation test.

To characterize the homogenized behavior of jellyroll inside the 18650 battery, a pressure-dependent crushable foam model with volumetric hardening in Abaqus was utilized [57]. The yield surface of this model is described by

$$F \equiv \sqrt{q^2 + \alpha(p - p_0)^2} - \alpha \frac{P_c(\varepsilon_{vol}^{pl}) + P_t}{2} = 0 \tag{2-15}$$

where q is Mises stress, p is pressure, p_c is hydrostatic compression yield strength and p_t is tension yield strength which is constant throughout any plastic deformation process. σ_c^0 and p_c^0 are initial yield strength in uniaxial compression and hydrostatic compression. $\alpha = 3k/\sqrt{(3k_t + k)(3 - k)}$, where $k = \sigma_c^0/p_c^0$, $k_t = p_t/p_c^0$. And hardening function $P_c(\varepsilon_{vol}^{pl})$ has the following form

$$P_c(\varepsilon_{vol}^{pl}) = \frac{\sigma_c(\varepsilon_{axial}^{pl})[\sigma_c(\varepsilon_{axial}^{pl})(\frac{1}{\alpha^2} + \frac{1}{9}) + \frac{P_t}{3}]}{P_t + \frac{\sigma_c(\varepsilon_{axial}^{pl})}{3}} \tag{2-16}$$

Where ε_{vol}^{pl} and ε_{axial}^{pl} are volumetric and uniaxial plastic strain and they are equal in uniaxial compression.

The flow potential is defined as

$$G = \sqrt{q^2 + \frac{9}{2}p^2} \tag{2-17}$$

Because of the difficulties in testing the cylindrical jellyroll, the test data from lateral compression of pouch cell in author's laboratory [9] was used by assuming it had similar properties as shown in Figure 2-31. The parameters from jellyroll model is listed in Table 2-31. k is set to 1.1 according to the reference [57] and k_t is optimized from the simulation.

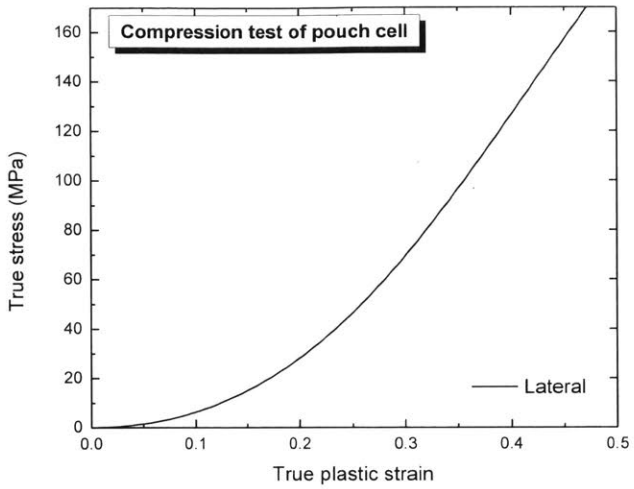


Figure 2-31 Stress-strain curve of jellyroll

Table 2-5 Parameters of jellyroll model

E (MPa)	ν	k	k_t	p_c^0	σ	ε
500	0.01	1.1	10	0.1	piecewise data	

When compared with the harden curve of the shell casing in Sahreai's paper [9], the shell casing studied in above section has exactly the same evolution. Therefore, the whole 18650 battery FE model was built by combining the shell casing and the jellyroll model. The cell model was then adapted to simulate the three-point bending and lateral indentation tests. Figure 2-32 and Figure 2-34 show the good agreements of simulation and test, which indicate the validation of shell casing model. Figure 2-33 and Figure 2-35 show the deformation of the jellyroll and shell casing individually and failure of whole battery from simulation. The effect of shell casing and jellyroll under these two loading conditions were also studied. Jellyroll only yielded at very low force while shell casing gave higher reaction force due to local deformation under three-point bending. However, under lateral indentation, the jelly roll contributed the most resistance compared with that of shell casing. Moreover, since the fracture of shell casing model was calibrated under large range of stress triaxiality, it could be used in complex loading cases as well.

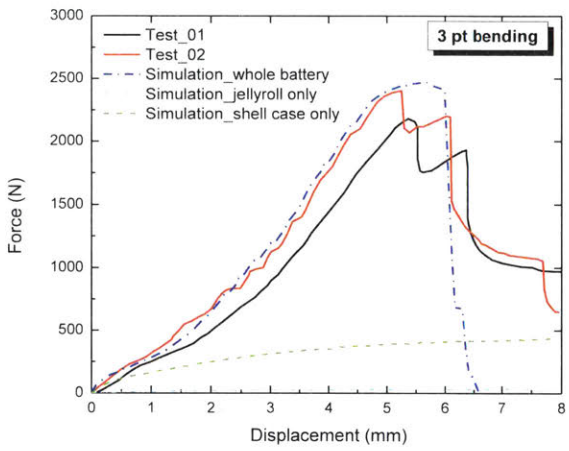


Figure 2-32 Comparison of test and simulation of three-point bending test of 18650 battery

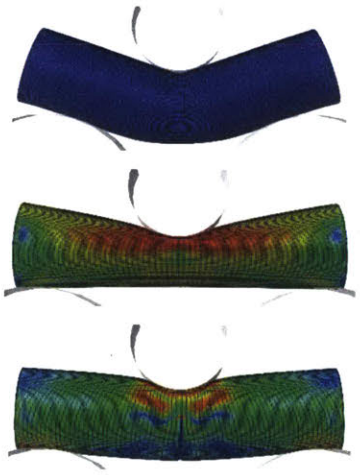


Figure 2-33 Bending of (a) jellyroll only, (b) shell casing only, (c) whole battery

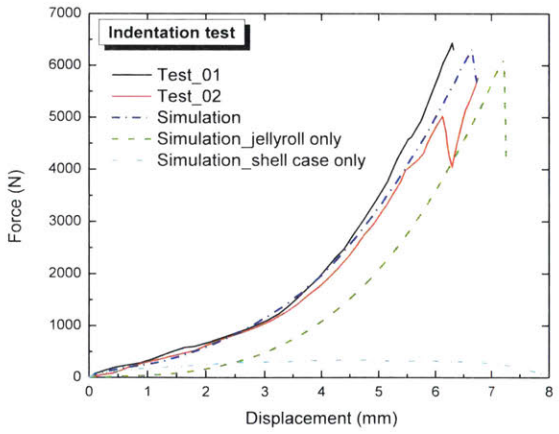


Figure 2-34 Comparison of test and simulation of indentation test of 18650 battery



Figure 2-35 Indentation of (a) jellyroll only, (b) shell casing only, (c) whole battery

2.7 Conclusion

In this chapter, the plasticity and fracture behavior of shell casing of cylindrical lithium-ion battery was studied. Due the original rolled sheet and deep drawing process, non-ignorable anisotropic properties of the shell casing was detected and Hill'48 yield function with associate flow rule was adapted to simulate the plasticity behavior. Modified Mohr-Coulomb (MMC) fracture model was used to predict the onset of fracture. To calibrate the MMC parameters, five types of tests with various combination of stress triaxiality and Lode angle was conducted, including notched tension, central-hole tension, butterfly tension, punch and simple shear with whole shell casing. The tests were performed on specimens cut from the flattened shell casing. The plasticity properties obtained from uniaxial tension and notched tests were shown to predict accurately the response of axial and lateral compression tests of shell casing between two flat plates. Hydraulic bugle test was used to validate the MMC fracture model at the structural level. The battery level validation was done with homogenized jellyroll model. It concludes that the MMC fracture model can be used to simulate fracture initiation of thin metal sheets material in lithium-ion batteries.

Chapter 3

Deformation and Failure Characteristics of Four Types of Lithium-ion Battery Separators

3.1 Introduction

To reduce risk of mechanical and thermal failure of battery cells, Electric Vehicle (EV) battery packs are protected by strong casings outside of the crumple zone. The mechanical and thermal behaviors of the EV lithium-ion batteries under crash loading are intensively studied. Researchers are continuously working on testing and modeling of the mechanical properties of lithium-ion battery cells and their components [8,9,13,54,57,65,66]. While there is a lot of information about strength and failure of these batteries, the exact mechanism of short circuit and conditions leading to thermal runaway are still not clearly understood. Local penetration experiments on pouch cells have produced puzzling results: some cells go to short circuit and thermal events under predictable levels of force and displacement while other cells tolerate much larger deformations without any noticeable failure [66–68]. The mechanical integrity of battery separator is critical for prevention of internal short circuit.

As mentioned in Chapter 1, microporous separators, such as polyethylene (PE), polypropylene (PP) and polypropylene-polyethylene-polypropylene (PP-PE-PP) made of polyolefin, are widely used in the lithium-ion batteries for EVs [39–41]. They can be manufactured by cold and hot stretch of precursor films with different stretch rates and ratios, followed by annealing until achieving a required porosity [39,69–73]. The mechanical properties of separators are highly dependent not only on the material that they are made of but also on their manufacturing processes. The so called wet and dry processes of polyolefin bring significant differences. The tensile strength of separators made from wet process in machine direction (MD) and in-plane transverse direction (TD) is comparable, while it is quite different for dry-processed separators in these two directions.

A better understanding of the mechanical behavior and failure mechanisms of the separators may assist in explaining an apparently conflicting response. Also, it can ultimately help to rank the properties of different types of separators under mechanical abuse loading and choose or design the one that would satisfy specific requirements of a battery pack. There are only few test standards, such as American Society for Testing and Materials (ASTM) D882 for tensile test of thin plastic sheets and ASTM D1306, D3763 for low and high rates puncture tests of separators [74].

In this chapter, four types of commercially available commonly used separators, dry-processed single layer PP separator, dry-processed trilayer (PP-PE-PP) separator and wet-processed ceramic-coated and nonwoven, were studied and their properties were compared. The separators were purchased from MTI Corp, with thicknesses ranging from 16 to 31 μm, as seen Table 3-1. One of the objectives of this thesis was to provide detailed comparison of mechanical strength and failure of these separator in all probable loading conditions. Uniaxial tensile specimens were cut with a range of specimen width from 5 to 25 mm to study the effect of tensile specimen geometry on failure properties. Also a range of punch sizes from 1/8 to 1 inch were used for biaxial tests. Another important result of the present chapter is detection and explanation of two distinct failure mechanisms under biaxial loading. We observed a significant difference in the size of short circuit area under these two failure modes. One implication of this finding is in explanation of the extent of short circuit and thermal reactions when each of these modes are activated. Additionally, the findings explains the so called "soft short" versus "hard short" in the cell subjected to mechanical abuse conditions.

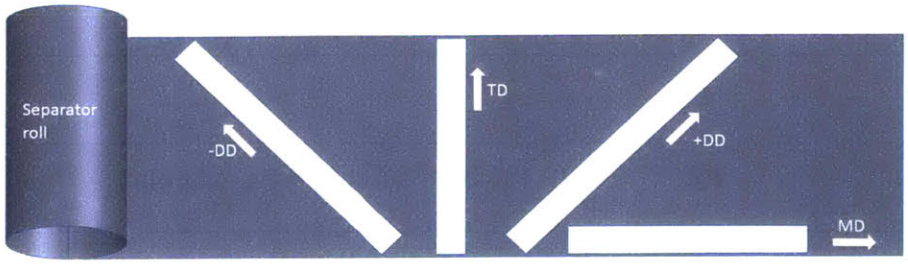
Table 3-1 Separator specifications

	1	2	3	4
Material	PP	PP-PE-PP	Alumina-PE-Alumina	Nonwoven
Process	Dry	Dry	Wet	Wet-laid [74]
Thickness (μm)	25	25	16 (2/12/2)	31
Porosity	36%~46%	39%	37%	46%
Pore size (μm)	0.01~0.1	0.05X0.21	0.1 (average)	0.2 (average)

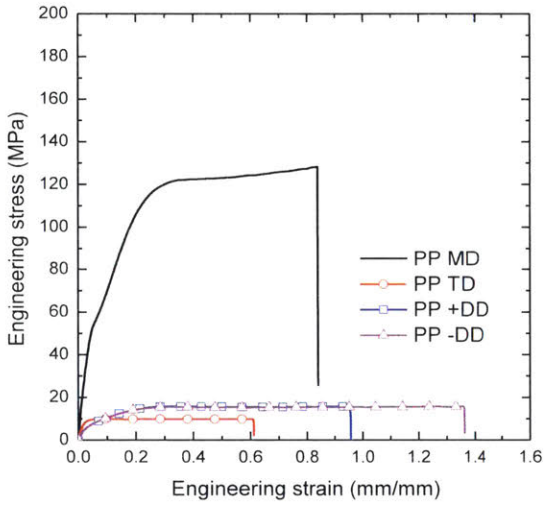
3.2 Experimental methods and results

3.2.1 Tensile tests

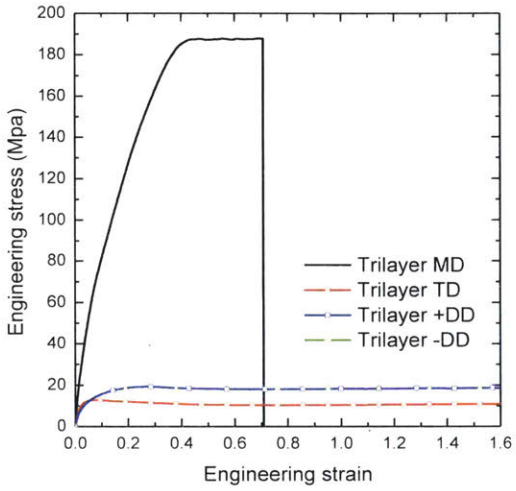
According to ASTM D882 for thin film, the separator should be cut with a uniform width in the range from 5 mm to 25.4 mm. With limited height from original separator roll, the total length of the strip specimen was fixed at 60 mm and gauge length as 35 mm. Since there are no special specifications for the width of strip separator, specimens were cut at five different widths: 5 mm, 10 mm, 15 mm, 20 mm and 25 mm, to study effects of specimen width on deformation and fracture strain. For polymeric separators, which usually do not have visible local necking before failure in uniaxial tensile tests, fracture determines the range of the material's elasticity and plasticity curve. In order to eliminate the edge damage, the separator was sandwiched between 5-mm Cartesian graph paper for cutting to have enhanced precision for the width and improve quality of cut. A sharp razor was used to cut specimens along machine direction (MD), transverse direction (TD) and two diagonal directions (+DD and -DD), as shown in Figure 3-1a. An Instron 5944 uniaxial tensile machine with 100N load cell and a constant 25 mm/min speed was used to perform the tests. The main concern of picking 25 mm/min is to finish the test in less than 10 min, even though in some tests of dry-processed separators along DD/TD, it is



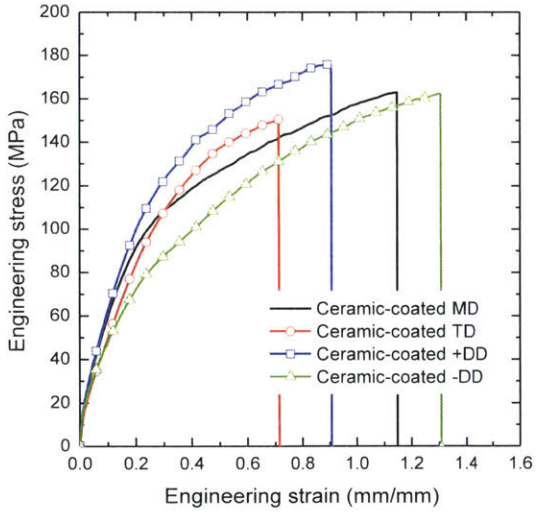
(a)



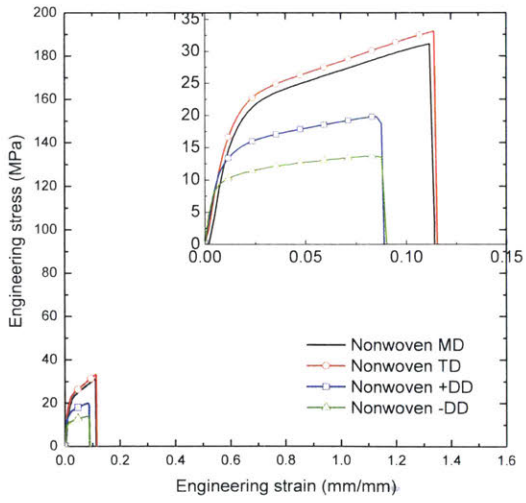
(b)



(c)



(d)



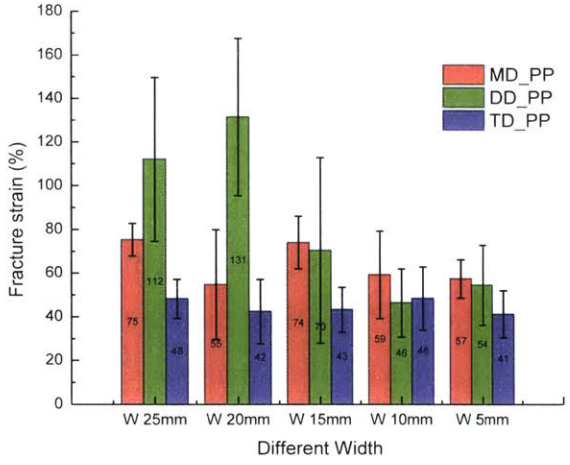
(e)

Figure 3-1 (a) Illustration of MD, TD, +DD, -DD a separator roll; nominal stress-strain of (b) dry-processed PP separator, (b) dry-processed trilayer separator, (c) wet-processed ceramic-coated separator, (e) nonwoven separator in the four directions

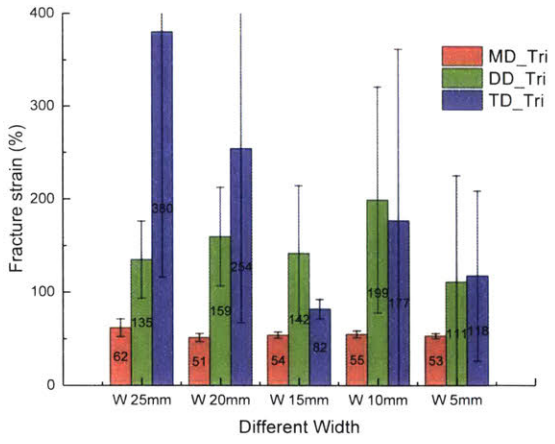
possible to go beyond 10 min. Digital image correlation (DIC) method (Vic 2D, 2009) was used to calculate the strains. Figure 3-1b shows test results for all types of separators studied, in four directions. For dry-processed PP and trilayer separators, the response is highly anisotropic. The strength in MD (>120 MPa) is much larger than that in DD and TD (<20 MPa). The strengths in –DD and +DD are identical. The wet-processed ceramic-coated one has comparable stress levels in four directions (>140 MPa), though the initial elastic moduli are different. The nonwoven separator has much lower strength (<35 MPa), which is similar in TD and MD, while it is weaker along DD, mainly due to the orientation of fibers. Its failure stress and strain levels are approximately five times smaller than the polymeric separators. It is worth pointing out that the stress-strain curves along +DD and –DD are different for ceramic-coated and nonwoven separators.

The fracture strains for specimens with different widths in each direction are compared in Figure 3-2a (+DD and –DD are combined as DD here). The standard error bar shows a large spread of the fracture stain with different widths. From these tests, we have found that: a) fracture strains of all the four separators in DD have relatively large variations; b) compared to the other three, wet-processed ceramic-coated separator has smaller variation of failure strain; c) the smaller the width of specimen is, the larger the variation due to cutting defects.

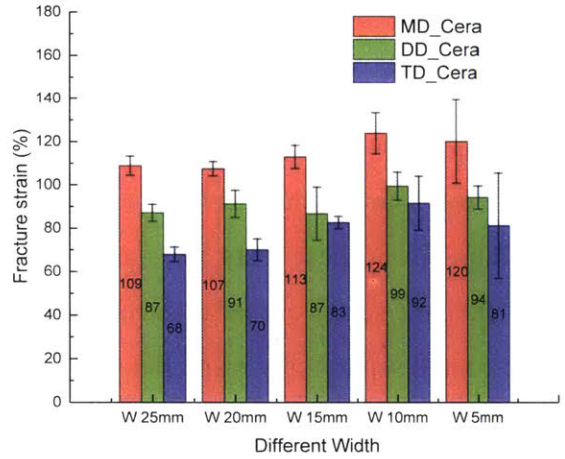
For dry-processed separators, the failure modes are quite different in MD, TD and DD, as shown in Figure 3-2b. The failure during MD loading of these two separators created zig-zag failure surfaces perpendicular to MD while failure surface in TD loading is much smoother. Stretch-induced wrinkling perpendicular to loading direction was observed for the TD and DD tensile tests of PP and trilayer specimens. The wrinkles and folds are due to clamped boundary conditions and only happens at certain range of tensile strains [75]. DD loading is characterized by large shear zones and extreme fracture strains. In large strains, the deformed regions of specimens in TD and DD became transparent (the un-deformed separator was solid white). The differences in failure modes of dry-processed separator in two directions is extensively discussed in Chapter 4. For the ceramic-coated separators, deformed shapes are similar in all three directions, characterized by a smooth necking area



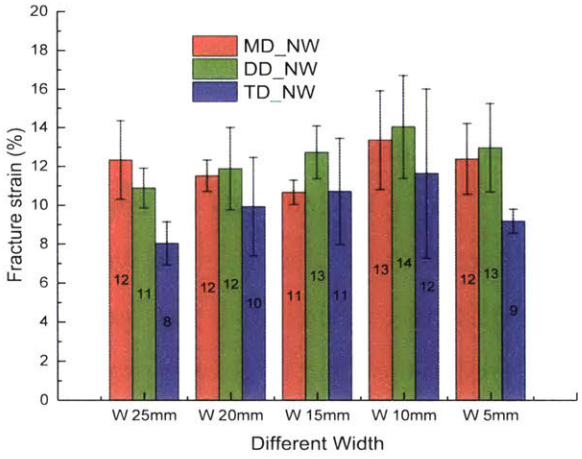
PP



Trilayer



Ceramic-coated

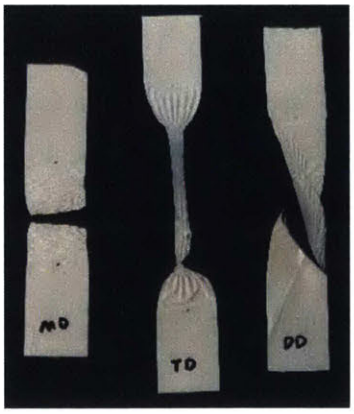


Nonwoven

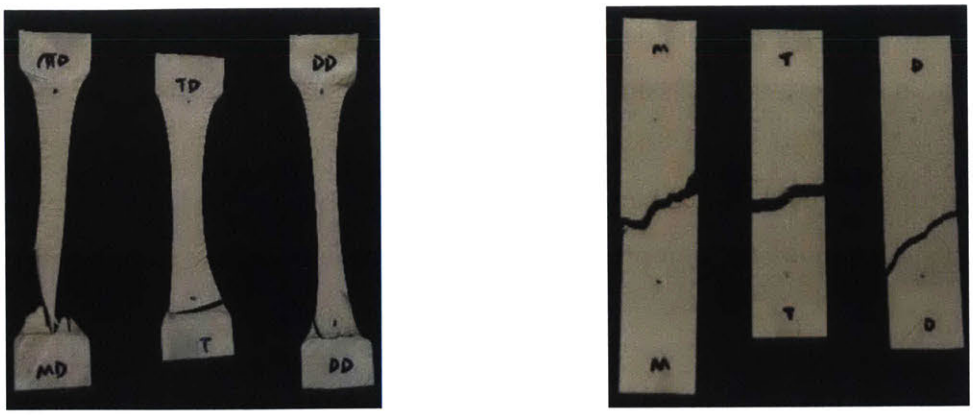
(a)



PP



Trilayer



Ceramic-coated Nonwoven

(b)

Figure 3-2 Comparison of failure strain and failure mode in MD, TD, DD in uniaxial tensile test. (a) comparison of fracture strain; (b) different failure modes in MD, TD, and DD (from left to right)

in the center of specimen. The nonwoven samples have minimal change of shape during loading as they fracture in relatively small strains ($\epsilon_f < 0.12$).

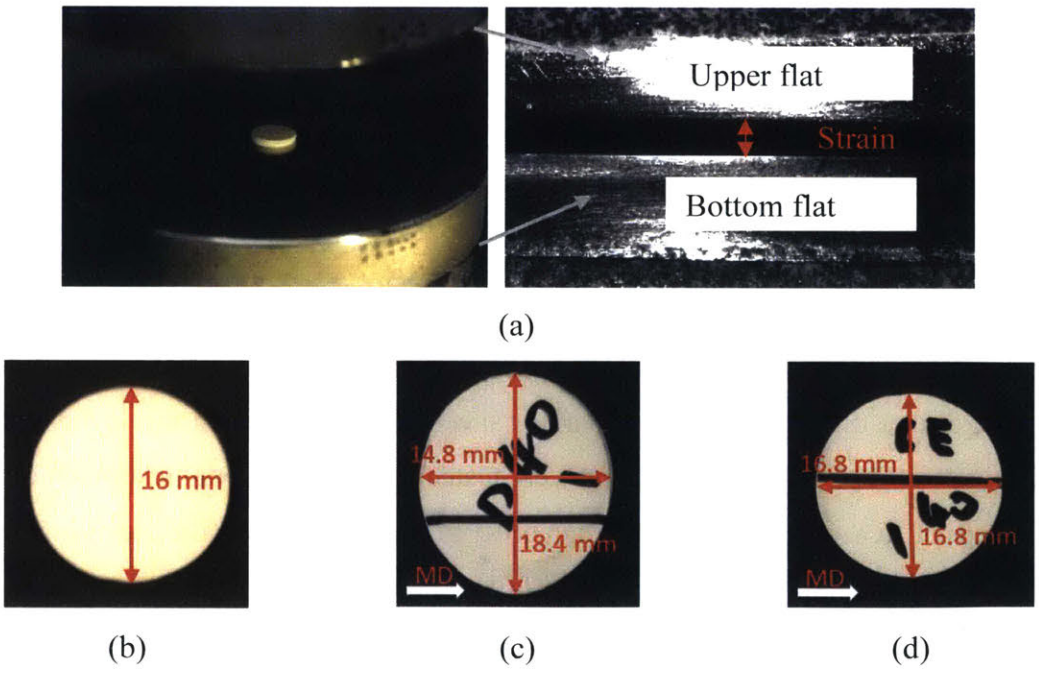
From the above observations, in order to characterize a new separator type, it is recommended to cut strips at four directions (MD, TD, +DD and -DD). In terms of width of the specimen, more reliable data is obtained when the width is 10 mm or larger.

3.2.2 Compression tests

For the compression tests, samples (40 layers) were cut by 16 mm diameter hammer-driven hole punch at one time from folded separator sheets to ensure that all the layers had the same orientation. The stacked specimens were tested in a MTS uniaxial test machine with 200 kN load cell at a strain rate of 0.012 /s in order to have the same strain rate as in uniaxial tensile tests. A pre-compression of 0.5 MPa (following Ref [76]) was used to make sure there were no gaps between the layers, which is slightly larger than the practical stack pressure of 0.2 MPa for pouch cell according to A123's user document [77]. Tests were repeated five times for each type of separator. The loading was applied to 100 MPa stress and was followed by unloading to zero stress. It is very important to mention that usage of DIC is

very crucial to get reliable strain data since the total thickness of the stacked layers is even less than 1 mm with pre-compression. By comparing the compressive stress-strain response with different layers, 10, 20 30, 40 and 50 layers, respectively, it is found that samples with layers of 40 and 50 yield almost identical results, which is consistent with Ref [76]. Figure 3-3 shows the test setup of the compression test and the samples before and most tests.

The nominal stress-strain curves and shapes of deformed round specimens are shown in Figure 3-4. While dry-processed PP (Figure 3-4) and trilayer separators deform to an oval shape with major axis along MD, the ceramic-coated (Figure 3-4) and nonwoven separators, remained round after the tests. This is mainly due to the high in-plane anisotropy of the dry-processed separators versus relatively isotropic behavior of wet-processed ceramic-coated and nonwoven separators. Relatively large differences were found in the stress strain curves between these four separators. While the polymeric dry-processed separators experienced obvious yield points, the ceramic-coated and nonwoven separators did not show similar trends under the applied compression force level in the tests. When loaded to



(a)

(b) (c) (d)

Figure 3-3 Compression test experiment. (a) test setup and image from DIC camera; (b) specimen before test; (c) PP separator after test; (d) ceramic-coated separator after test

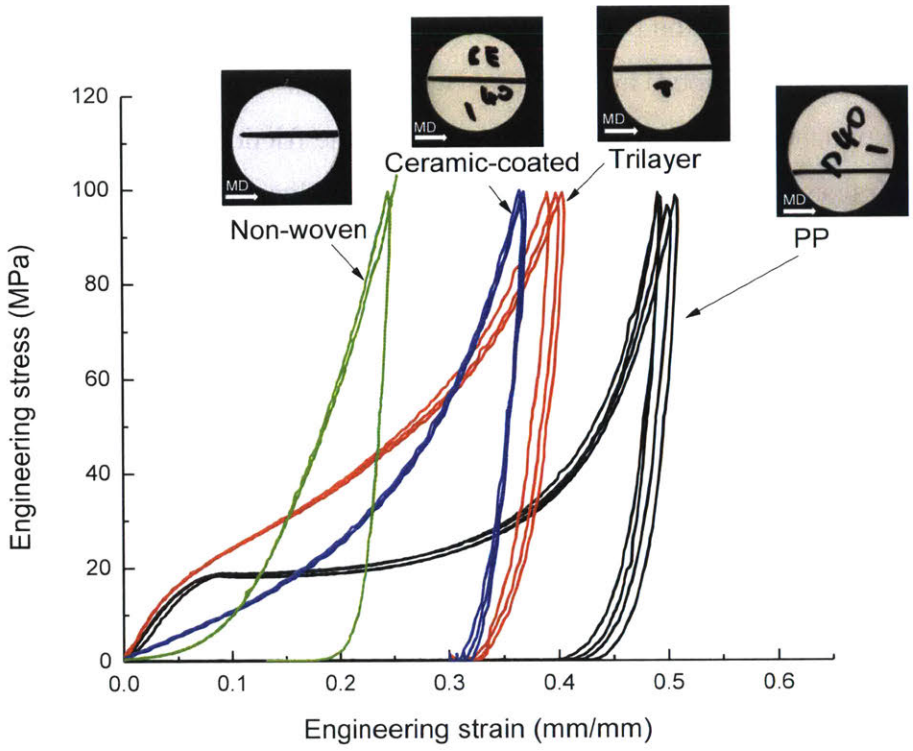


Figure 3-4 Nominal stress strain curves of the four separators

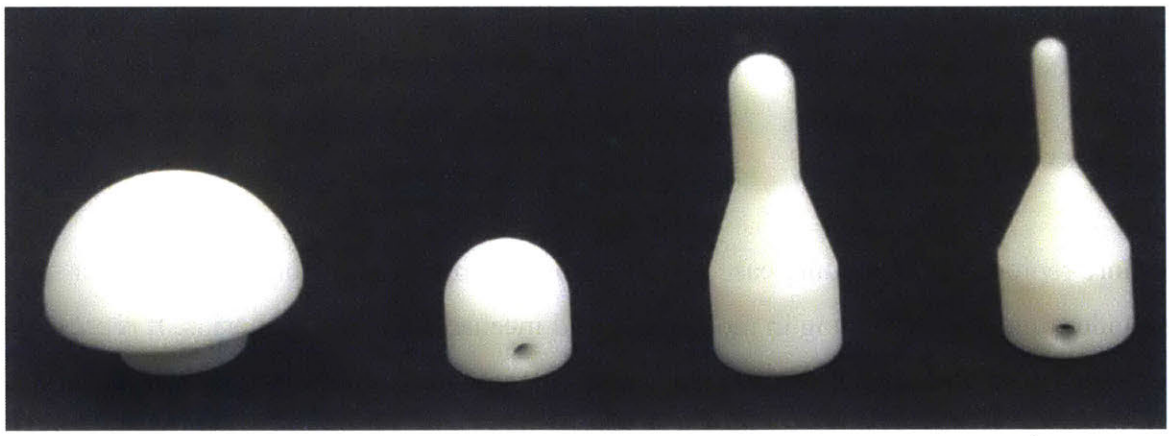
the maximum value of 100 MPa, the nonwoven separator had the smallest strain followed by ceramic-coated separator. The PP separator held the largest strain to reach the peak force value. After unloading, only small rebound of material was observed.

3.2.3 Biaxial punch tests

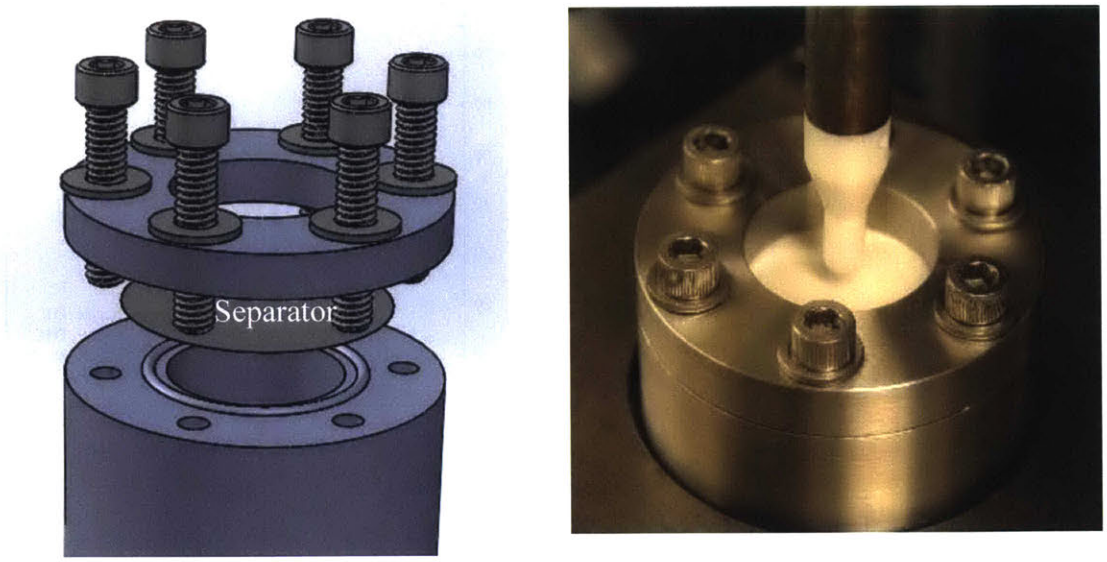
A more representative loading case for separators is a punch intrusion. The separator may go under this kind of loading in most real world mechanical abuse scenarios. It represents combined in-plane biaxial tension and out-of-plane compression. A punch tests with a small radius punch head is one of the standard abuse test for lithium-ion battery separators. It is performed with a punch of 3.2 mm in diameter according to ASTM F1306-90, and usually referred to as a puncture test [78]. Punch test can eliminate the errors induced by imperfections on the edge due to cutting method, and thus provide a good estimate of material properties and failure strains.

Figure 3-5 shows a view of the biaxial punch test setup. Round specimens cut from each separator were tightly griped in a fixture with interior diameter of 32 mm. Four hemispherical punches, made out of Teflon to reduce the friction, were used to apply the loading. Punch tests were carried out with a punch head diameter of 25.4 mm, 12.7 mm, 6.4 mm and 3.2 mm. These tests were performed with an Instron Tabletop loading frame at a speed of 12 mm/min to ensure a comparable strain rate level as uniaxial tensile at onset of failure. The 100 N load cell was used for all tests except the test of ceramic-coated separator with 1 inch punch, which required a larger load cell (2 kN).

Figure 3-6a-d compares the force displacement curves of each separator with different sizes of punch head. The nonwoven separator has the smallest punch strength (5-20 N) among the four separators due to its short fibers. The wet-processed ceramic-coated separator has the highest punch strength (19-160 N) since it is strong in both MD and TD, and the trilayer separator (8-90 N) behaved better than PP (4-30 N) in terms of punch strength. Figure 3-6e-h compares the images of the separators onset of failure. From the experiments, a slit along the MD was commonly seen for PP and trilayer separators with larger punch heads.



(a)



(b)

Figure 3-5 Biaxial punch test setup. (a) teflon punch head with diameter of 25.4 mm, 12.7 mm, 6.4 mm and 3.2 mm (from left to right); (b) biaxial loading fixture

For the ceramic-coated and nonwoven separators, the failures were more local and had a round shape right under the punch. The failure region in each case can give a hint about size of possible short circuit area when each of these separators would fail in a real cell under mechanical abuse. The short circuit area produced due to failure of wet-processed ceramic-coated separators and nonwoven separators is expected to be much smaller than the one created due to slit failure of dry-processed separators. It should be noted that dry-processed separators can have complex failing scenarios with smaller punch sizes.

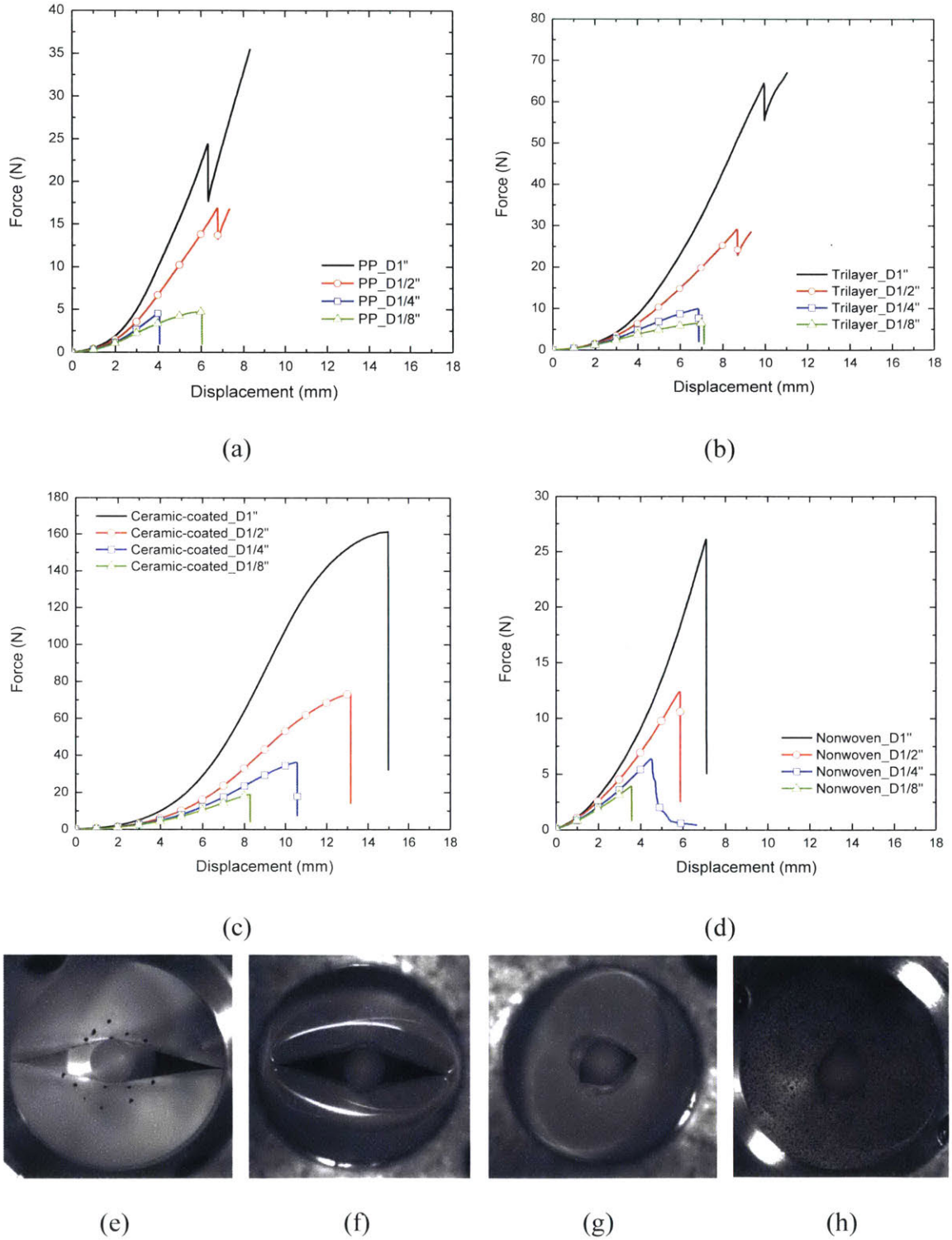


Figure 3-6 Force-displacement curves of punch test (a) PP, (b) trilayer, (c) ceramic coated, (d) nonwoven and separators after failure (e) PP, (f) trilayer, (g) ceramic coated, (h) nonwoven (punch head diameter: 1/4 inch)

3.3 Two failure modes in biaxial punch loading

SEM image (Figure 3-7a) showed that separator under punch loading gets both effects of TD and MD tensile loads. Formation of new fibrils in the bulk material regions is an effect similar to MD uniaxial loads, while opening of the pores is seen in TD loading.

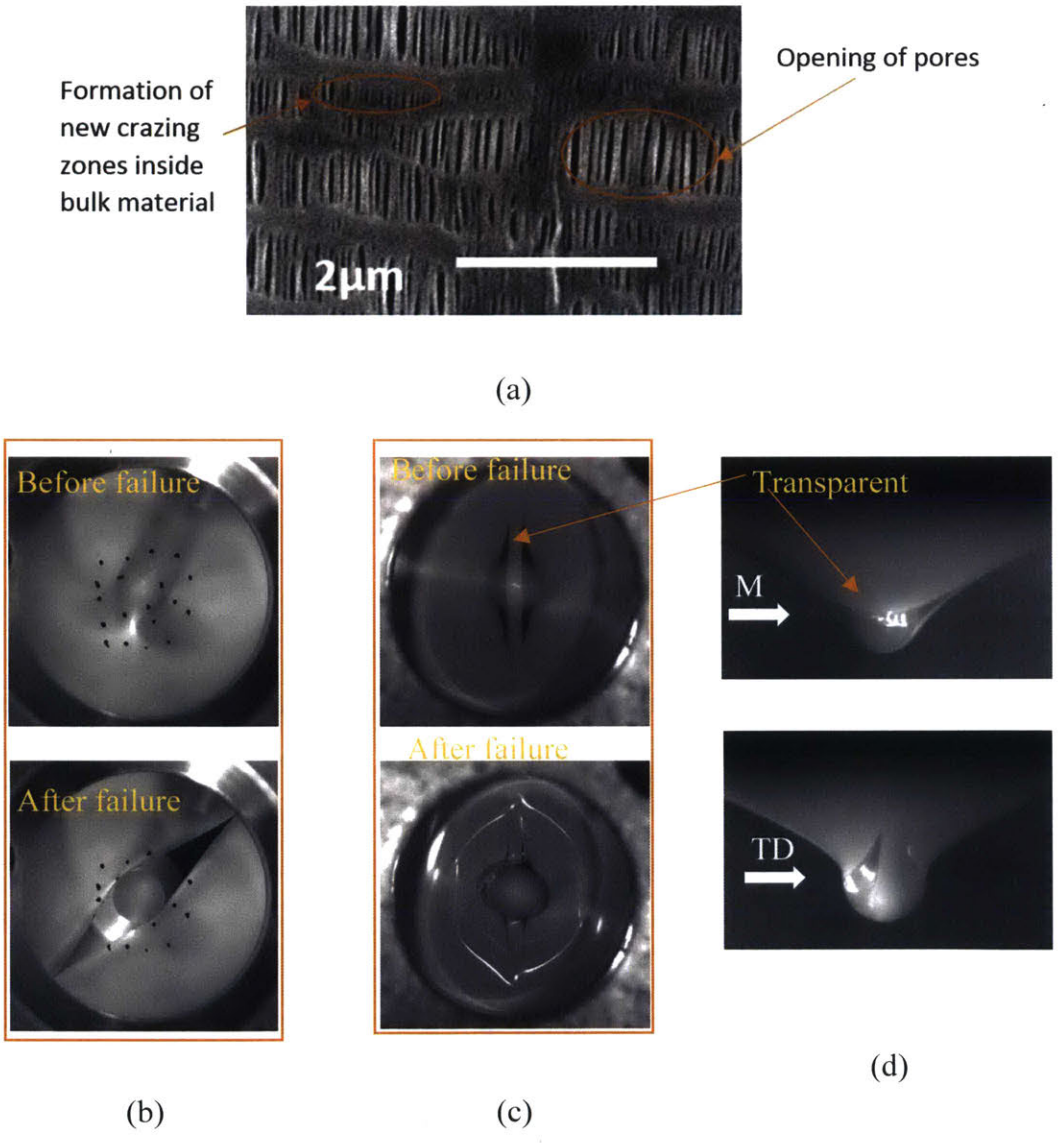
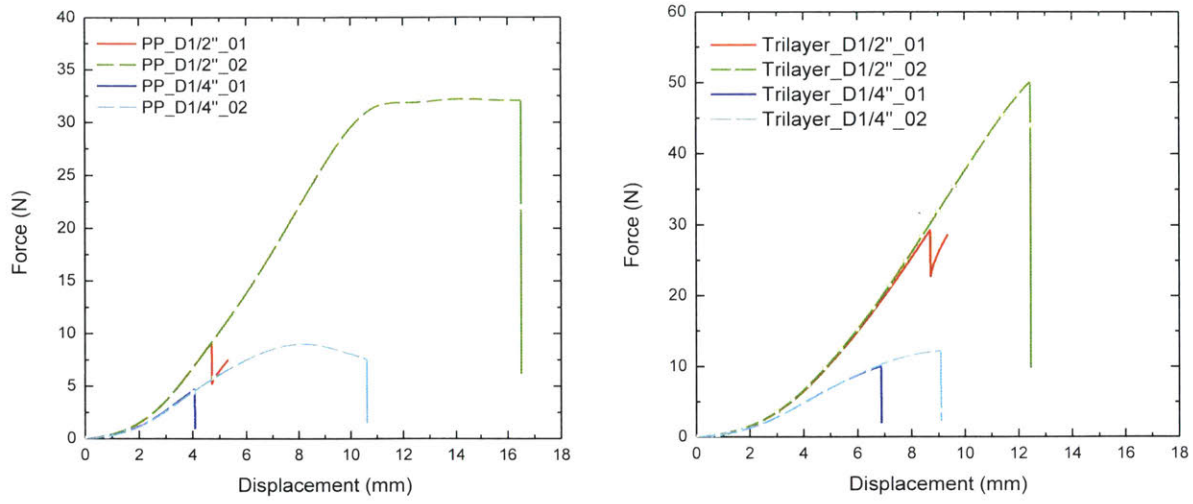


Figure 3-7 SEM image and Photos of separators under punch loading. (a) SEM image of PP separator; (b) Mode A Failure; (c) Mode B Failure; (d) additional views of transparent area before failure in Mode B

An interesting observation was that two different failure modes co-exist for dry-processed separators, as shown in Figure 3-7b-c. In the first and more common one (named failure Mode A, seen Figure 3-7b), the cracks form along MD, featuring a large diagonal slit. The smooth surface of the tear along MD for this failure mode is similar to what was observed in uniaxial TD loading cases in Figure 3-1b. The other failure mode creates a zig-zag surface along TD (named failure Mode B, seen Figure 3-7c), similar to what was observed in uniaxial MD loading cases in Figure 3-1b. Failure Mode A happens under a smaller punch force and lower punch displacement. The sample would reach failure Mode B only if it passes force and displacement levels associated with Mode A without failure. However, a transparent section is formed along MD when the forces and displacements reach values corresponding to Mode A, see Figure 3-7b. The differences in curvatures of deformed shape from side views along MD and TD clearly show effect of high anisotropy.

Figure 3-8ab show the force displacement curves of each separator with different sizes of punch head. Specimens failed in Mode A are shown with solid lines and the ones failed in Mode B are shown with circular symbols. In each punch size, a failure in Mode A is associated with much smaller force and displacement, when compared to a Mode B failure. While the tests were repeated five times, in this figure only one representative sample curve from each failure mode case is plotted to keep the figure clear. For the PP separator, with the punch diameter of 1 inch (25 mm), all the five specimens failed in Mode A. When the punch head size decreased to ½ inch (12.5 mm) diameter, three out of five specimens failed in Mode A, and two of them failed in Mode B. With punch head diameter of ¼ inch (6.4 mm), only one specimen in five repeated tests failed in Mode A and the rest failed in Mode B. With punch diameter of 1/8 inch (3.2 mm), all the five specimens failed in Mode B. We observed similar trends for the trilayer separator.

A relatively free flow of the material that is in contact with the punch head is needed to allow deformation beyond Mode A, without localization in one point of the stretched transparent section, until reaching Mode B. This was accommodated in the above tests due to use of Teflon punch heads which eliminated friction. For large punch heads, it is not easy to allow all the material under the punch head to flow freely and deform relatively "uniformly". Therefore failure Mode B is mostly observed only in smaller punch sizes.

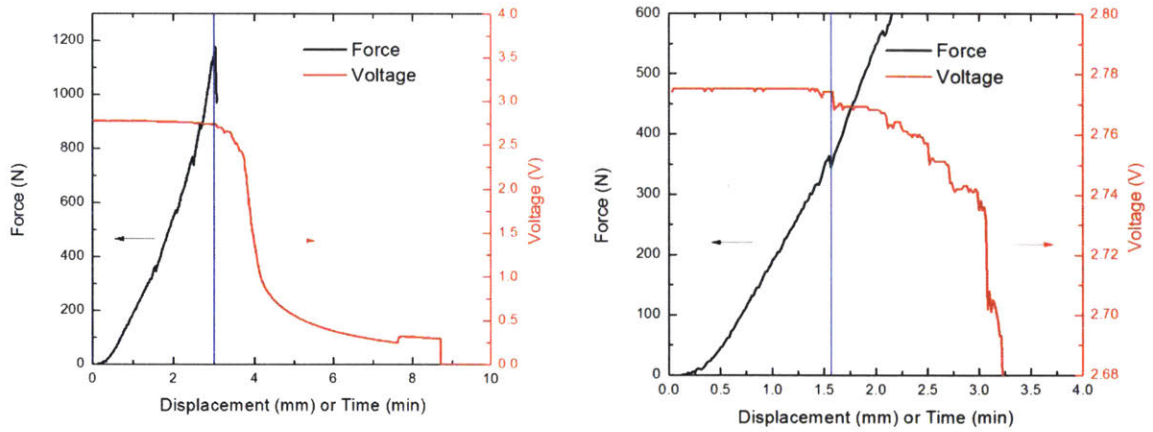


(a) (b)

Figure 3-8 Force-displacement curves from punch loading of PP and trilayer separators with different punch sizes. (a) PP separator; (b) trilayer separator

3.4 Discussion on formation of distinct short circuits

Soft verus Hard Short Circuit: In punch test of the whole battery cells, due to the friction from cathode and anode particles, the separator is mostly expected to fail in Mode A, and not to reach Mode B. Friction would lead to an instant localization with the start of thinning and appearance of transparent section. However, failure in Mode B could be observed in extremely small punch sizes (pin or needle tests). To understand whether a cell that has not failed in Mode A is still safe, we would like to discuss a full cell experiment previously reported by Sahraei et al. [66]. The authors performed punch tests with various punch sizes on different pouch cells until detecting a short circuit from drop in punch force and cell voltage. While peak force and displacements to failure usually followed a linear trend with punch size, it was observed that in a conical punch (smallest punch) test of a large pouch cell, the peak values were much beyond what was expected for that punch size. With the new understanding about two failure modes discussed above, this cell is presumed to have had a separator failure in Mode B, while all other cells had it failed in mode A. As shown in Figure 3-9a, in this test, short circuit was detected at a force of 1200N and punch displacement of 3 mm.



(a) (b)

Figure 3-9 A hard short easily detected at 3 mm displacement (a), original global curve; versus a soft short at 1.5 mm displacement (b), zoomed voltage

Scrutinizing in the cell voltage with a higher precision showed that a small decrease in voltage had started around the force and displacement values which corresponded to a Mode A failure, based on other cell tests with larger punch sizes. The authors concluded that a soft short had started at that point. The soft short was not detected as a failure, and loading continued until much larger force levels and presumably Mode B failure of the separator. This means that failure Mode A is of an utmost importance: it can trigger soft shorts due to thinning and probable opening of the pores in the transparent area, without causing a full detectable failure in the cell.

Extreme versus mild thermal events: The two failure modes may also provide some explanation about lack of repeatability in nail penetration tests, when in some tests cell may fail in Mode A and in some it could fail in Mode B. In Figure 3-10, we have highlighted the geometry of possible contact between materials on two sides of a separator when it fails in Mode A versus that in Mode B. The much larger contact area due to a Mode A failure may result in a much more violent thermal event in this case when compared to the small area seen in Mode B failure.

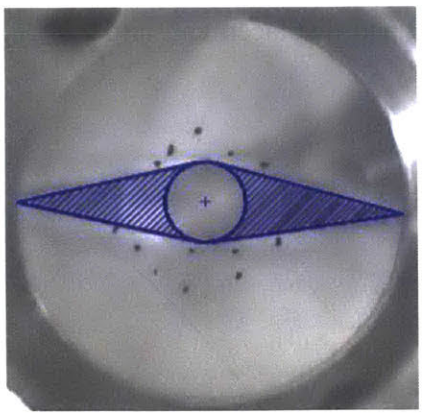
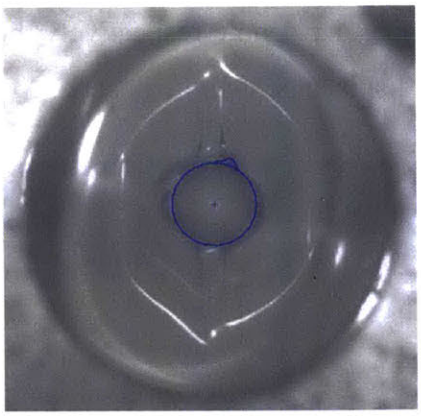
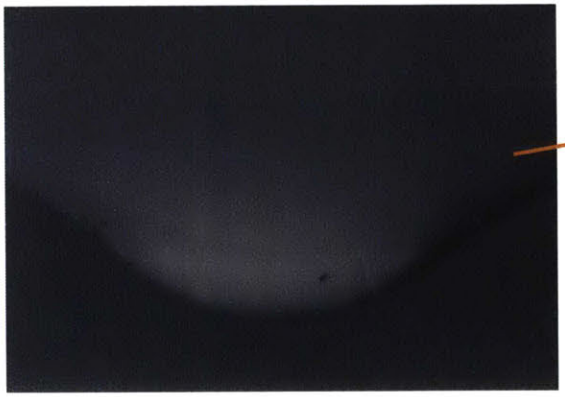



Figure 3-10 Short circuit area due to Mode A failure (a) left, versus the area in a Mode B Failure (b) right

Separator Failure Criterion: For the design purpose, where a proper measure should be chosen for optimum protection against deformation, it is important that the displacement leading to onset of Mode A is used as failure criterion. Otherwise the cell can undergo a soft short without detection. While some punch tests can lead to failure in Mode A, and therefore determining the load-displacements associated with Mode A would be directly possible, in the cases of tests leading to Mode B failure, it is harder to estimate what the values for Mode A failure would be. To develop a failure criterion, the onset of thinning and formation of transparent area under the punch should be detected. We looked very closely into this by reviewing magnified images of the contact area under the punch in order to detect this point (see Figure 3-11). We discovered that the onset of thinning observed from the tests could be detected on the load displacement curve from a change in convexity, i.e. by the inflection point. The peak value in the slope of force-displacement curve, as shown in Figure 3-11 with a red curve, shows the point of inflection which is where a thin and transparent area in the separator starts to appear. According to these findings, the critical displacement corresponding to the onset of failure point A can be calculated from:

$$\frac{d^2 f(x_{Mode\,A})}{dx^2} = 0 \quad (3\text{-}1)$$

where f and x denote respectively the punch force, and displacement, and $x_{Mode\ A}$ is the punch displacement at the onset of Mode A failure.



Start of thinning and formation of transparent section under punch

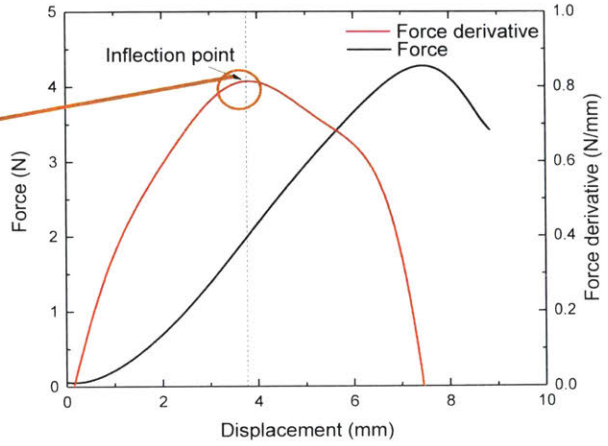


Figure 3-11 Onset of thinning and formation of transparent area in the PP separator

3.5 Conclusion

While uniaxial tests show significant anisotropy for dry-processed PP and trilayer separators, nonwoven and wet-processed ceramic-coated separators have much lower anisotropy. This was also evident in compression tests where the circular shape of PP and trilayer separators turns oval after the test, while this area remains circular for wet-processed ceramic-coated and nonwoven separators. A comparison of strength of these separators under uniaxial and biaxial punch tests showed that wet-processed ceramic-coated separators had the highest strength, while the nonwoven separator was the weakest among all. Uniaxial and biaxial tests also provided information about failure mechanisms in separators. Each type of separator has a distinct failure signature. Ceramic-coated wet-processed separators and nonwoven separators create local and relatively small round areas of failure under the punch which would cause smaller short circuit areas when compared to dry-processed separators which their failure results in large slits after failure.

Dry-processed separators, currently widely used in commercial batteries, have two different failure modes. Understanding of these failure modes and their characteristics gives insight about inconsistent nail penetration results, where a failure in Mode A can

result in extreme thermal event, but a repeat of the test leading to failure Mode B can be much less eventful. Additionally, a criterion for displacements that a separator can tolerate without having a soft failure was proposed. It could be used to design cell manufacturing procedures or battery protective structures while keeping in mind level of tolerance of separator without creating a soft short area.

Chapter 4

Deformation Mechanism and Numerical Modeling of Dry-processed PP Separator

4.1 Introduction

The comparison of mechanical properties of four types of separators under uniaxial tensile, through thickness compression and biaxial punch in Chapter 3 provides the useful macro level properties for numerical simulation of separators. However, from these tests, local deformation sequence and deformation mechanism of the micro fibrils, as seen in Figure 1-7, is still not revealed. Generally, separators that are made from different manufacturing processes have different micro structures. Among them, the dry-processed separator is more common in the past and recent years [79]. According to Goldman Sachs [80] and a market survey by China SPIR, dry-processed separator is still dominating the market, while the market of wet-processed separator is expected to grow in the coming years. Thus, in this chapter, the single layer dry-processed PP separator is carefully characterized and the methods also work for other types of separators.

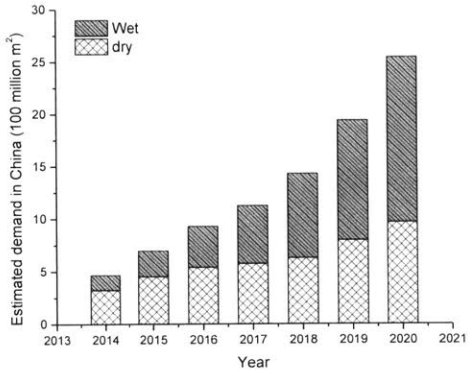
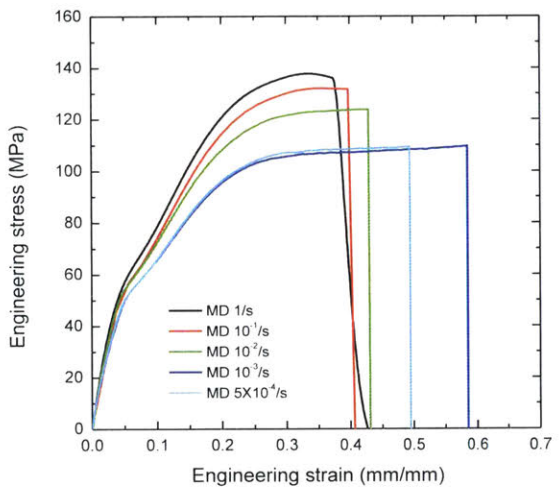


Figure 4-1 Market size prediction of wet and dry-processed separator in China (data from qb-lib.com)

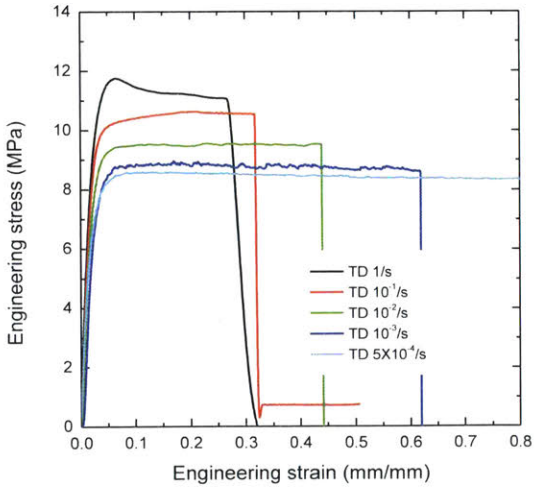
The mechanical properties of PP separators under tensile, compression and punch has already been listed in previous chapter. This chapter is focused on characterization of PP separator in terms of the strain rate and temperature properties and micro level deformation mechanism.

4.2 Strain rate and thermal properties of PP separator

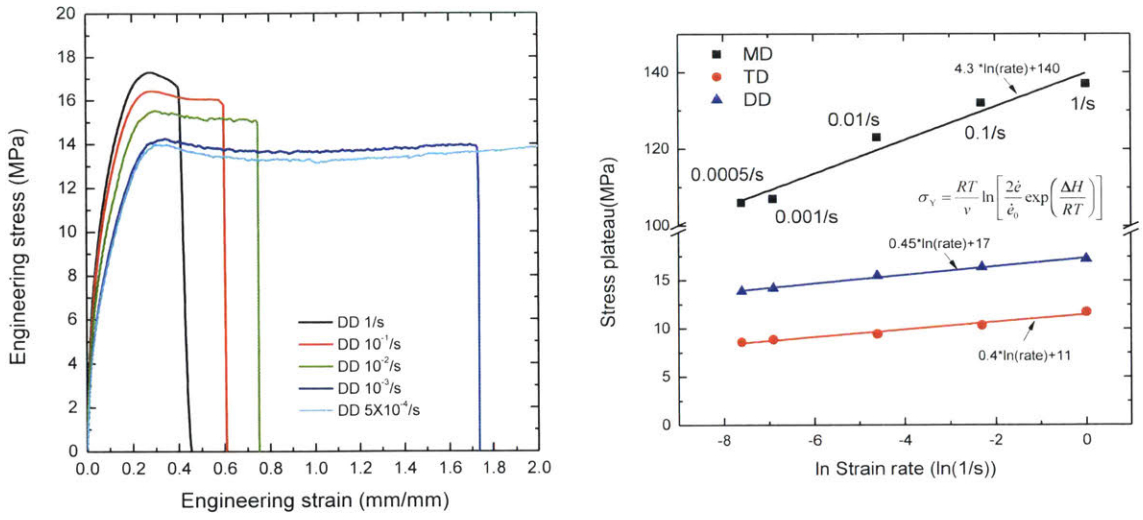
Polymers are viscoelastic materials in nature. The separators inside lithium-ion batteries experience different deformation rate under normal charge-discharge operation and under crash loading. The strain-rate effect should be taken into account when it comes to numerical modeling of dynamic performance of lithium-ion cells. Strip specimens with width of 10 mm similar to Figure 3-2, were tested with strain rate of 5×10^{-5}/s, 10^{-4}/s, 10^{-3}/s, 10^{-2}/s, 10^{-1}/s. Each test scenario was repeats five times. Instron Tabletop machine with small grips (weight: 3.4 N) was used to reduce the grips' inertial effect. The engineering stress strain curves in MD, TD, DD with the above strain rates are shown in Figure 4-2. The second yield point was chosen as stress plateau to illustrate the effect of strain rate in Figure 4-2d. The stress plateau has a linear relationship with natural logarithmic of strain rate, which is commonly seen among thermal plastics [81].



(a)



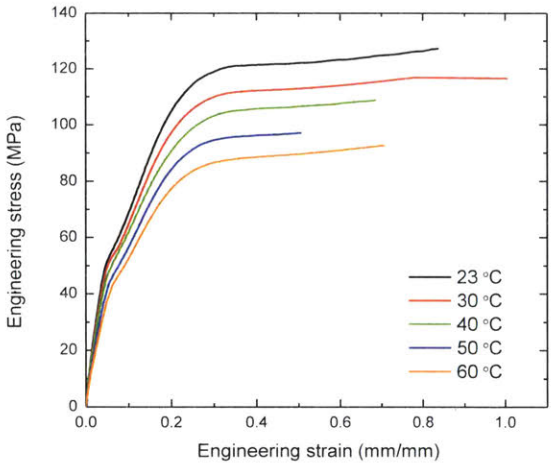
(b)



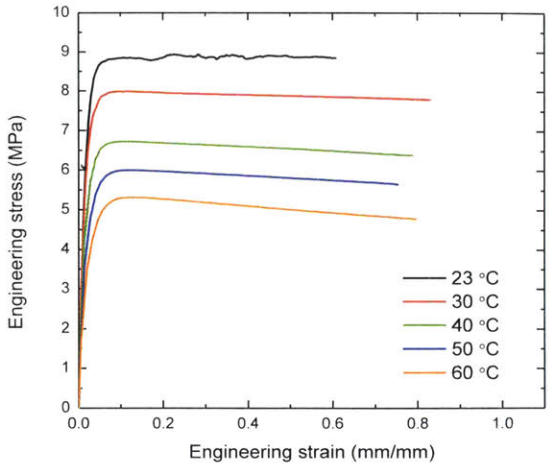
(c) (d)

Figure 4-2 Strain rate effect in MD, TD and DD of PP separator. (a) MD; (b) TD; (c) DD; (d) summary of strain rate effect

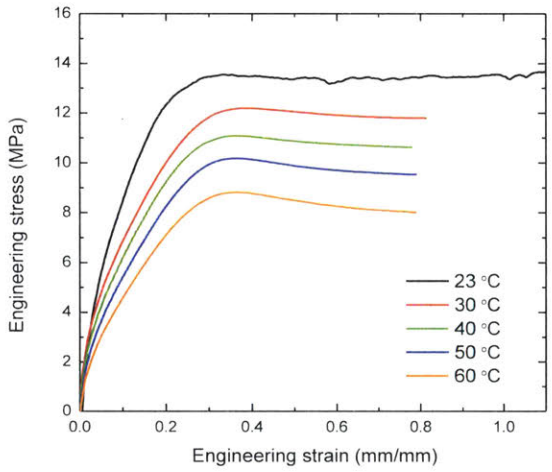
The temperature inside cell under large discharge could rise to 45 °C or even 60 °C, which will shorten the life of cell [82–87]. Dynamic mechanical analyzer (TA instrument Q800 DMA) was used to characterize the mechanical properties under different temperatures. Strip specimens with width of 5 mm and length of 30 mm with same method in Chapter 3, in MD, TD and DD direction (total 60 specimens). The test speed is set to 10.7 mm/min according to the change in gauge length from 35 mm to 15 mm due to the limitation of travel distance of the DMA. Stress strain curves under 25 °C, 30 °C, 40 °C, 50 °C, 60 °C are shown in Figure 4-3. Strong temperature dependent effect was found for PP separator. The decrease of loss modulus in Figure 4-4a at around 0 °C may indicate the α relaxation (glass-to rubber relaxation) since the glass transition temperature is between -20 °C and -10 °C, which also agrees with results by Xu et al. [88]. The sharp drop of the tangent phase lag around 160 °C is the meltdown of PP separator. For the common working temperature from 25 °C to 45 °C, as seen in Figure 4-3 and Figure 4-4, there is still significant decrease of elastic modules.



(a)



(b)



(c)

Figure 4-3 Stress strain curve of PP separator in MD, TD and DD under different temperatures. (a) MD; (b) TD; (c) DD

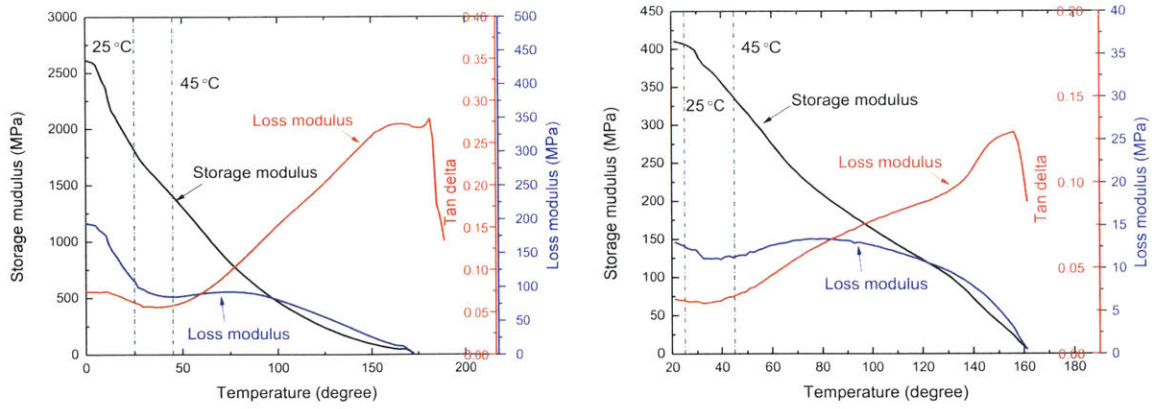


Figure 4-4 Temperature dependence of storage modulus, loss modulus and tangent delta in MD and TD. (a) MD; (b) TD

4.3 Chemical bond characterization and crystalline orientation

The PP separator is highly anisotropic porous semi-crystalline film due to the orientation of the crystalline and amorphous structure. With Thermo Fisher Continuum Fourier Transform Infrared Microscope (FTIR), the absorbance peaks in Figure 4-5 are related stretch and bending of carbon-hydrogen bonds and carbon-carbon bonds [89]. By comparing the peak of isotactic PP from Luongo [90], the FTIR peaks of the PP separator matches the peaks relatively well and tells the PP separator is made from isotactic PP, which was also reported in literature [43,91].

The X-ray diffraction (XRD) is widely used in determining the crystalline orientation of polymer film. Here we use MIT SAXSLAB Small Angle X-ray Scattering System and the diffraction pattern are in Figure 4-6. The radiation wave length is 1.5409 Angstroms ($CuK_{\alpha 1}$). From wide angle XRD, the 110 plane is oriented slightly more along MD while 040 plane and 130 are largely along MD. The 111 and 131 plane are somehow overlapped and not oriented along MD, confirming the results of Tabatabaei et al. [47]. Following their method, long period distance, L_p, could be estimated from the corrected Lorentz first peak of WXRD [92], in Figure 4-7, where $q = 0.046\ A^{-1}$ and $L_p = \frac{2\pi}{q} = 135$ Å. The lamellae

thickness is then the product of L_p and crystalline fraction (0.4065 from WAXS calculation), which is 55.5 Å.

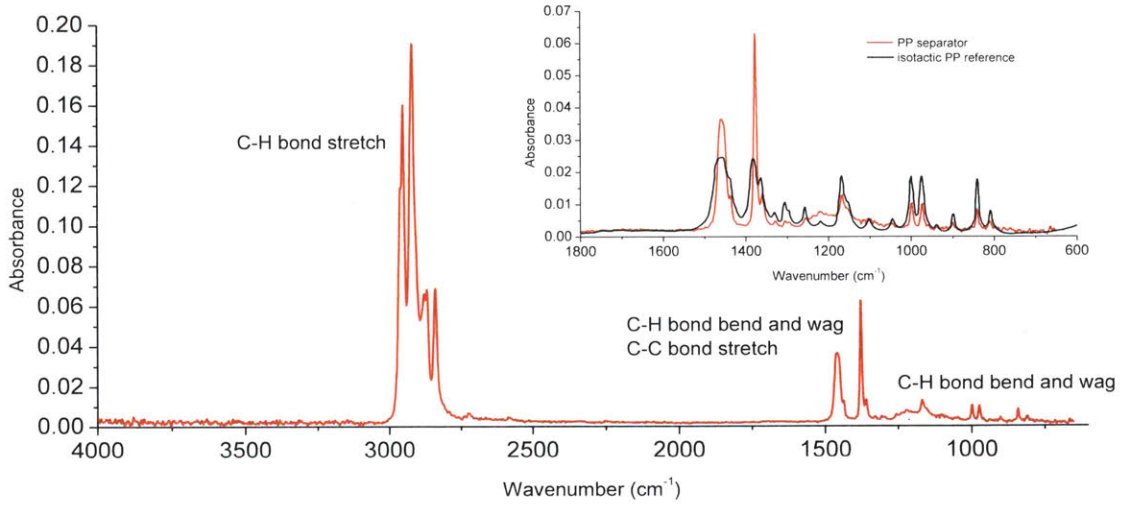
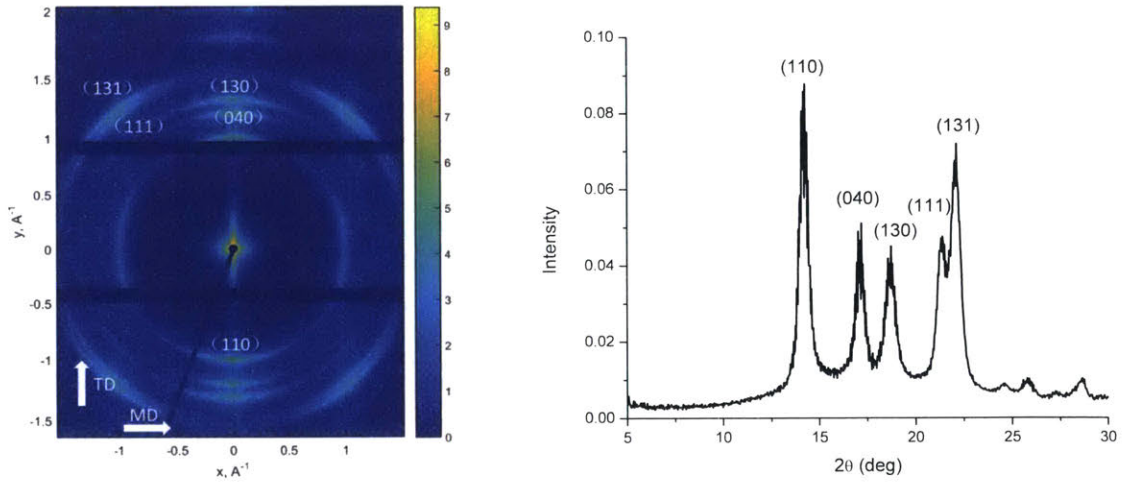
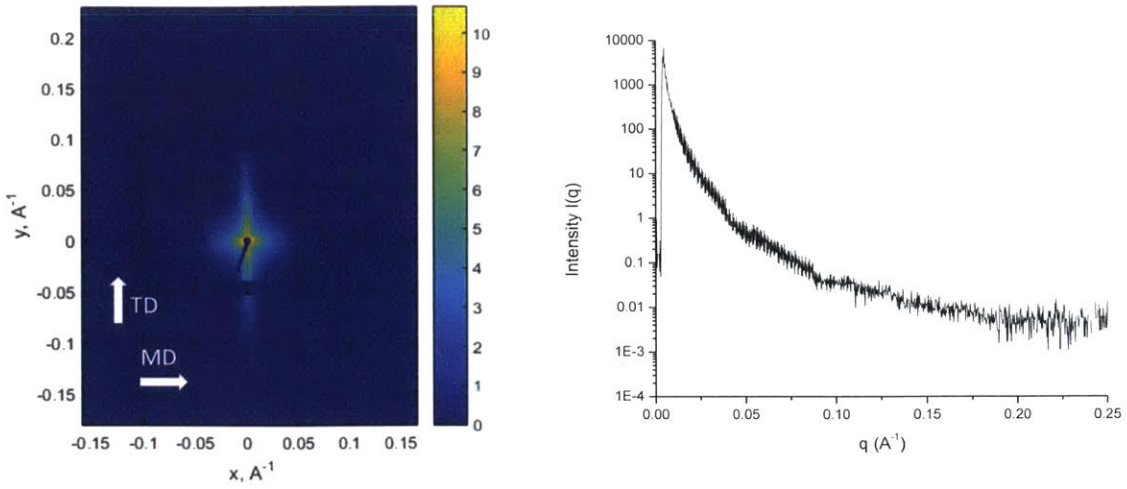


Figure 4-5 FTIR spectrum of PP separator, matched well with isotactic PP spectrum



(a)



(b)

Figure 4-6 Wide and small angle X-ray diffraction. (a) wide angle XRD; (b) small angle XRD

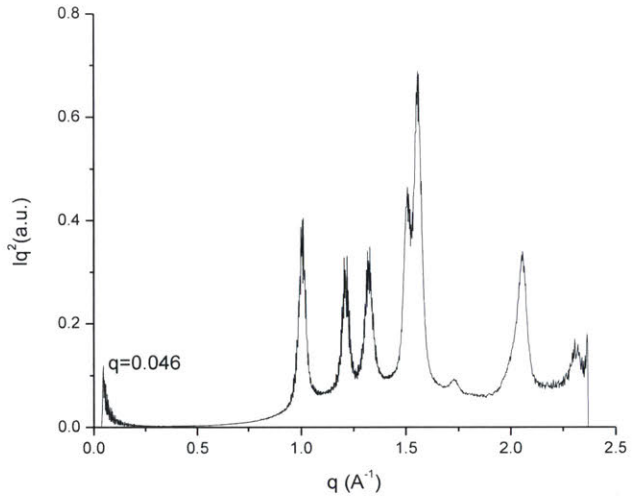


Figure 4-7 Lorentz corrected WAXS intensity profile

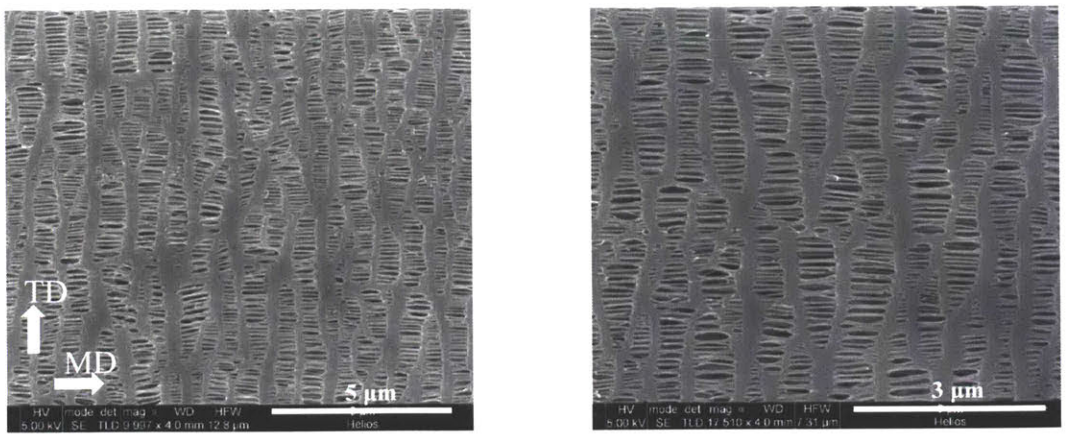
4.4 Micro fibril deformation sequence under uniaxial loading

To understand the deformation mechanism of the PP separator, SEM micrograph is a very good candidate. Figure 4-8 is the surface and cross section view of PP separator. Gold coating with thickness of 10 nm was deposited on the surface with EMS 150T sputter coater

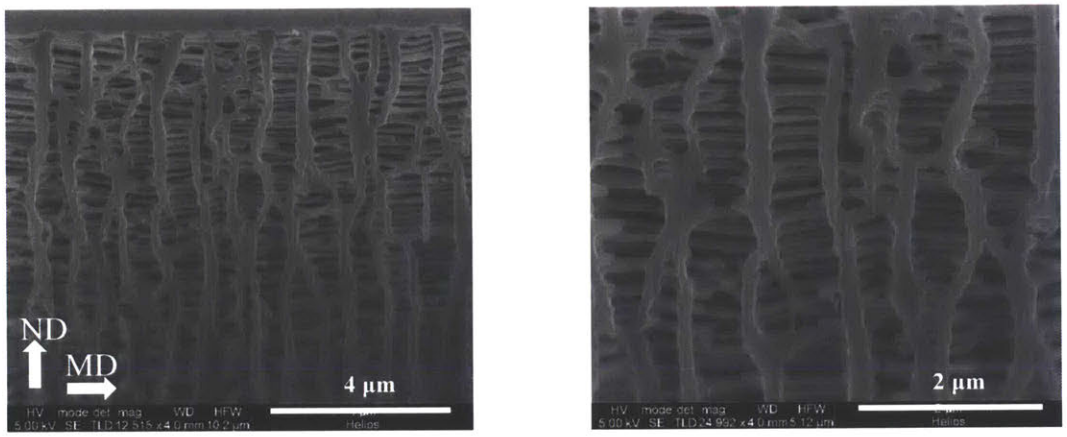
and Helios nanolab 600 Dual beam focus ion beam (FIB) milling SEM was used for cross section milling. As it will be mentioned in Chapter 5, FIB-SEM is a quite excellent tool to obtain undamaged the cross section surface. It clears shows the micro fibrils and anisotropic structure of the PP separator. Tabatabaer et al.[47] reported on a nice study of micro structure changes from nonporous extruded precursor film during stretching and they showed the fragmentation during stretching and indicated the formation of amorphous fibrils in between crystalline lamellae in the separator, as seen in Figure 4-8. Large increase of the elliptical pore size or the failure of lamellae during the loading of the separator may lead to transfer of electrons and internal shorts of the cell. Therefore, the study of evolution of the micro fibrils and lamellae under different loading could provide more detailed information of separator failure.



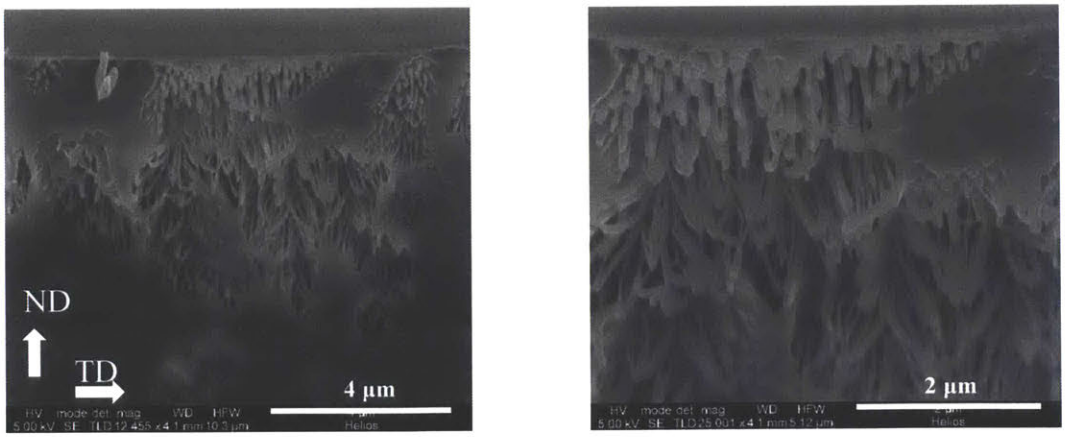
(a)



(b)



(c)



(d)

Figure 4-8 SEM micrograph of PP separator of surface and through thickness view. (a) 3D view of separator film; (b) surface SEM (different scale bar); (c) cross section view along MD (different scale bar, ND is normal direction); (d) cross section view along TD (different scale bar, ND is normal direction)

It was planned to conduct in-situ tensile tests of the PP separator under SEM. However, the fibrils are very thin in diameter and experience a severe beam damage during in-situ tension even with gold coating of 30 nm under beam voltage of 4kV, as shown in Figure 4-9 and in Ref [93]. There was not visible beam damage before the test while during tensile test, the original fibril became slender and new voids/fibrils were produced which were not covered by the gold coating and exposed to the beam. A way around this problem is to do interrupt tests.

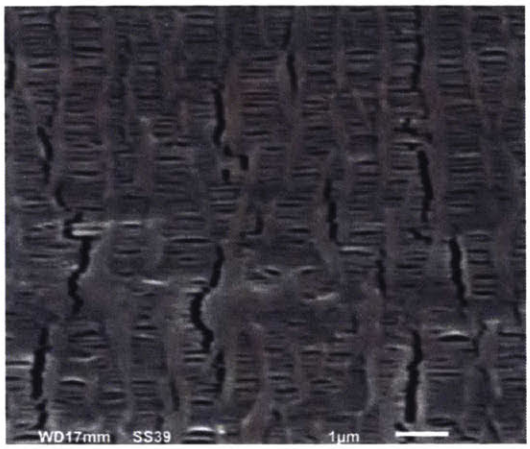


Figure 4-9 Fracture due to beam damage

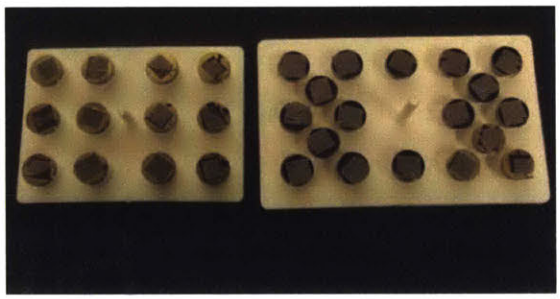


Figure 4-10 SEM samples from interrupt test specimens



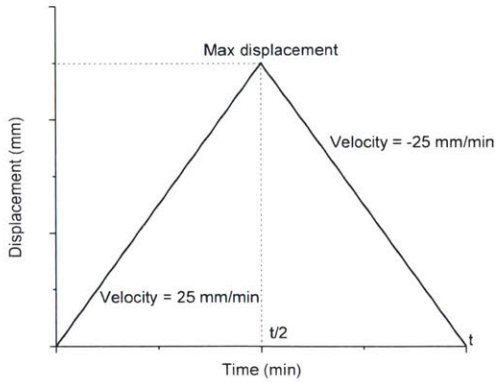


Figure 4-11 Interrupted test setup (250-N grip and 100-N load cell) and loading profile with loading and unloading speed 25 min/min

The interrupted test specimens were cut with width of 10 mm and length of 60 mm. The specimens were loaded to different strain levels and then fully unloaded to zero

displacement. The SEM samples in Figure 4-10 were cut from the most deformed regions of these tested specimens. The test setup is shown in Figure 4-11 (left) and the loading displacement-time profile is in Figure 4-11 (right). The loading and unloading speeds were fixed to 25 mm/min for these tests. The engineering stress-strain curves of the interrupted tests along MD are in Figure 4-12. Figure 4-13 shows the SEM morphology of the interrupted test along MD. The crystalline lamellae and fibrils are both elongated when the displacement is small. The fibril has limited extension range and the lamellae is expected to deform and new fibrils are formed then. Literature contributed this phenomenon to chain slippage of inter-lamellae as well as intro-lamellae [47,94–97]. Figure 4-14 shows the wide and small angle XRD of interrupted tests. The crystalline orientation (the crystal planes are same as in Figure 4-6) had not changed. Only the fractured specimen in Figure 4-14e indicates relative pore size decrease in TD direction.

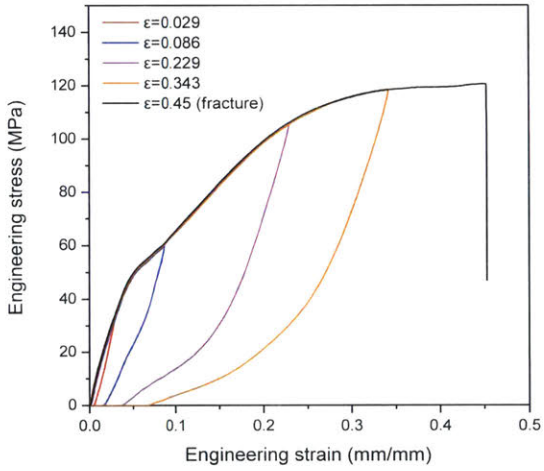
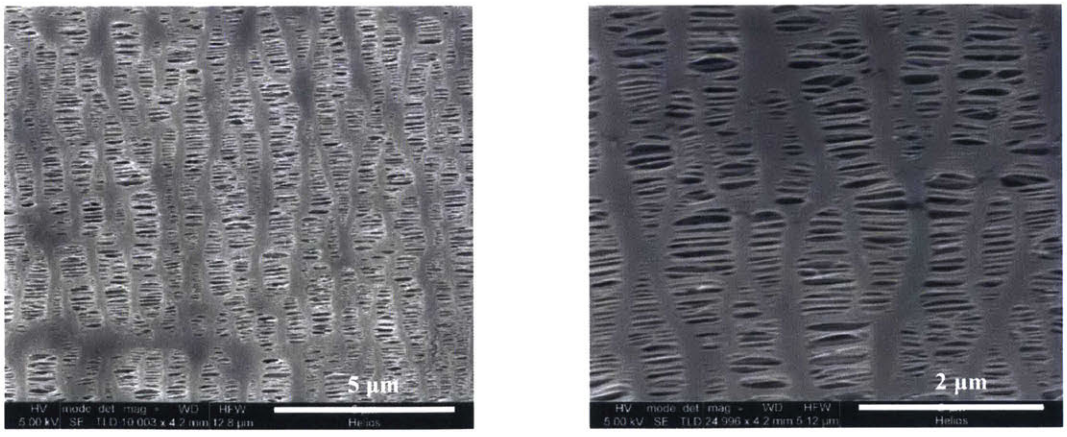
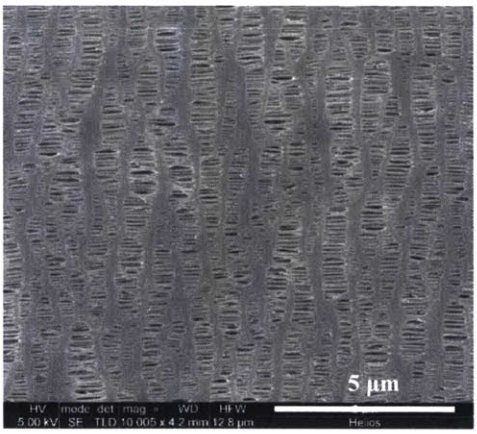
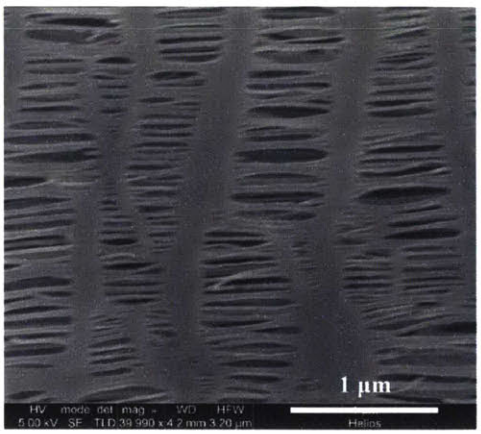


Figure 4-12 Force-displacement curves of interrupted test along MD

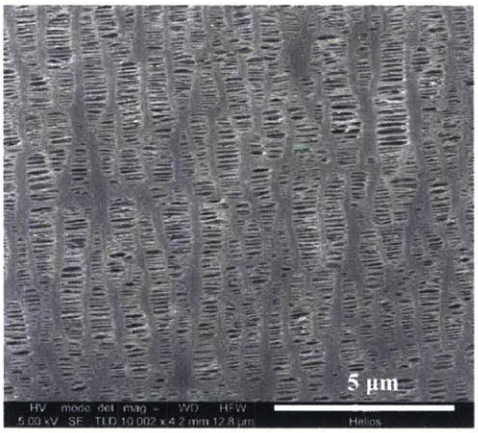


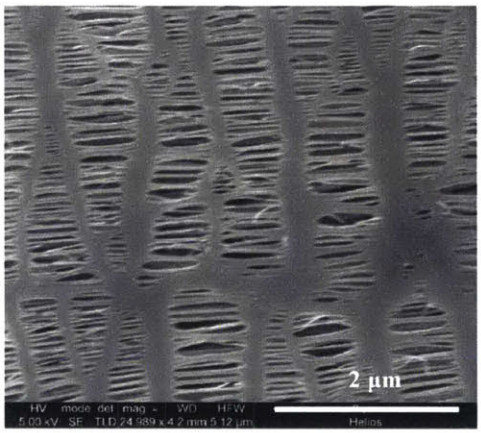
(a)



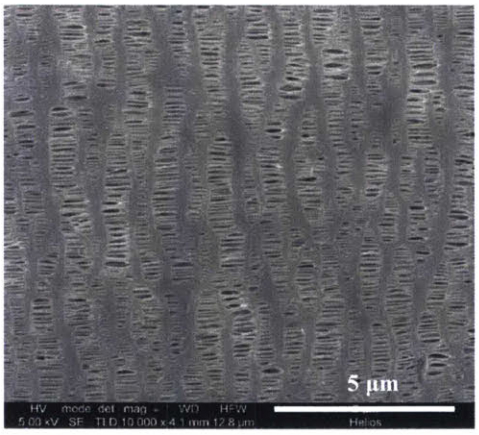


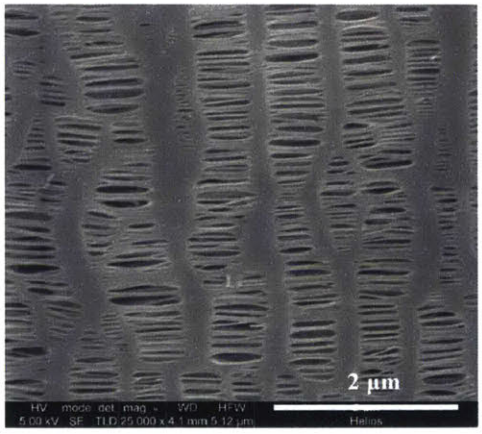
(b)



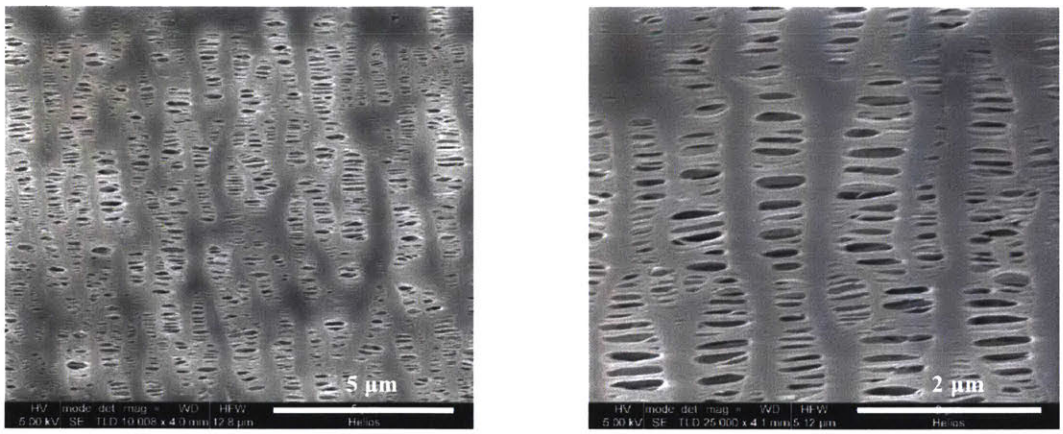


(c)



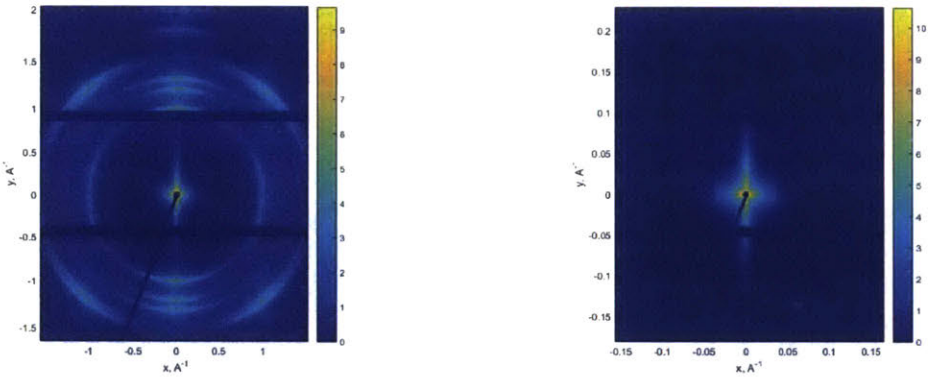


(d)

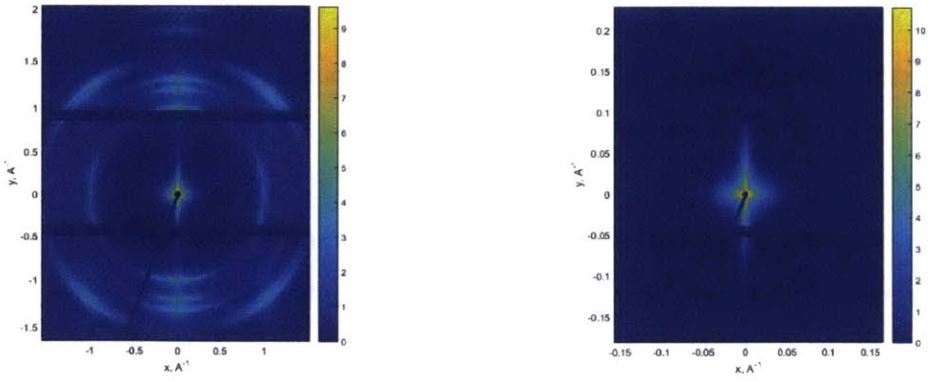


(e)

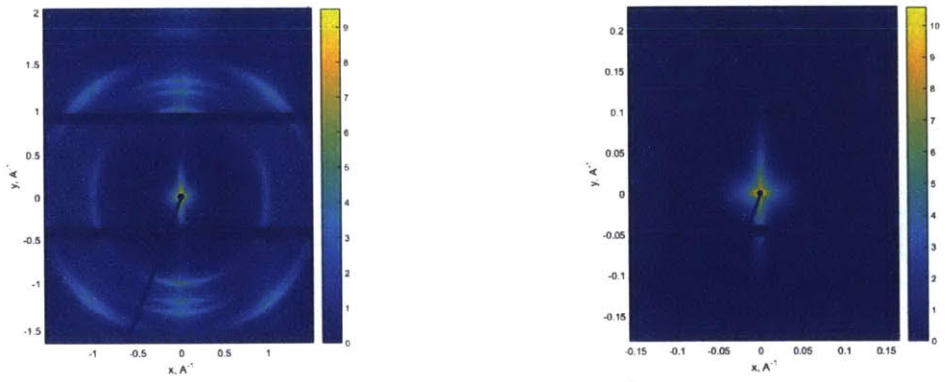
Figure 4-13 SEM micrograph of interrupted tests along MD with different maximum strains and scale bars. (a) engineering strain = 2.9%; (b) engineering strain = 8.6%; (c) engineering strain = 22.9%; (d) engineering strain = 34.3%; (e) engineering strain = 45% (fractured)



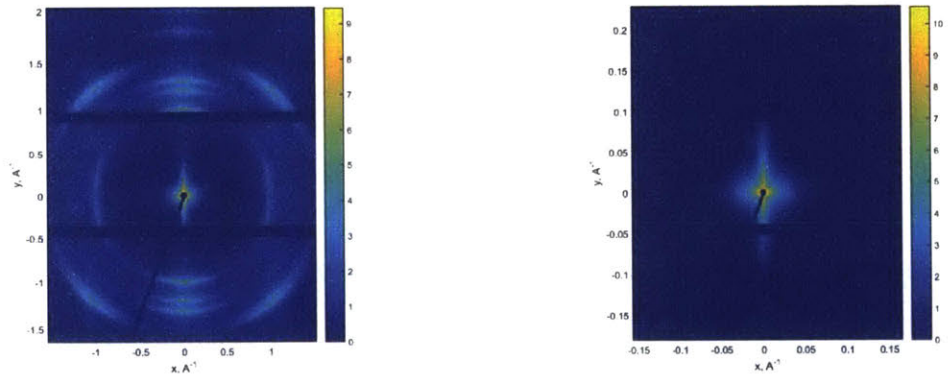
(a)



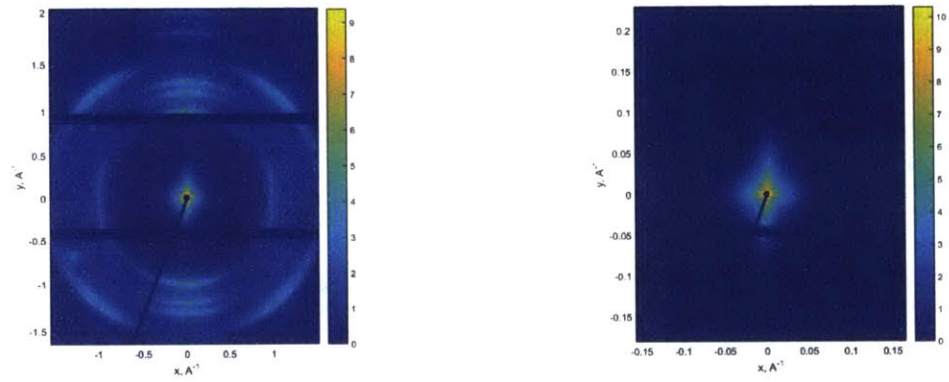
(b)



(c)



(d)



(e)

Figure 4-14 Wide and small X-ray scattering of interrupted tests along MD with different maximum strains and scale bars. (a) engineering strain = 2.9%; (b) engineering strain = 8.6%; (c) engineering strain = 22.9%; (d) engineering strain = 34.3%; (e) engineering strain = 45% (fractured)

The tensile tests along TD is shown in Figure 4-15. The minor axis of elliptical holes relatively increased during the deformation along TD, as shown in Figure 4-16. There was width decrease of the lamellae, such as Figure 4-16e-f. When the engineering stress went to 62.8%, the most deformed region became almost transparent and the SEM micrograph in Figure 4-16g gives a very interesting result. The lamellae blocks were well deformed and became thin while the fibrils are not parallel to MD anymore and tilted due the lamellae thinning. This indicates that the deformation of micro structures along TD are largely contributed by lamellae thinning. The pore size along TD became comparable to that along MD, as seen in small angle XRD picture of Figure 4-17. However, the crystal orientations did not change, which is the same as in MD tension.

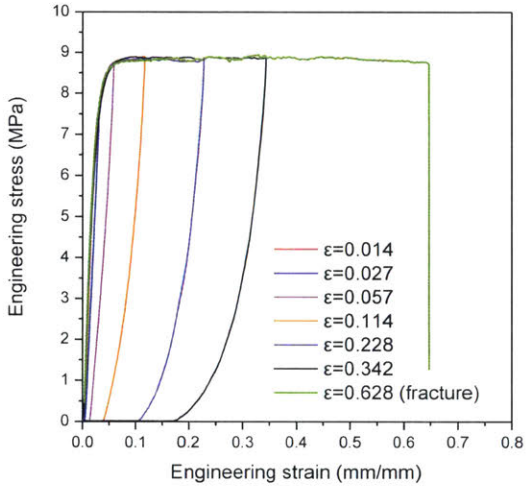
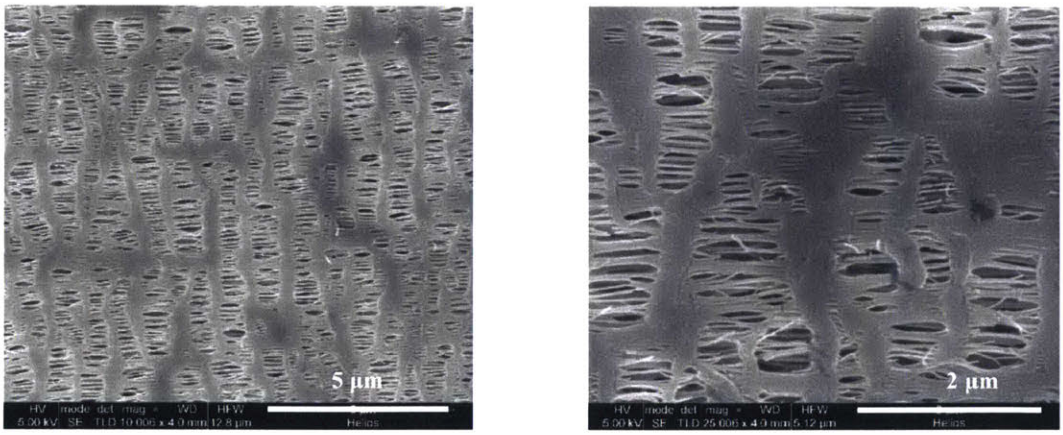
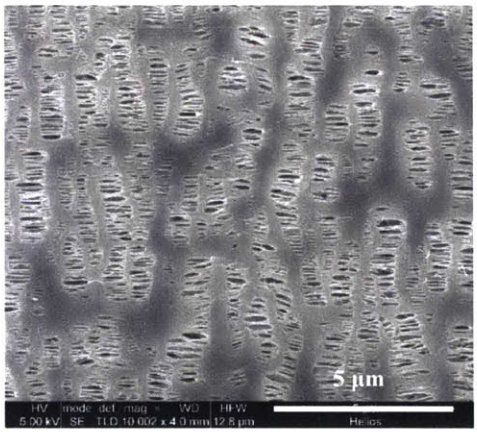
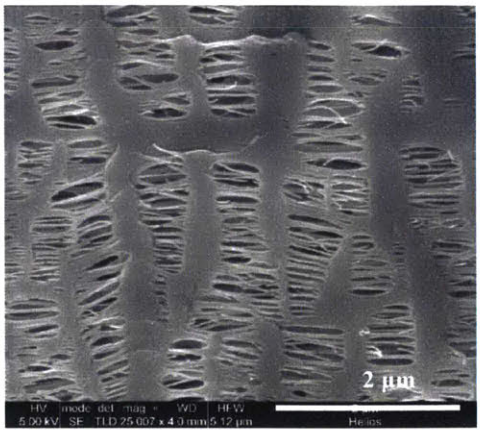


Figure 4-15 Force-displacement curves of interrupted test along TD

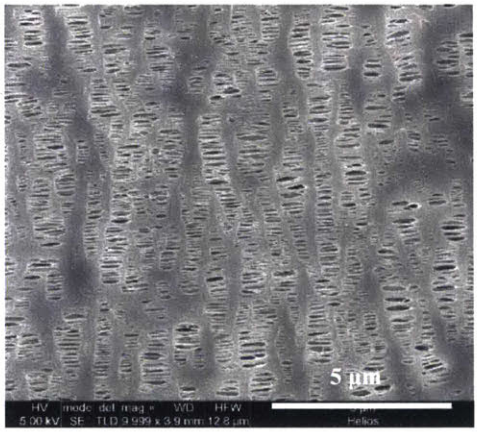


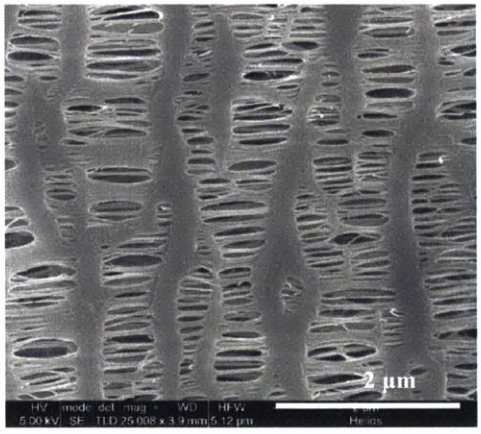
(a)



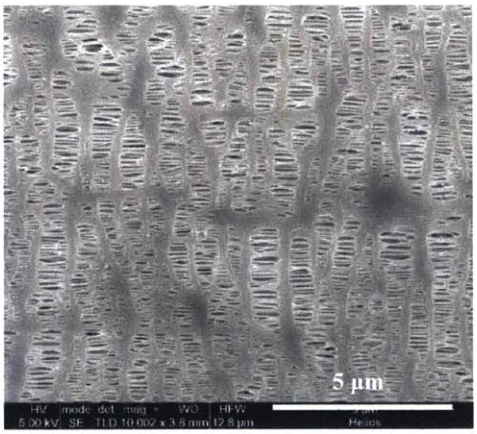


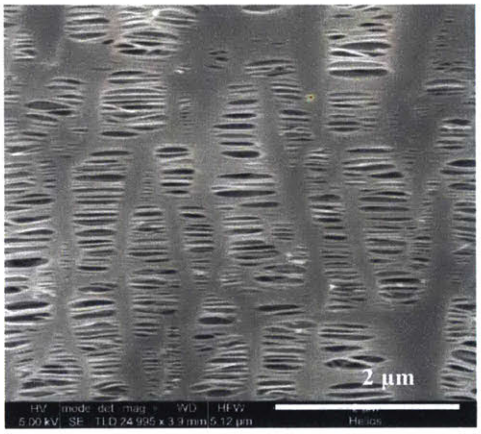
(b)



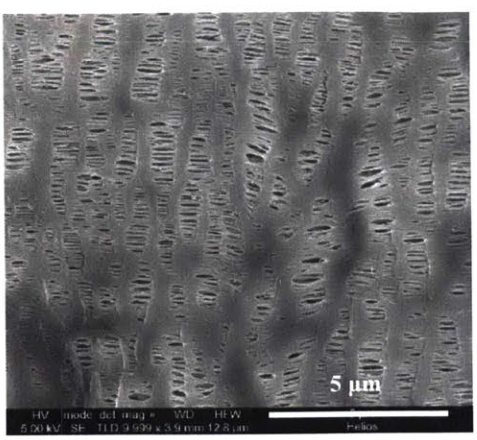


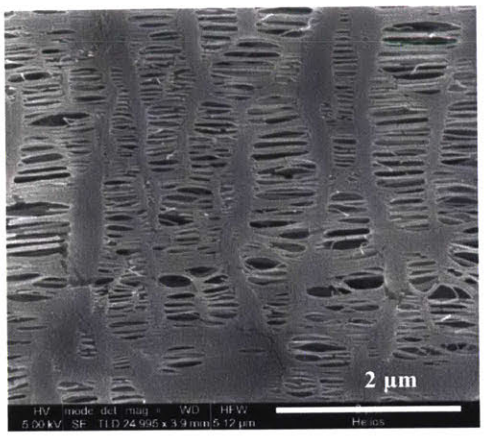
(c)



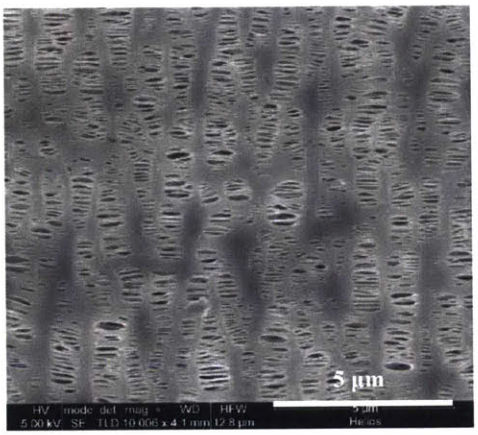


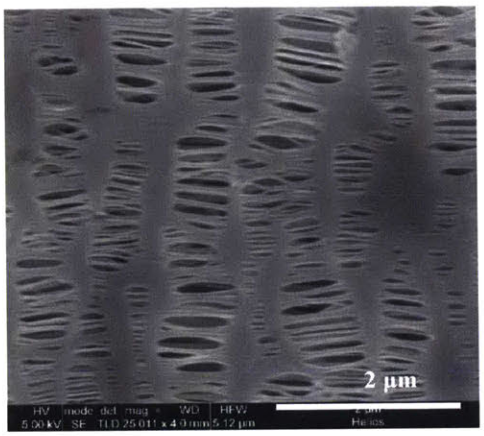
(d)



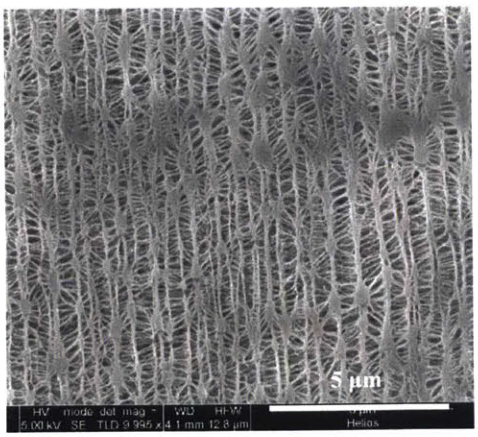


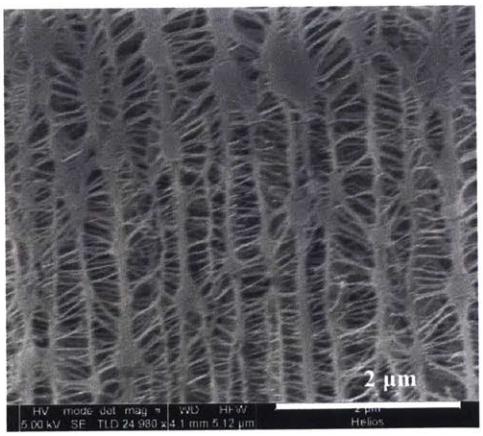
(e)





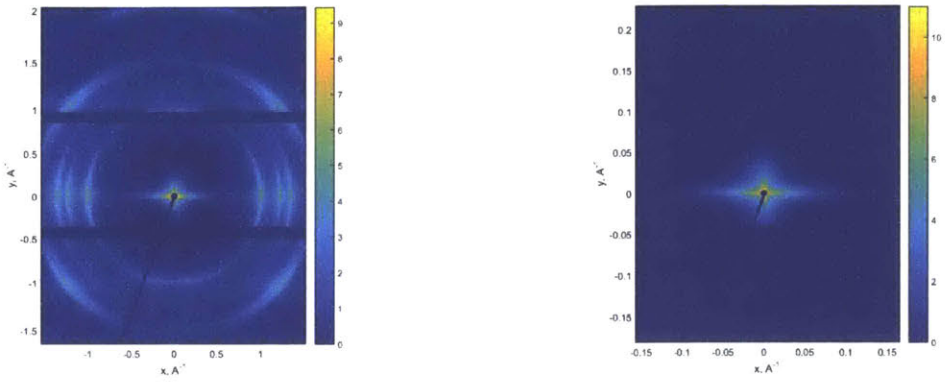
(f)



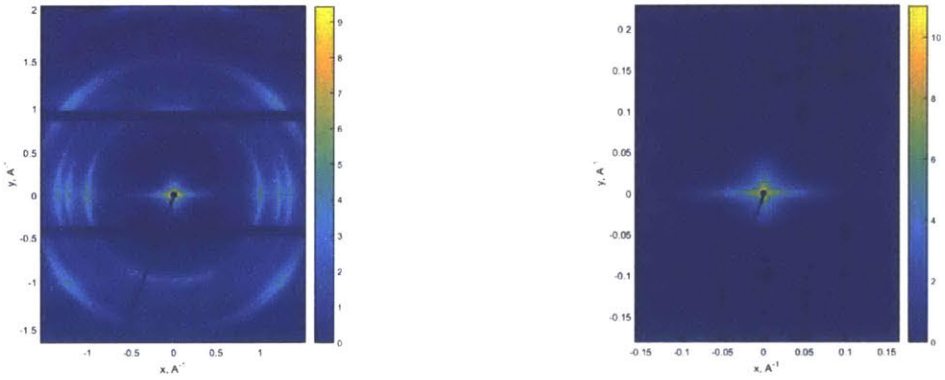


(g)

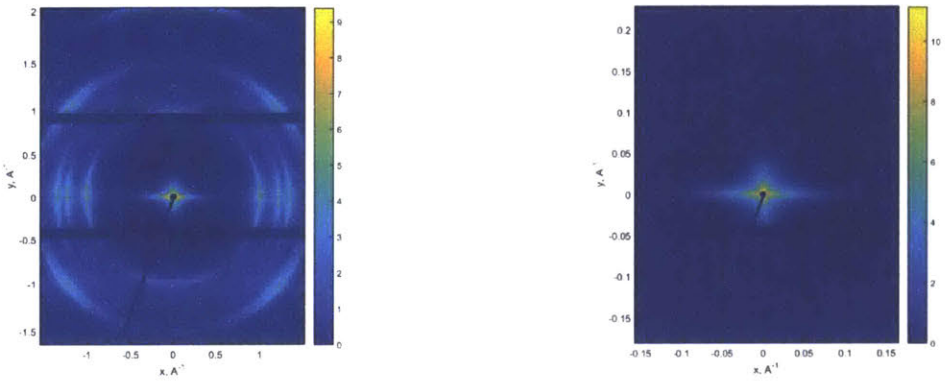
Figure 4-16 SEM micrograph of interrupted tests along TD with different maximum strains and scale bars. (a) engineering strain = 1.4%; (b) engineering strain = 2.7%; (c) engineering strain = 5.7%; (d) engineering strain = 11.4%; (e) engineering strain = 22.8%; (f) engineering strain = 34.2%; (g) engineering strain = 62.8% (fractured)



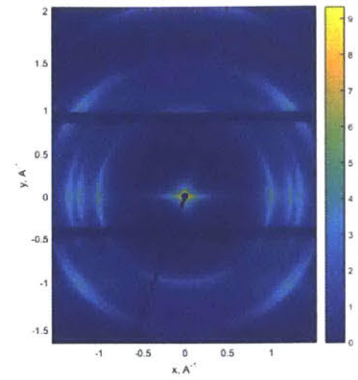
(a)

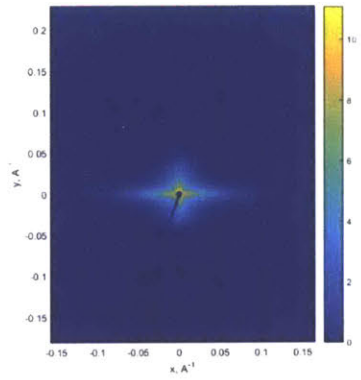


(b)

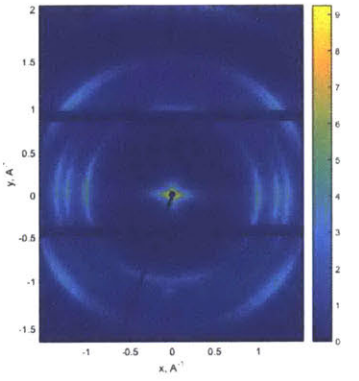


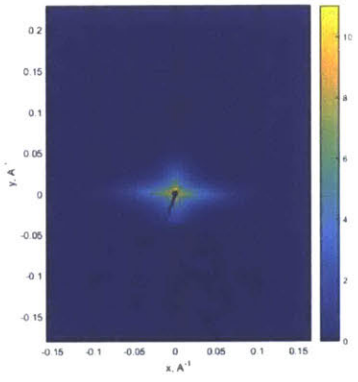
(c)



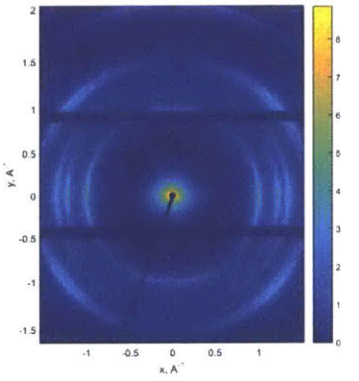


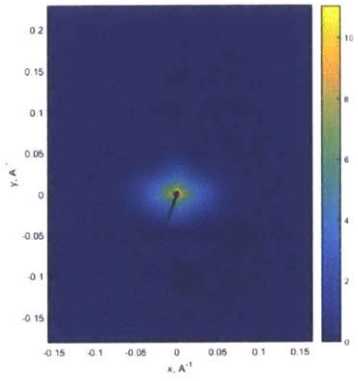
(d)



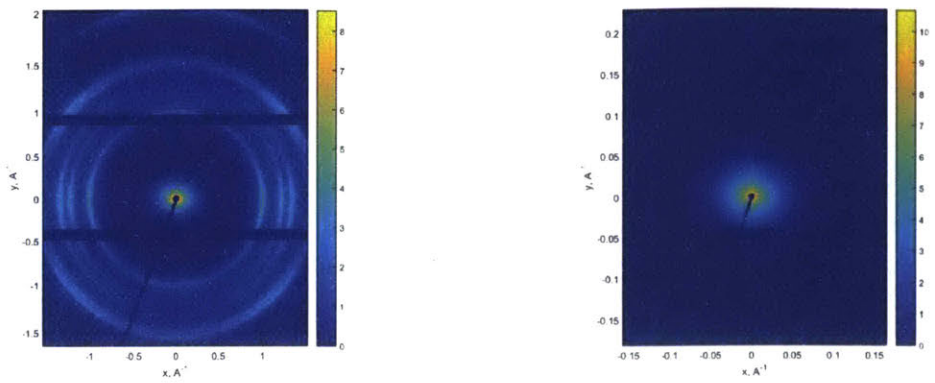


(e)





(f)



(g)

Figure 4-17 Wide and small X-ray scattering of interrupted tests along TD with different maximum strains and scale bars. (a) engineering strain = 1.4%; (b) engineering strain = 2.7%; (c) engineering strain = 5.7%; (d) engineering strain = 11.4%; (e) engineering strain = 22.8%; (f) engineering strain = 34.2%; (g) engineering strain = 62.8% (fractured)

The tensile test results along DD is in Figure 4-18 and Figure 4-19. Significant rotation in the DD loading was found when engineering strain went to 22.8%. Relative separation of lamellae block is in Figure 4-19e-f. Figure 4-21 is region of localization during DD tension: the shear deformation is very severe locally and failure of the fibrils were seen on the whole surface in certain specimens under large displacement. The XRD images in Figure 4-20 have strong evidence of crystal orientation during DD loading. The angle between major and minor axis of original elliptical pores changed from perpendicular to acute one.

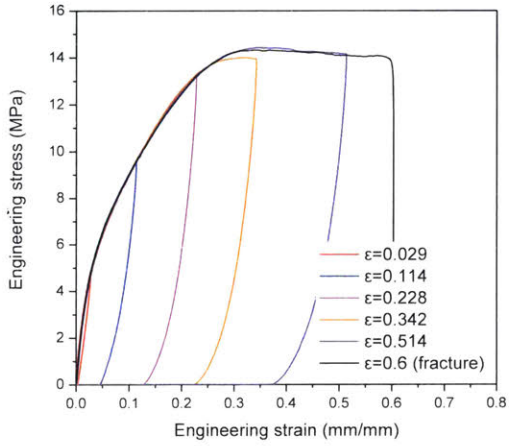
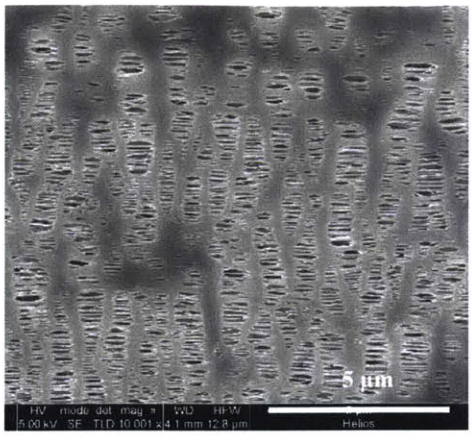
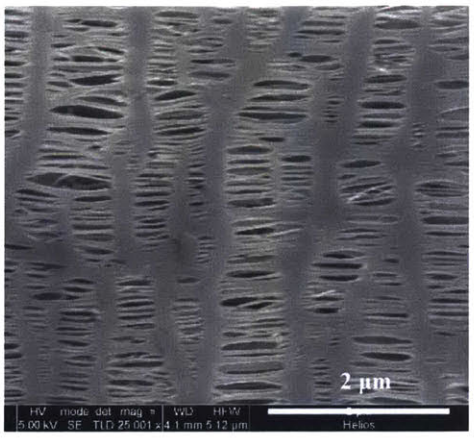
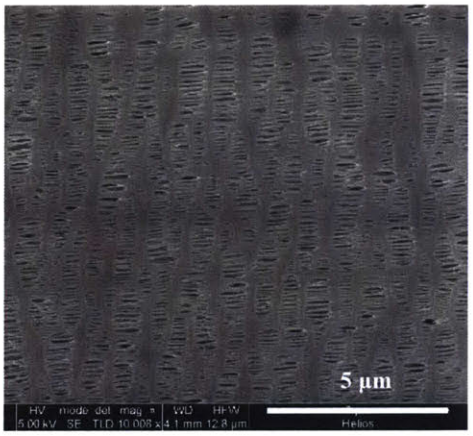


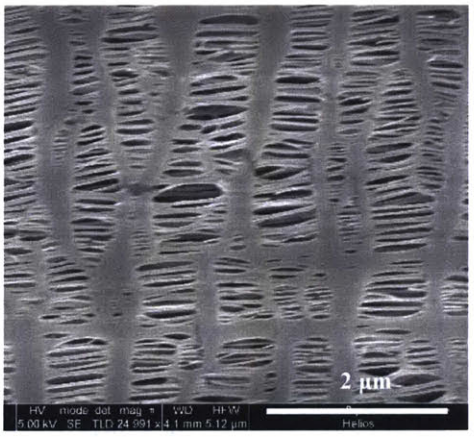
Figure 4-18 Force-displacement curve of interrupted test along DD



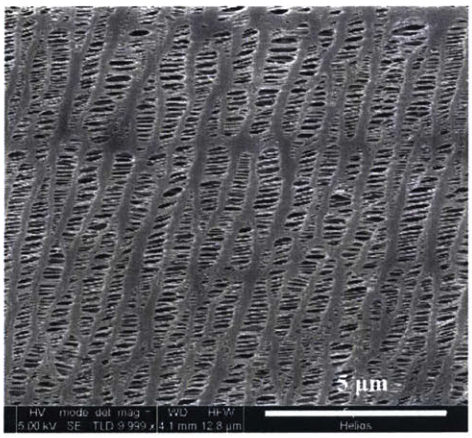


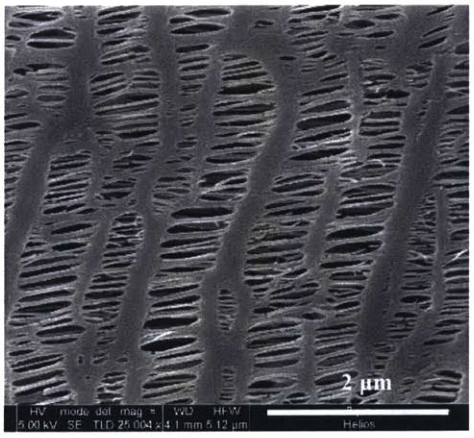
(a)



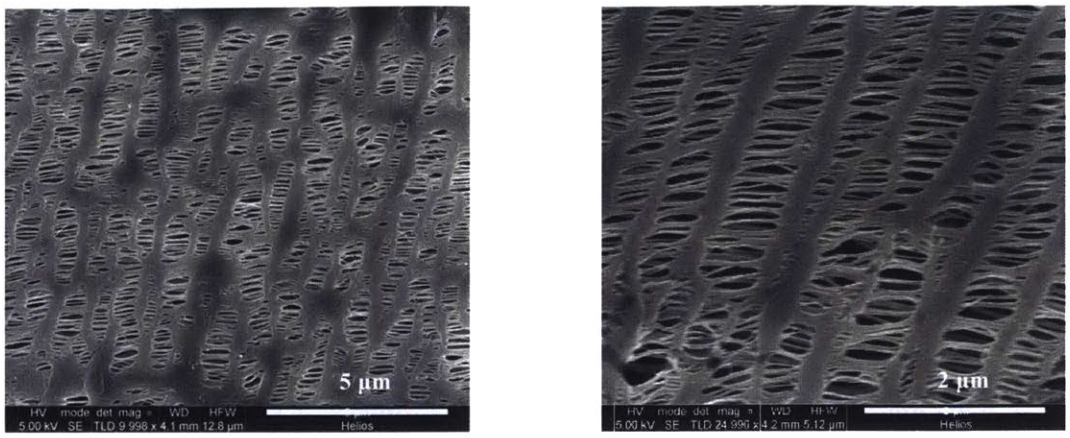


(b)

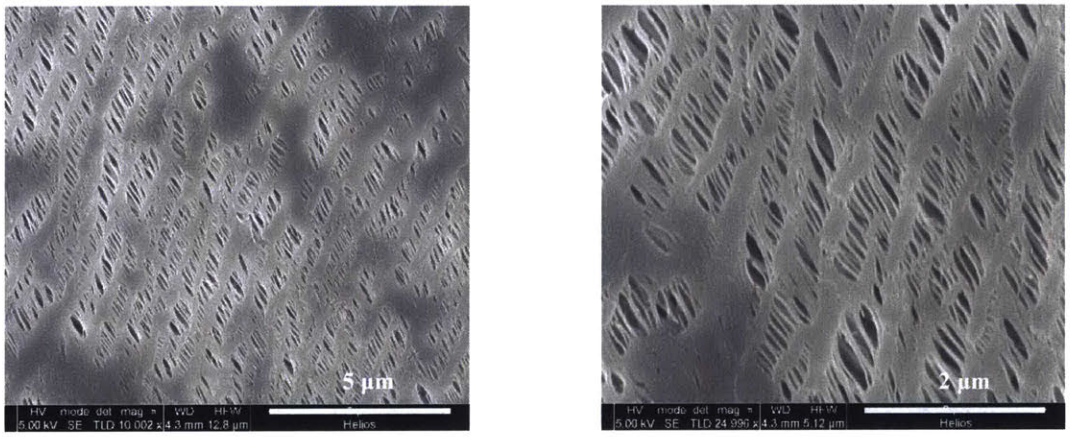




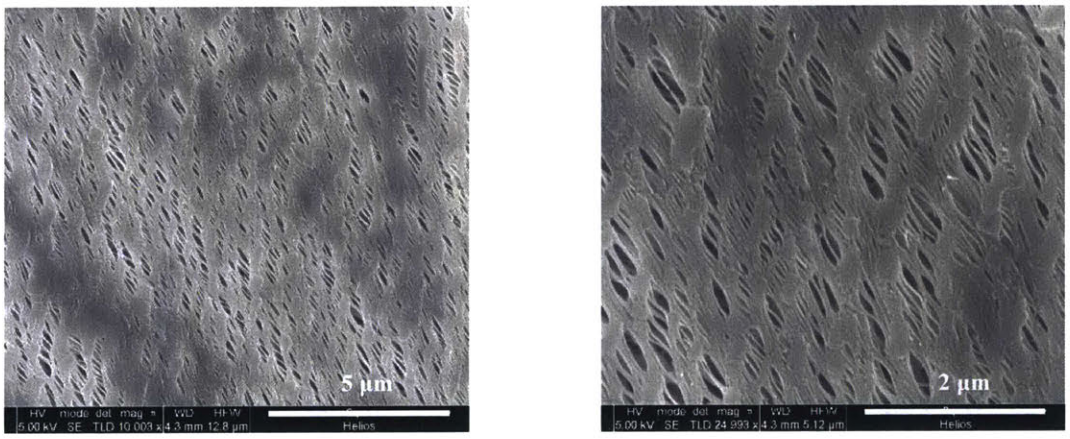
(c)



(d)

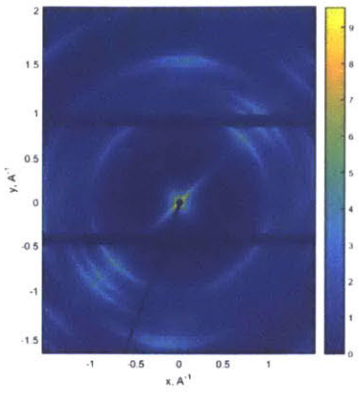


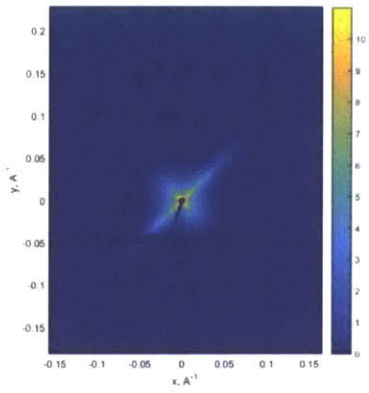
(e)



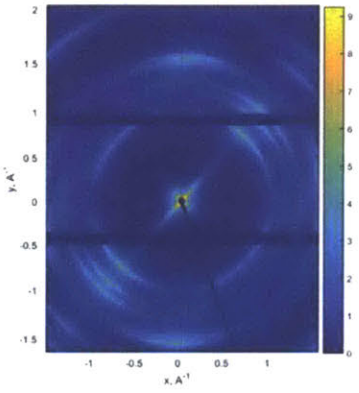
(f)

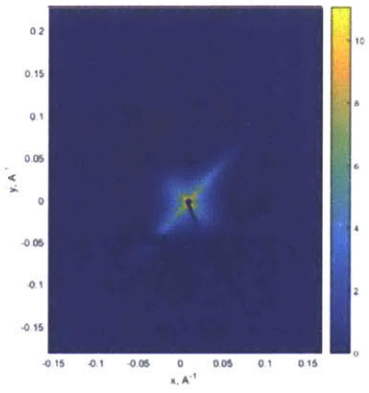
Figure 4-19 SEM micrograph of interrupted tests along TD with different maximum strains and scale bars. (a) engineering strain = 2.9%; (b) engineering strain = 11.4%; (c) engineering strain = 22.8%; (d) engineering strain = 34.2%; (e) engineering strain = 51.4%; (f) engineering strain = 60% (fractured)



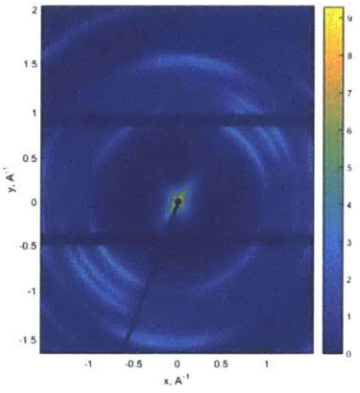


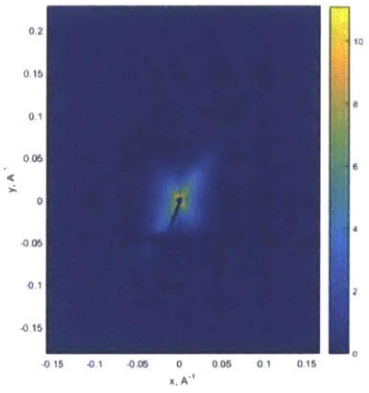
(a)



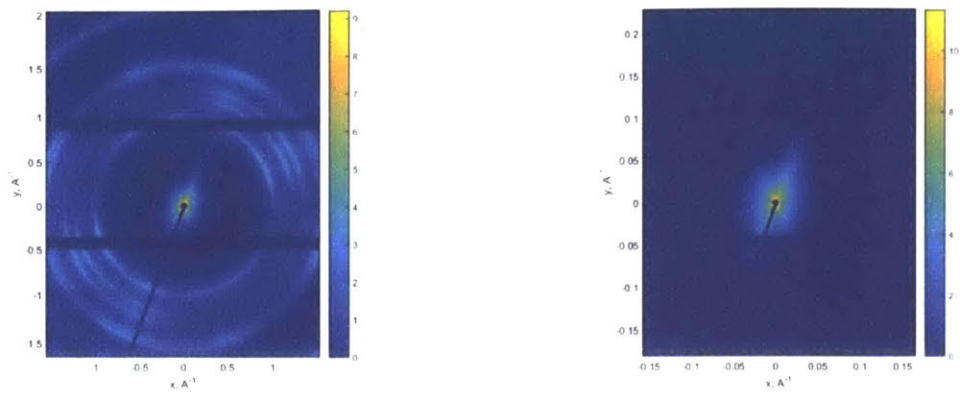


(b)

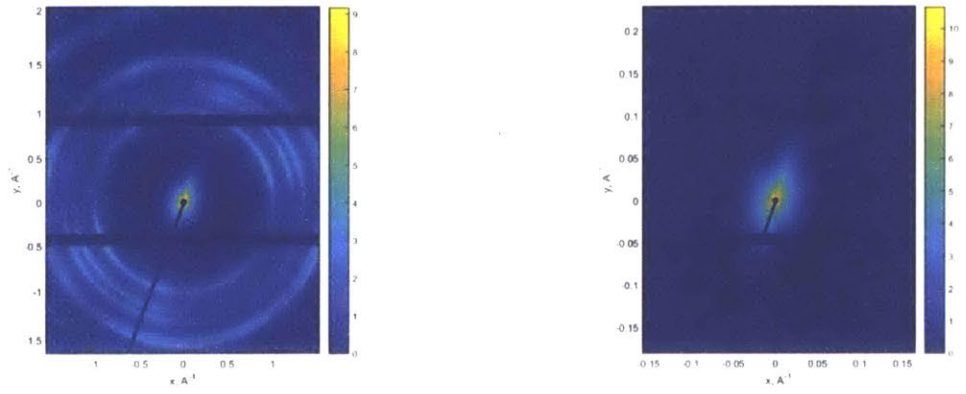




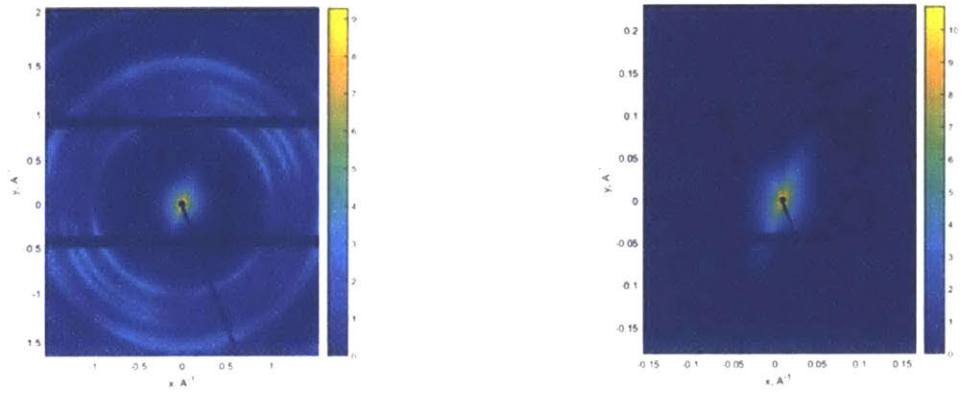
(c)



(d)

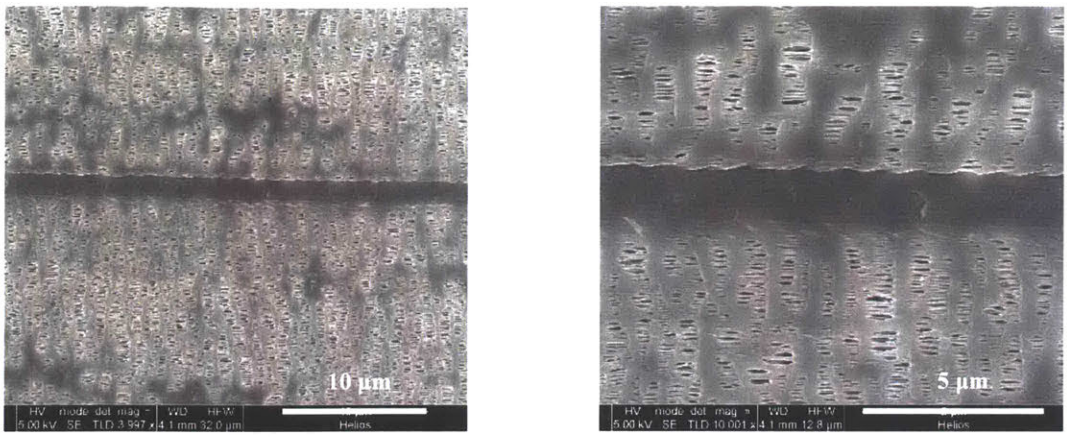


(e)

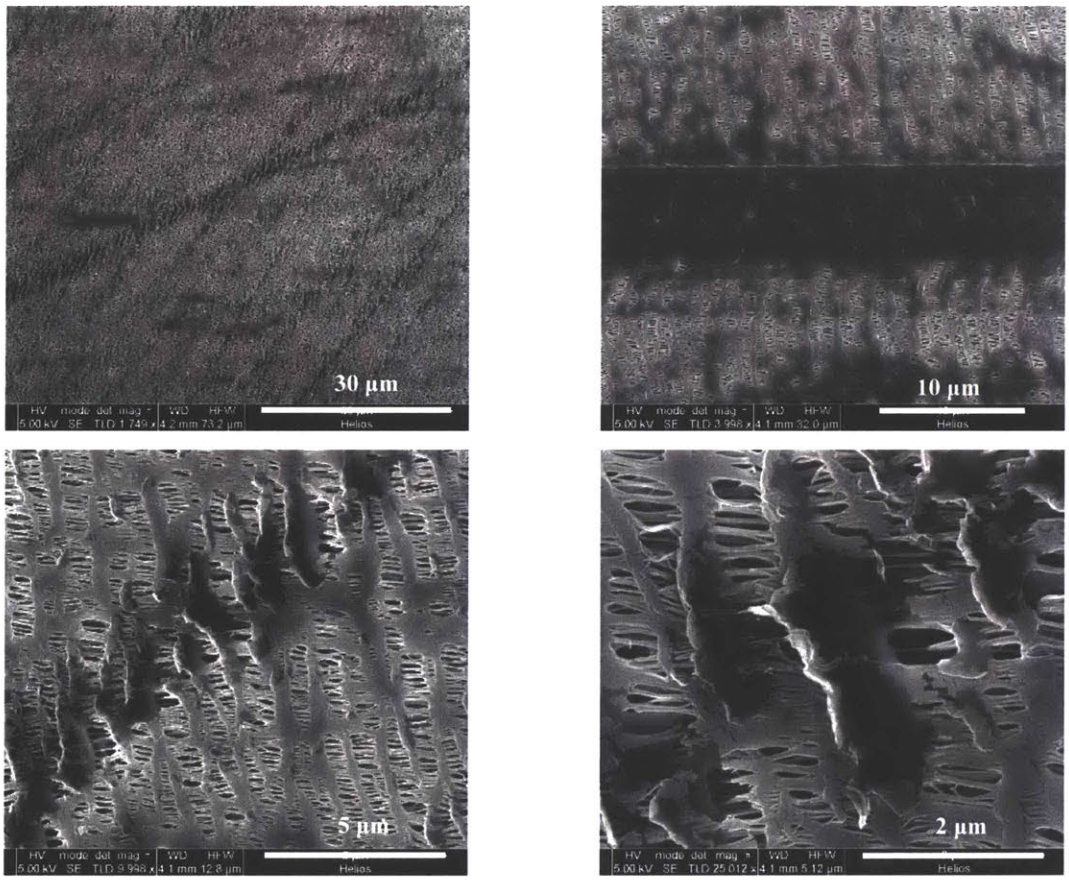


(f)

Figure 4-20 Wide and small X-ray scattering of interrupted tests along TD with different maximum strains and scale bars. (a) engineering strain = 2.9%; (b) engineering strain = 11.4%; (c) engineering strain = 22.8%; (d) engineering strain = 34.2%; (e) engineering strain = 51.4%; (f) engineering strain = 60% (fractured)



(a)



(b)

Figure 4-21 Localization of microstructures in DD tensile. (a) engineering strain = 2.9%; (b) engineering strain = 34.2%;

From the above SEM and XRD observation of the specimens from interrupted tests along MD, TD and DD, deformation sequences are summarized in Figure 4-22. The original microstructures of PP separator can be assumed a parallel of lamellae and fibrils as

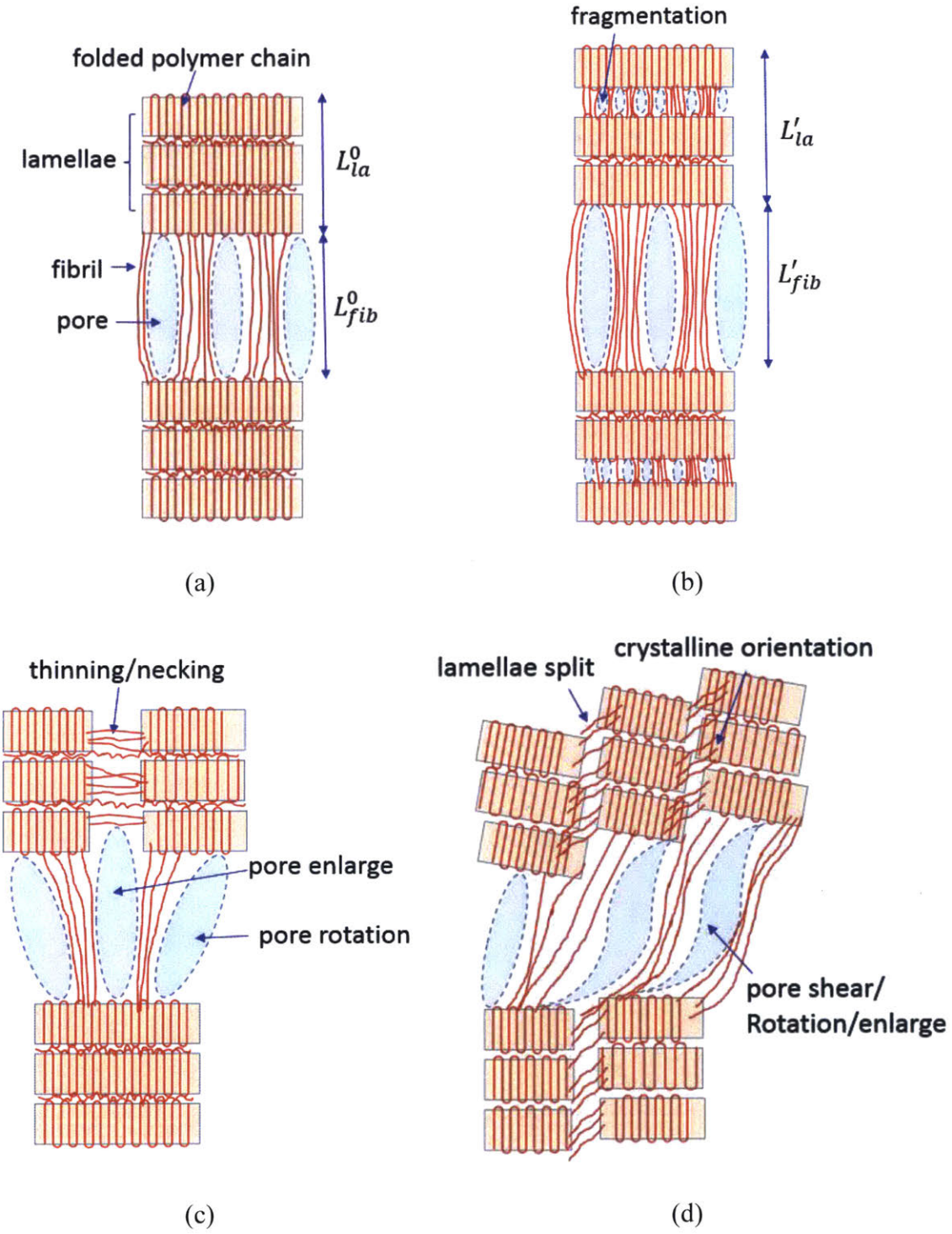
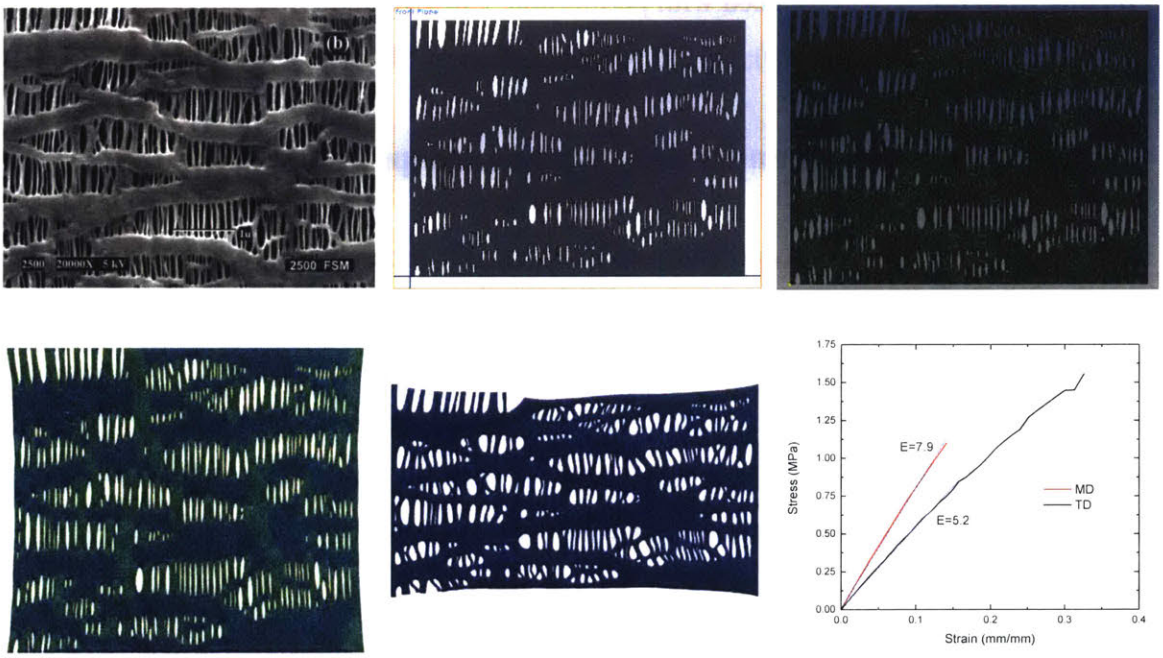


Figure 4-22 Illustration of the deformation sequences of fibrils and lamellae under MD, TD and DD loading. (a) original; (b) under MD loading; (c) under TD loading; (d) under DD loading

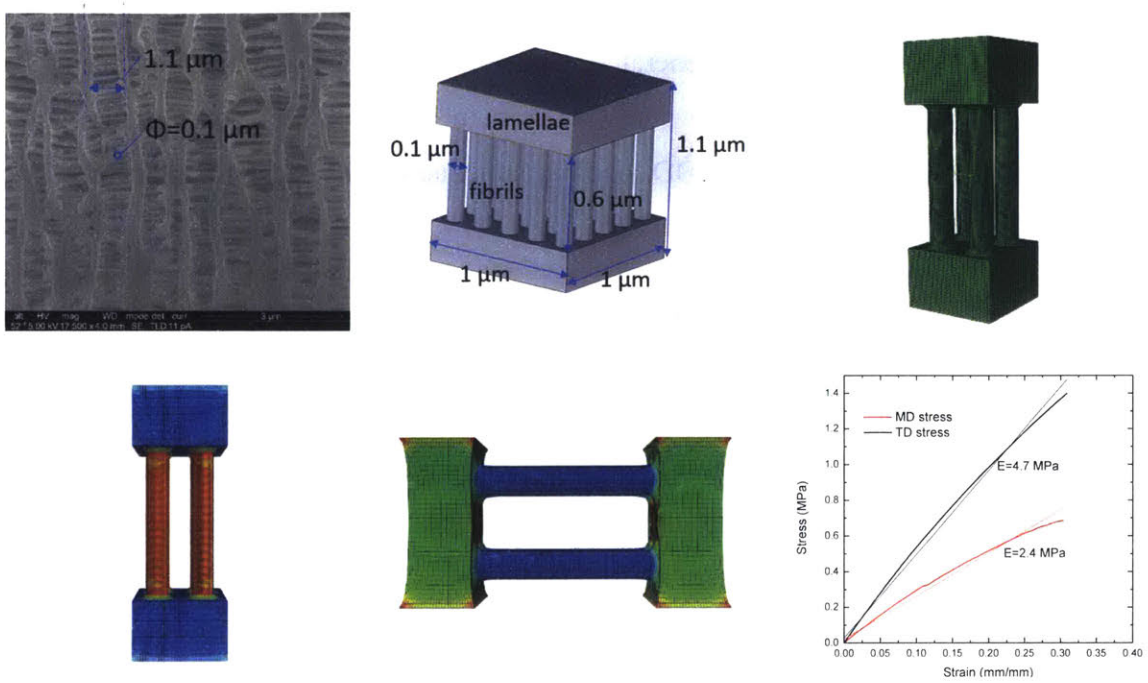
shown in figure 4-22a. Under MD tension, the lengths of both lamellae and fibrils increase. Fragmentation and new pores are generated. Under TD loading, there are thinning of the lamellae blocks and rotation of the pores, as seen in Figure 4-22c. Some of the pores become rounder and larger. Under DD loading, lamellae blocks separate and rotate. The pores are sheared as shown in Figure 4-22d.

4.5 Structural anisotropy vs. material anisotropy

The highly anisotropic properties are due to effects of the structural anisotropy and material anisotropy. The contribution of these two parts were studied based on sample numerical reconstruction of the structure by assuming same material properties all over. Figure 4-23 is 2D and 3D reconstruction of characteristic geometry of PP separator. With stress strain curve from bulk PP material used in Abaqus hyperplastic material model, the normal elastic stress strain comparison shows that the differences in MD and TD due to structural anisotropy are small, less than 2 times (strength level in MD over in TD), which suggested that the material anisotropy dominates the high anisotropic response along MD and TD.



(a)



(b)

Figure 4-23 Structural anisotropic study. (a) 2D reconstruction of PP separator (SEM picture from ref [39]. Reproduced with permission. Copyright © 2004, American Chemical Society); (b) 3D reconstruction of PP separator

4.6 Fibril deformation under out-of-plane compression

Due to a thin-film nature and operating environment, the separator must sustain a large out-of-plane compression load from electrodes during charge and discharge as well as abuse loading. The dimensions of PP separator before and after tests are shown in Figure 3-3b-c and the nominal stress-strain curves are presented in Figure 3-4. Under through thickness compression, the material in TD, which has lower strength got stretched while it shrunk in MD. The separators experienced obvious yield points under the applied compression. After the yield point, the stress was growing exponentially until almost full densification. An SEM image of this separator (Figure 4-24) shows that bulk material regions have been stretched along width and length, which in turned caused local buckling of fibrils. This explains the lengthening in TD and shrinking in MD seen in Figure 3-3c.

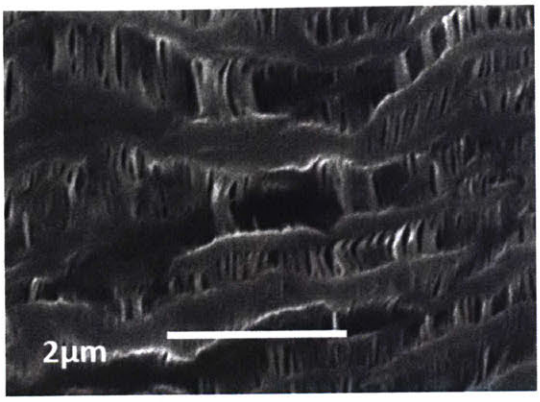


Figure 4-24 SEM micrograph after out-of-plane compression

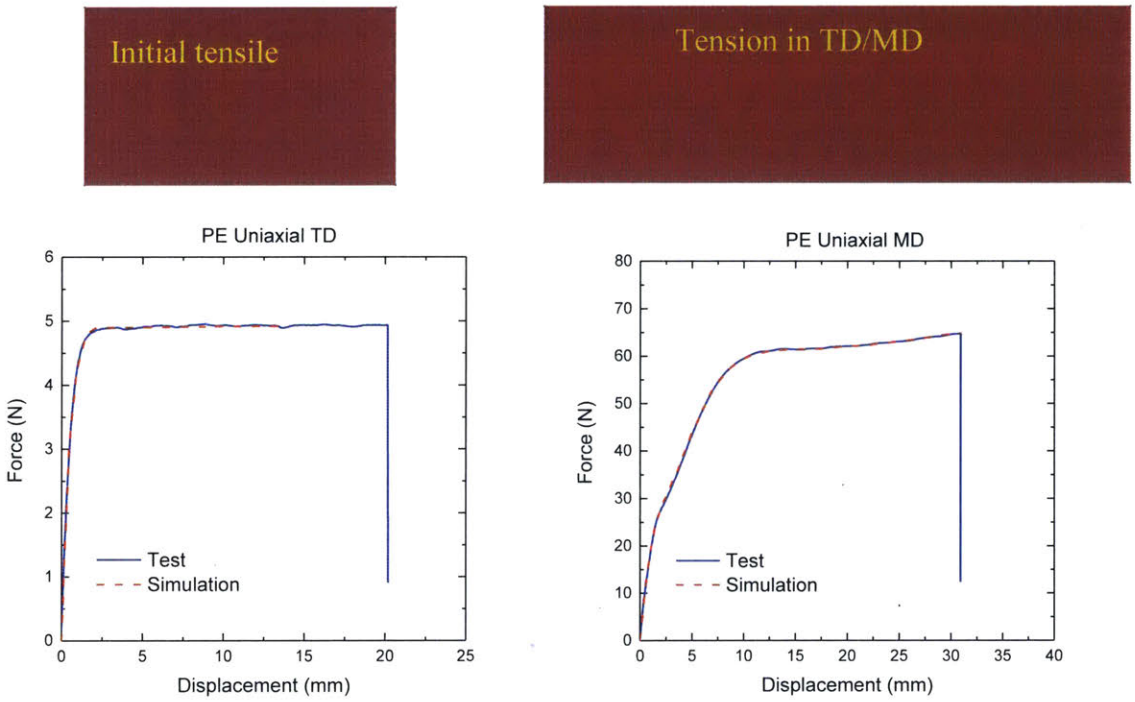
4.7 Finite Element Modeling of PP Separator

It transpires from the above tests that the PP separator has distinct properties in three directions of loading. Also, properties are different in tension and compression. Combining this information and the porous nature of micro structure of the separator, it was concluded that an anisotropic foam model may be a reasonable choice to provide a first order approximation for the behavior of separators in various loading scenarios. Therefore, the PP separator was modeled using material 126, the anisotropic crushable foam model, from library of LS Dyna materials. This material model allows input of different stress-strain curves in three principal directions of anisotropy, in tension, compression, and shear as well as different properties in tension and compression. Tensile properties in TD and MD were inputted to the model as show in Figure 3-1b. As it was not possible to measure the tensile properties in through-thickness direction for such a thin specimen (25 μm), those properties were assumed to be equal to TD. Compressive properties could only be measured in through-thickness direction (Figure 3-4) and were assumed to be similar in two other directions. The uniaxial tensile test in diagonal direction was used to calculate shear stress/strain in principal anisotropy plane by 45 degree rotation of stress and strain tensors (45 degree from axis of diagonal specimen), and it was assumed to be equal for all three shear directions.

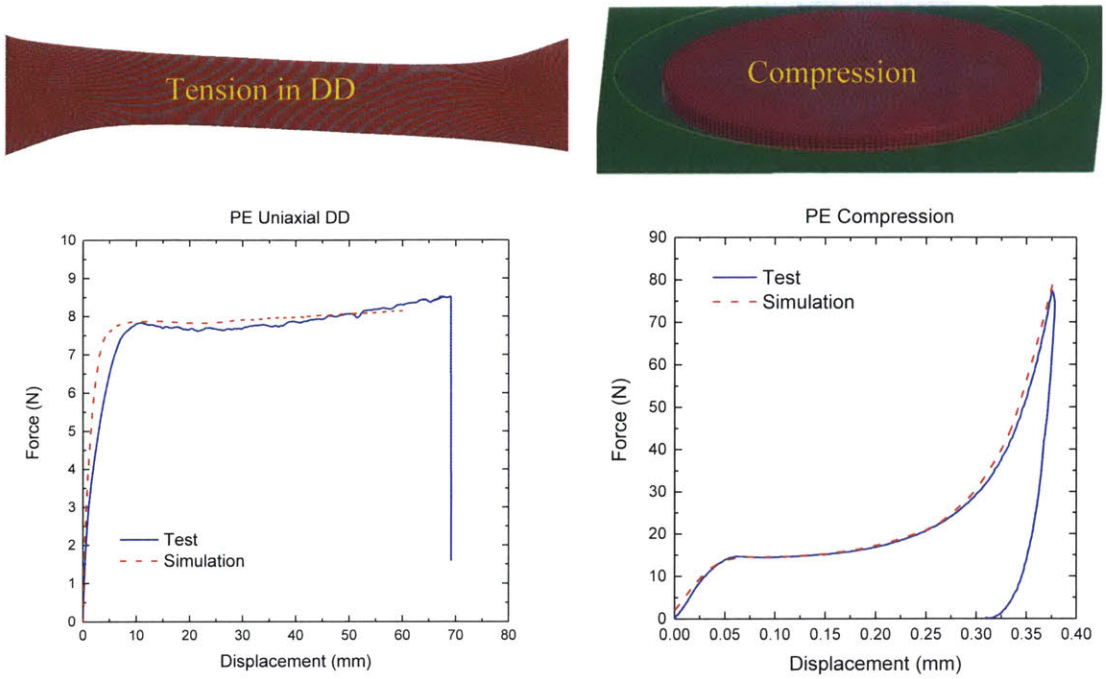
Finite element (FE) mesh for uniaxial tensile specimen was developed using solid elements of 0.25x0.25x0.025 mm. The model had nodes fixed on one end and moving with a

constant rate on the other end. During loads in TD and MD direction, no significant change in cross section of the sample was observed (see Figure 4-25a). However, in DD direction the central part of the mesh rotated during loading (see Figure 4-25b), which was similar to the deformation of DD specimen during the test, as seen in Figure 3-2b. In all uniaxial loading cases in tension and compression, the model represented very closely the load-displacement behavior seen in the tests (Figure 4-25a-b, and c).

In the next step the biaxial tensile loads with different punch heads were simulated. A failure criteria of maximum principal strain was used in these simulations. As it could be observed in the uniaxial tests, failure strain varied for the three directions of loading. Figure 3-1b showed that the smallest failure strain was observed in TD which was about 0.57. This value was used for all simulations of punch loadings.



(a)



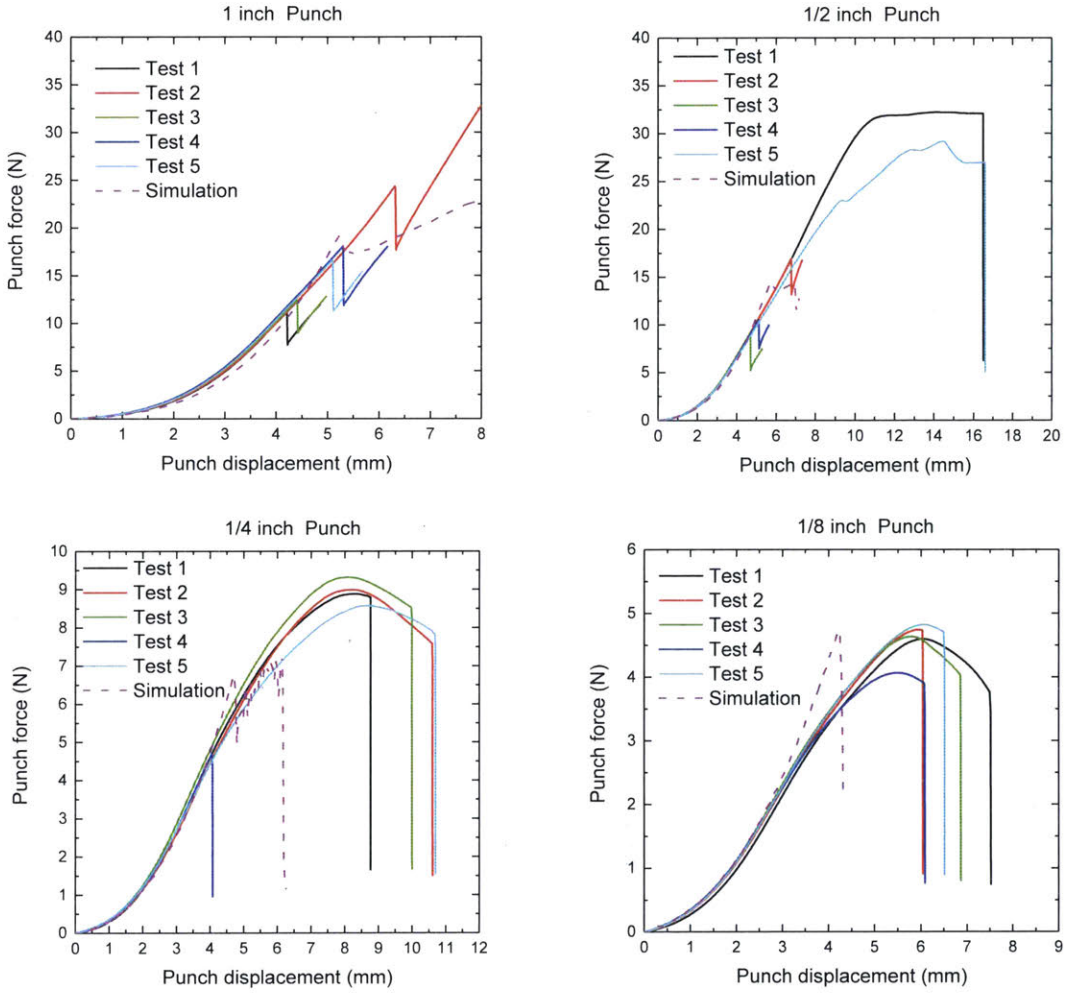
(b) (c)

Figure 4-25 Simulation of uniaxial tensile and compressive loading of separators. (a) tensile loading in TD and MD; (b) tensile loading in DD; (c) through-thickness compression

FE mesh for this simulation was divided into two areas, in the center of the specimen a finer mesh of 0.125x0.125x0.025 mm was used, while on the perimeter a larger mesh of 0.25x0.25x0.025 mm was employed. Figure 4-26a shows punch simulations with 1 inch, 0.5 inch, 0.25 inch and 0.125 inch diameter punches. The models were successful in predicting load-displacement curves of the separator up to the point for all punch sizes (Figure 4-26b). For ¼ and ½ inch punches, onset of element deletion after peak force also corroborated with developed crack. For 1 inch punch simulation, failure and element deletion was much later than local peak and did not correspond to tearing observed in the tests. The model also correctly predicted the effect of anisotropic material on the shape and curvature of deformation in two planes of anisotropy. Figure 4-27 shows comparison of model and test during 1/8 inch punch loading in two planes. Due to anisotropic properties, the side views from vertical planes along MD and TD show different deformation slopes, as shown in Figure 4-26c (left). The FE model could capture this phenomenon.



(a)



(b)

Figure 4-26 Punch loading simulation and comparison with test: (a) punch test simulation with different punch size; (b) comparison between test and simulation with different punch heads

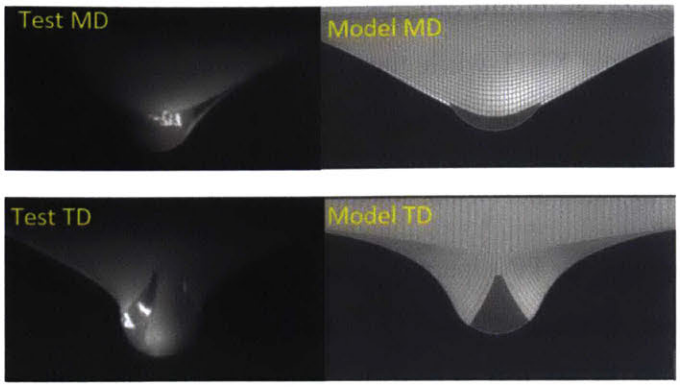


Figure 4-27 Side-view comparison between test and simulation from vertical planes along MD and TD

4.8 Summary

Dry-processed PP separator is commonly used in EV batteries. The temperature of cell components, especially the region where the cooling system is weak, could rise to a high level. The properties of the separator under high operating temperature is very important for later numerical modeling of mechanical abuse of operating cells. Uniaxial tensile tests of PP separator along MD, TD and DD under 23 °C, 30 °C, 40 °C, 50 °C, 60 °C were obtained with DMA. The strength decreases a lot from 23 °C to 60 °C. Through temperature sweep from 20 °C to 200 °C, significant decrease in storage modulus was observed. The strain rate sensitivity study of the separator shows the viscous properties. Wide angle and small angle X-ray scattering characterization gives the crystalline orientation information of the PP separator. There are several crystalline planes aligning along MD due to stretching of the nonporous precursor. Fourier transform infrared spectroscopy (FTIR) characterization shows that PP separator is made from isotactic PP.

SEM micrograph from interrupted test along MD, TD and DD gives the deformation of micro fibrils and crystalline lamellae. In MD tension, increase of lamellae width and the fragmentation in the crystalline lamellae was observed. The shortening in width of lamellae and rotation of fibrils were seen in TD loading. The separation/split of lamellae blocks and their rotation were found and localization in several regions and specimens indicates the two direction deformation during DD loading, such as MD shear and TD tension. No

distinguishable change of crystalline orientation was seen in MD and TD loading according to the wide and small angle XRD, while the elliptical pores are tending to become sphere-like shape in the end of the loading. Crystalline orientation change and pore orientation are observed in DD loading.

A finite element model of the PP separator was developed in LS DYNA by making use of LS DYNA's modified anisotropic foam model. The model succeeded to predict the load-displacement behavior in all test scenarios. Additionally, the anisotropic deformation during punch test and shear deformations in DD tensile test were simulated realistically. Further investigations are underway for development of a more refined material and failure models for all tested separators.

Chapter 5

Mechanical Degradation of Battery Separators Under Charge-Discharge Cycles

5.1 Introduction

The charge and discharge induced aging of lithium-ion batteries, mainly the capacity loss of the battery cells after years of operation, is still a big challenge for the fast-growing market of electric vehicles worldwide. Researchers are continuously studying the aging mechanism of cathodes and anodes, such as fracture of chemical coatings, formation of solid electrolyte interface, degradation of active materials [82,83,98–100]. On the other hand, the degradation of battery separators during charge and discharge cycles, which is not directly related to capacity loss, has not been investigated that well.

Lithium-ion battery separators, typically made of polyolefin, such as polyethylene (PE), polypropylene (PP), or their combination, prevent contact between cathode and anode.[39] The failure of separators under abuse loading conditions will directly lead to internal short circuit and potential thermal run away. The mechanical properties of polymeric-based separators are temperature, loading rate and loading history dependent. During cycling of lithium-ion batteries in Electric Vehicles (EVs), besides charge-discharge, the battery components experience thermal and mechanical cycling as well. Therefore, there is a need to understand the extent of potential degradation of the separator under normal operating conditions in EVs.

In previous work, our research group has studied mechanical properties of various battery components taken out of fresh cells or before consumed in a cell [54,65,101]. In this chapter, the mechanical properties of separators from disassembled fresh cells and cells with various charge-discharge cycles were compared. The separators studied were dry-processed trilayer separators (PP-PE-PP). Uniaxial tensile tests and biaxial punch tests

were carried out. We found that separators from long cycled cells became significantly weaker under biaxial loading than that from fresh cells. This indicates adverse effects of aging. Lateral indentation of live cells shows that aged cells had smaller displacement and force to short circuit. Scanning electron microscope (SEM) images of cross sectional views of separators with different cycle numbers were compared as well. There was no significant change in the microstructure of the cycled separators. However, traces of particle deposits in the pores may explain the loss of strength. Infrared spectroscopy characterization of separators gives additional explanation about the potential aging mechanisms.

5.2 Experimental

The battery cells in this study had an elliptical shape and a nickel oxide chemistry. The dimensions were 64.8 mm by 37.2 mm by 19.1 mm and their nominal capacity was 5.3 Ah. The cells were fabricated at the same time and then cycled with 0.2 C discharge rate and 0.7 C charge rate under room temperature. Cells became inflated as they went under larger number of cycles. Figure 5-1 shows the comparison of cells with 0 and 1200 cycles. Cells underwent 0, 50, 100, 325 and 1200 cycles were used for the study. Separators of these five cells were extracted and washed with Dimethyl Carbonate (DMC). These separators with a thickness of 16 μm were dry-processed trilayer separators (PP-PE-PP). The color of separator changed for cells with higher cycles. For the cell with 1200 cycles, the separator was almost brown, as shown in Figure 5-2. Delamination of cathode and anode coatings were also observed for cells with higher cycles.

Uniaxial tensile specimens were prepared according to ASTM standard D882 for thin films, having a strip shape with a uniform width of 10 mm as explained in previous chapters. The strip specimen length was fixed as 60 mm and the gauge length was chosen as 35 mm. Following Sheidaei [13], to have enhanced precision for the width and improve quality of cut, a sharp razor was used to cut specimens while the separator was sandwiched between 5-mm Cartesian graph paper. The specimens were cut along machine direction (MD), transverse direction (TD) and diagonal direction (DD). An Instron 5944 uniaxial tensile machine with 100 N load cell and a constant 25 mm/min speed was used to perform the tests. Each test scenario was repeated five times.

Biaxial punch specimens with a diameter of 45 mm were cut by a hole puncher. The specimens were tightly fixed on a fixture with interior radius of 16 mm. Four Teflon hemispherical punch heads with diameters from 25.4 mm to 3.175 mm were used to apply the load, as shown in Figure 5-3. The tests were conducted by the same Instron machine and the loading speed was set to 12 mm/min. Each test scenario was repeated twice.

To investigate structural changes, Helios nanolab dual beam microscope with focused ion beam (FIB) was used to obtain cross sectional views of fresh and cycled separators along MD and TD. Additionally, energy-dispersive X-ray spectroscopy (EDS) was used to determine the chemical elements along the cross section. Between different sample preparation methods such as polishing the epoxy-impregnated sample, milling sample with ion beam cross section polisher and breaking of brittle separator sample in liquid nitrogen, FIB-SEM is found to be the best in terms of time and efforts of sample preparation and quality of final image. This method was also employed in available literature [102]. Thermo Fisher Fourier Transform Infrared (FTIR) microscope provided a comparison of polymer chain changes between separators from 0 cycled and 1200 cycled cells.

In addition to tests on separators, local indentation tests on full cells with 0 and 1200 cycles were conducted with a 12.5 mm steel hemispherical punch head and 1mm/min loading speed. Voltage of each cell was monitored during the tests. Tests stopped when a short circuit was detected from a drop in voltage.

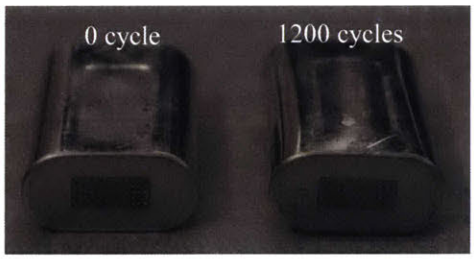


Figure 5-1 Volume change cycled cell compared with new cell

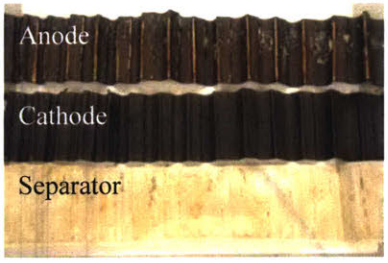


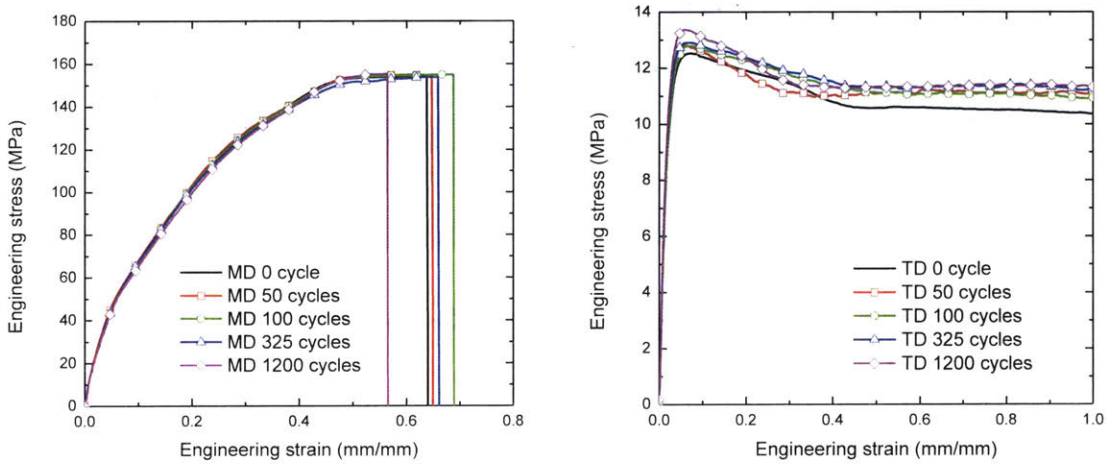
Figure 5-2 Battery components after 1200 cycles



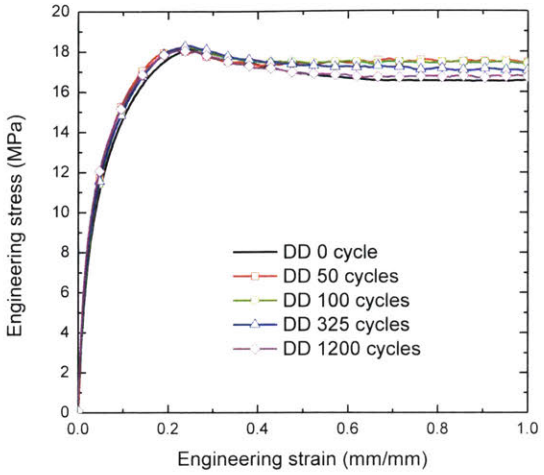
Figure 5-3 Punch test setup with a teflon punch head of 12.7 mm in diameter

5.3 Results and Discussion

Uniaxial tensile test results for separators with different cycles are shown in Figure 5-4. The stress-strain curves before failure in TD, MD, and DD did not show any noticeable differences. Therefore, the uniaxial tensile tests results indicate that the charge-discharge cycles did not influence the stress-strain curves of the separator. However, the failure strains in uniaxial tests are highly dependent on the cutting quality of strip specimens, and these tests cannot be used to comment on changes in failure strains. Biaxial tests that remove effects of edge imperfections were needed to check if failure strains have changed during cycling.



(a) (b)



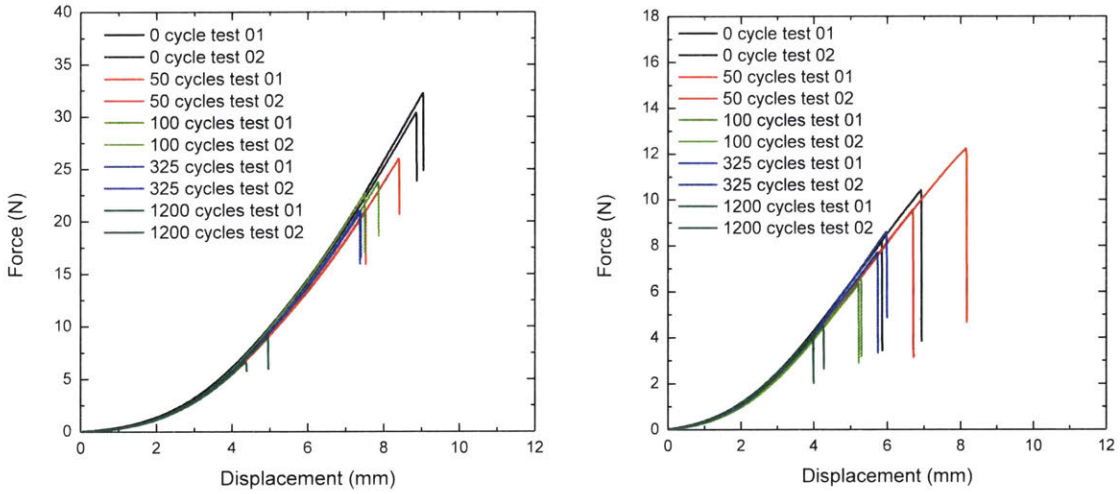
(c)

Figure 5-4 Engineering stress-strain curve of separators with different cycles in MD, TD and DD. (a) MD; (b) TD; (c) DD

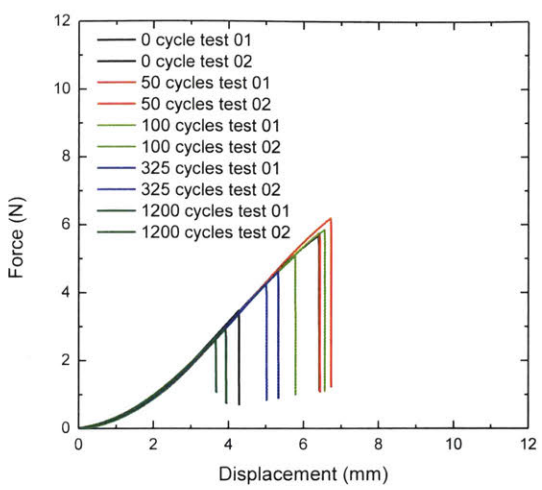
Figure 5-5a-d shows the biaxial loading test results with four punch heads. The evolution of the force-displacement curves is comparable, while the failure forces are much smaller for the separators with 1200 cycles. This shows the loss of puncture strength for the separators with high number of charge-discharge cycles. Figure 5-5e shows the failure force vs. cycle number curves for all four punch head sizes, where the failure forces were first averaged based on the two repeated tests and then normalized over the average force of separators with 0 cycle for better illustration. Although the failure force of separator with 50 and 100 cycles was scattered with different punch heads, the general trend is clear: with increasing cycle numbers, the separator became weaker under biaxial loading. Similar decrease of failure properties were also reported as the results of physical degradation of bulk PP [103,104].

Lateral indentation test results of two live cells with 0 and 1200 cycles are shown in Figure 5-6. The cell with 1200 cycles failed/shorted at a smaller force and displacement, which indicates the loss of puncture strength at separator level translates to a reduced tolerance to local indentation for high cycled batteries at cell level as well.

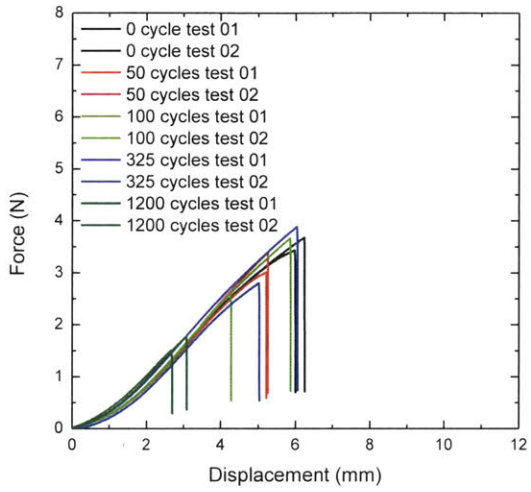
To understand the causes of degradation, possibly both physical and chemical aging, cross sectional views of the 16 μm thick separator prepared by FIB-SEM was used to check the changes in microstructure. Cross sections were investigated in three directions, on top surface, on a surface cut perpendicular to TD and another surface perpendicular to MD. Figure 5-7 shows the SEM pictures for a separator taken out of a fresh cell undergone 0 cycling. A three dimensional cube, made out of the three SEM pictures in each direction is shown in Figure 5-7a. Figures 5-7b shows the orientation of the bulk material and fibril sections on the top surface of separator (PP layer). Figures 5-7c and 5-7d show the cross-sectional views (top surface PP layer and central PE layer) of the separator on the surface perpendicular to TD.



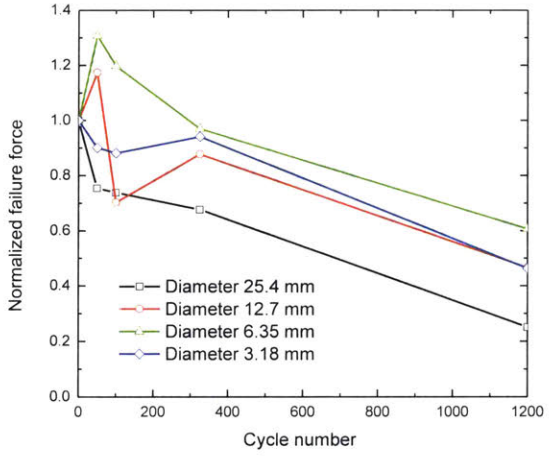
(a) (b)



(c)



(d)



(e)

Figure 5-5 Punch test results for separators with different punch size. (a) punch diameter: 25.4 mm; (b) punch diameter: 12.7 mm; (c) punch diameter: 6.4 mm; (d) punch diameter: 3.175 mm; (e) normalized failure force vs cycle number for different punch head sizes

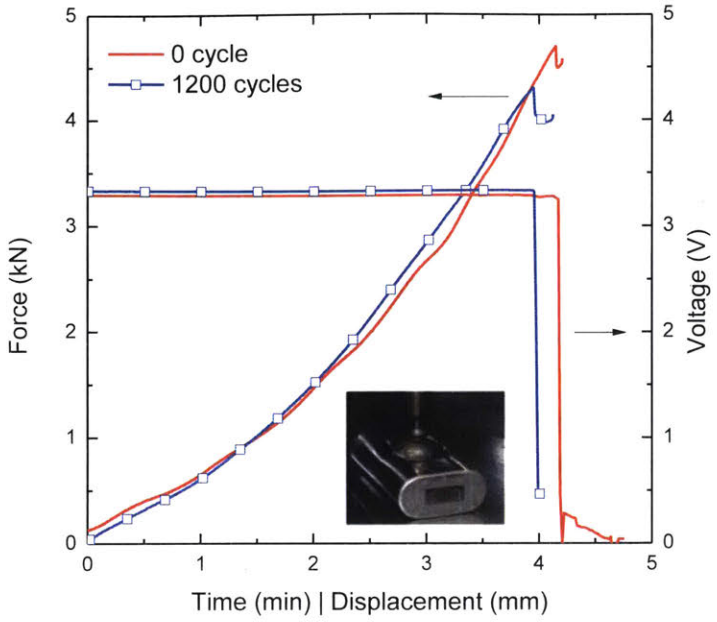


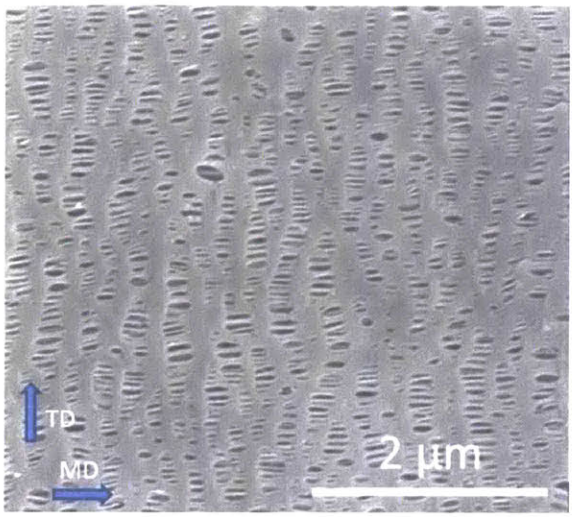
Figure 5-6 Lateral indentation results of cells with 0 and 1200 cycles

Figure 5-8 shows the SEM pictures of the separator from a 1200 cycled cell. No obvious structural change was seen from these cross-sectional SEM images of 1200 cycled separators as compared to the 0 cycled separator. The pattern and pore sizes of PP and PE layers remains similar between the separators from these two cell. However, particles, potentially chemical reaction products, were accumulated inside the pores of the 1200 cycled separator around the fibrils of PE layer, as seen in Figure 5-8a and magnified in circles in Figures 5-8c and 5-8d.

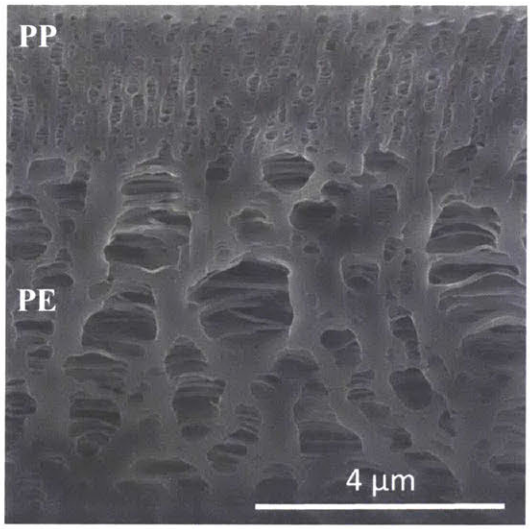
SEM/EDS analysis of the cross section of PE region showed that elements of nickel, oxygen and phosphorus were found in the cycled cell cross section. This may indicate potential chemical reactions between the active material of nickel and the electrolyte creates the chemical deposits seen in the pores of 1200 cycled separator.



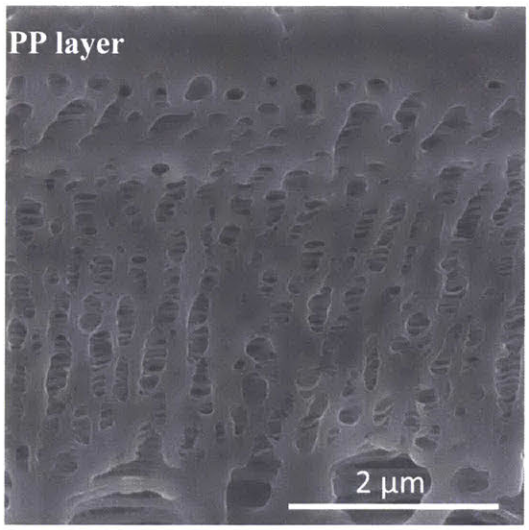
(a)



(b)

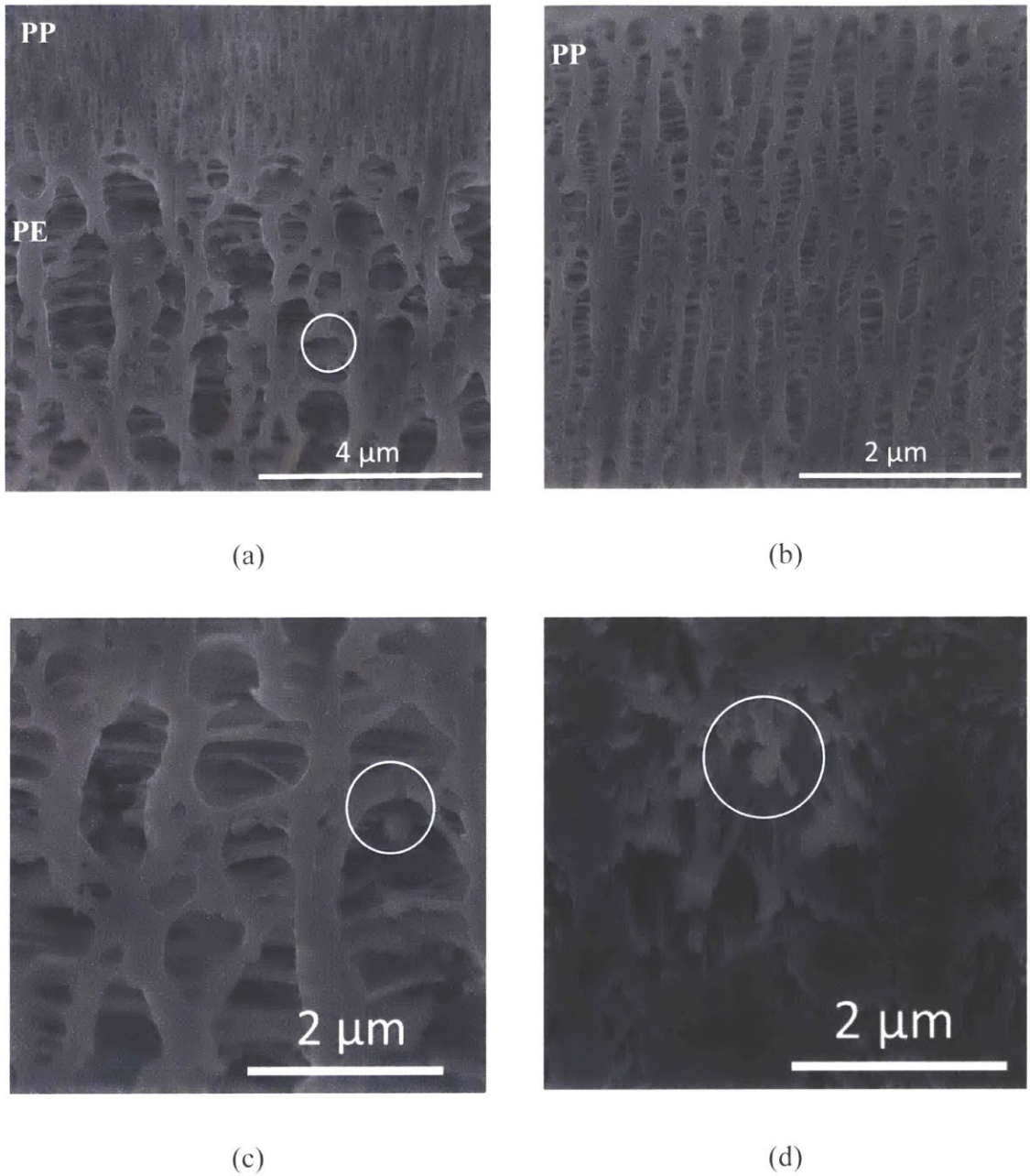


(c)



(d)

Figure 5-7 SEM pictures of a fresh (0 cycled) separator. (a) structure of a fresh (0 cycled) separator; (b) surface SEM of 0 cycled separator (PP layer); (c) cross-section view of PP and PE layer of 0 cycled separator along MD; (d) cross-section view of PP layer 0 cycle

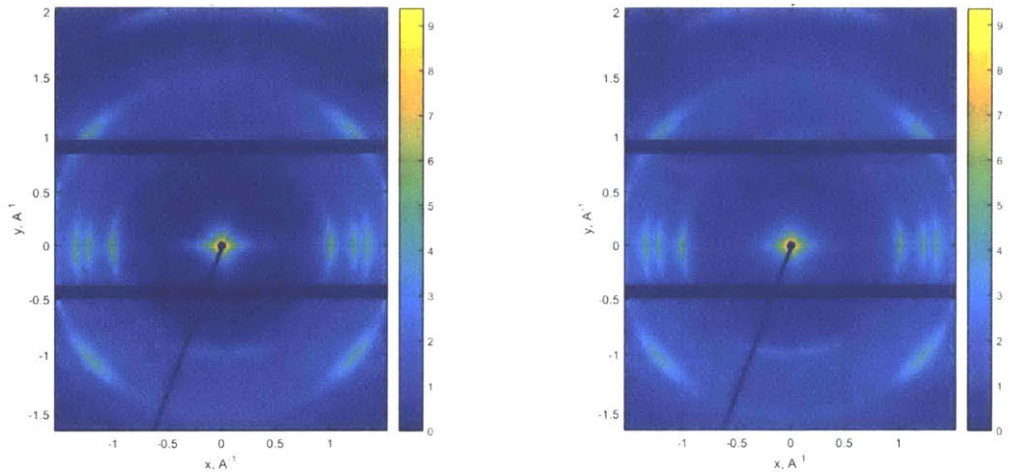


(a) (b)

(c) (d)

Figure 5-8 SEM picture of 0 and 1200 cycled separators. (a) cross-section view of PP and PE layer of 1200 cycled separator along MD; (b) cross-section view of PP layer 1200 cycled separator along MD; (c) cross-section view of PE layer of 1200 cycled separator along MD (particle in circle); (d) cross-section view of PE layer 1200 cycled separator along TD (particle in circle)

Wide angle XRD images in Figure 5-9 for separators with 0 and 1200 cycles indicate that there is no significant change in orientation of the crystalline structures due to charge-discharge cycles.



(a) (b)

Figure 5-9 Wide angle XRD images of (a) separator with 0 cycle and (b) separator with 1200 cycles

FTIR spectrum of fresh and cycled separator surfaces of both cathode and anode sides are shown in Figure 5-9. There is no significant change on the surface of either side between 0 and 1200 cycled separators. A slight increase of potential carbon-fluorine bonds signal is observed on the cathode side for the 1200 cycled separator (see the magnified section of figure between wavenumber 1300 to 900 cm^{-1}. After submerging 0 and 1200 cycled separators in DMC for three days, the above differences were almost disappeared, which hinted that the chemical degradation of polymer chain was not likely happening.

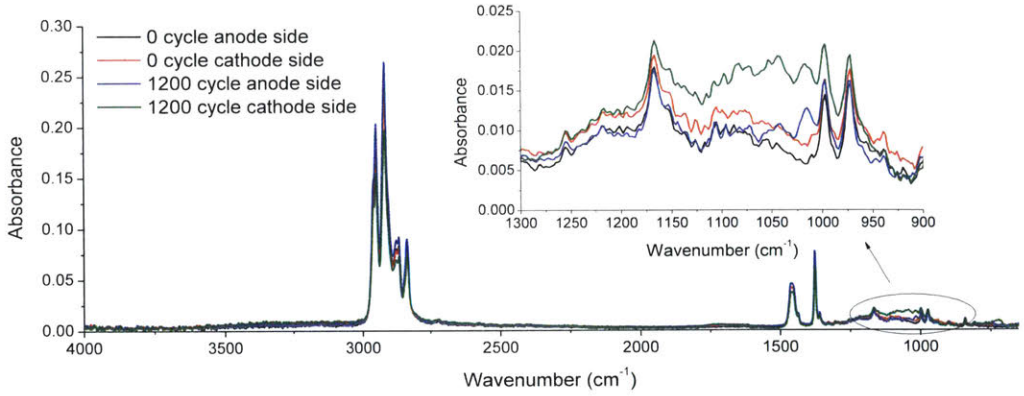


Figure 5-10 FTIR spectrum of 0 and 1200 cycled separators

5.4 Concluding Remarks

Several factors may influence the aging of lithium-ion battery separators, including temperature and mechanical loading hysteresis during charge and discharge cycles, chemical oxidation of polymer film, resistance increase due to accumulated chemical particles in the pores and the effect of electrolyte. Dry-processed trilayer separators (PP-PE-PP) from cells with five different charge-discharge cycles were tested under uniaxial and biaxial loading. It was found that the yield properties did not change between separators undergone different number of charge and discharge cycles. However, the failure properties under biaxial loading drop significantly for the separator with 1200 cycles. Cross-section view of separators indicated that the topology of fragments did not change. Therefore, mechanical deformation due to volume changes in charge and discharge cycles may not explain the loss of puncture strength. Meanwhile, the earlier failure of 1200 cycled separator may be explained by existence of chemical particles which were accumulated in the central PE layer. Additionally, FTIR spectrum suggested that no new chemical bonds were found on the surfaces and chemical aging was not likely to happen.

Chapter 6

Summary and Future Directions

6.1 Summary of main results

Test and modeling of 18650 shell casing: a comprehensive test and modeling practice for cylindrical shell casing has been developed. The shell casing contributes a large portion of mechanical resistance of 18650 cell subjected to different types of loading. The failure of battery separator and internal shorts could easily happen after the fracture of the shell casing. Unlike flat sheet metal, the axisymmetric nature of cylindrical cell makes it challenging to conduct various tests. In Chapter 2, dogbone specimens along axial, hoop and diagonal direction were cut from the flattened shell casing and used to calibrate the anisotropic plasticity properties (height: 65 mm, diameter: 18 mm, thickness: 0.26 mm). The potential damage due to this flatten process was also studied by cutting dogbone specimen directly from shell casing without flattening. Tests on notched specimens, central hole, plane strain, biaxial and shear specimens were conducted for calibration of the fracture model. Hill's 48 plasticity and modified Mohr-Coulomb (MMC) fracture model of the shell casing were then developed. The MMC facture model considers the stress triaxiality dependent fracture strain which is more accurate than constant failure strain used in literature. Three validation study of the shell casing model were conducted at shell casing level: axial and lateral compression, three-point bending and hydraulic bulge test. Experiments at the battery cell level was also performed with the homogenized jellyroll model. A good match between test and simulation indicates the predictability of the developed model and was demonstrated to prove the applicability of our advance model for battery cell mechanical abuse loading.

Test procedure in determining separator mechanical properties: four different types of commonly used battery separator: dry-processed separator, dry-processed trilayer separator, wet-processed ceramic-coated separator and nonwoven separator, were tested

and compared. Specimen width study of strip specimen for uniaxial tensile test shows that strip width larger than 10 mm could yield consistent results when the gauge length is 35 mm. The out-of-plane compression tests with 40 layer stacked separators shows the different properties between dry and wet-processed separators where the former became oval shape and later remains round after test. Through punch tests, two different failure modes were found for dry-processed separators, which gives insight about the scattered results in the nail penetration or small punch test of cell. Tests with Mode A failure lead to rapid thermal event while repeat tests with Mode B failure can be much less eventful. Based on test observation, a criterion for displacements that a separator can tolerate without having a soft failure was proposed. It could be used to design cell manufacturing procedures or battery protective structures while keeping in mind level of tolerance of the separator associated with a soft short.

Deformation sequence of micro fibrils and lamellae in PP separator: comprehensive characterization of PP separator provides very detailed information. The temperature and strain-rate dependent properties from uniaxial tensile test under different temperature and loading speeds give the inputs for later numerical modeling. Wide and small angle X-ray scattering shows that several crystalline planes are orientating along MD. SEM micrograph from interrupted test along MD, TD and DD give the deformation sequences of the micro fibrils and lamellae. There were fragmentation/crazing in the lamellae which shows generation of new elliptical pores during MD tension. While TD tension gives very different deformation of the lamellae and fibrils. The lamellae became narrow and there were rotation of the fibrils followed. The separation/split of lamellae blocks and their rotation were found and localization in several regions and specimens indicates the two direction deformation during DD loading, such as MD shear and TD tension. The 2D and 3D reconstruction of the PP separator suggested that the material anisotropy dominates the high anisotropic properties along MD and TD when structural anisotropy contributes relatively less.

Numerical model of PP separator was developed in LSDYNA with LSDYNA's modified anisotropic honeycomb model since the separator is porous and highly anisotropic. The model was shown to predict the response of the separator under different loading conditions.

Degradation of dry-processed trilayer separator due to charge and discharge cycles: dry-processed trilayer (PP-PE-PP) separators extracted from prismatic cells with five different charge-discharge cycles were tested. The mechanical properties under uniaxial tension of different cycled separators did not show much differences while the failure displacement of cycled separators under punch test decreased a lot which gives the sign of charge-discharge induced degradation. Cross section view of the separator shows that no distinguishable morphology was found, such as length and diameter of the fibrils. However, some chemical reaction products were found in the central PP layer of the separator which is also a sign of degradation (not mechanical degradation). FTIR spectrum suggested no change of chemical bonds on the separator surfaces and chemical aging may not happen.

6.2 Future research

Lithium-ion batteries that consisted of different components with completely different types of materials and the length scale of in-plane and out-of-plane are 3 orders of magnitude in different, one in mm and the other in micrometer, makes that test and modeling a challenging topic. There are complex couplings between mechanical, thermal and electrochemical properties of the cell during model charge-discharge operation and abuse loading. From mechanical test and modeling point of view, there are several issues worth careful study.

6.2.1 Numerical modeling of the separator with other types of modeling strategy

The modeling of the separator that made from different processes should be done with different treatment. Constitutive models with compressible and anisotropic properties as well as strain rate and temperature dependent could bring dozens of parameters which makes its engineering application difficult. The foam model that was adapted in this thesis has limitations. For example, it would not be predict the oval shape specimen under compression since it assumes zero Poisson's ratio. Another assumption in this model is uncoupled yield and flow rule in different principal directions. A simple but effective model is still needed and welcome. The effect of ceramic coating may be also important for these ceramic-coated separators for their modeling.

6.2.2 Test and modeling of electrodes

The separator and shell casing could not stay alone to capture the mechanical properties of cell without accurate model of the electrode. The electrodes contain double coatings and current collector, either aluminum or copper foil as shown in Figure 1-4. The test and modeling of foils and coatings are also challenging due to their thin nature and the difficulties to obtain a pure layer of coating without damaging.

6.2.3 Coupling of thermal and electrochemical properties

The ultimate goal of this practice is to predict the mechanical properties of lithium-ion batteries in all kinds of operating environment. Thus, the thermal and electrochemical properties and their couplings are important to the numerical model. Researchers are in the process of adding these features in multi-physics software. However, with lots of fitted parameters, the models are still struggling to predict "new" tests. This is an emerging area that needs great efforts.

6.2.4 Solid state battery study

The energy density of conventional liquid electrolyte lithium-ion battery is being pushed closed to its limit. The next generation of lithium battery for electric vehicle is under investigation by both universities and startups. The solid state battery is one of the most promising next generation cells for large consumer electronics. The nonflammable solid electrolyte works also as separators, will significantly improve the mechanical safety of lithium cells. With the careful design of the cell, it is possible to use the battery cell as structural components in EV and energy absorption components, which will bring the design of EV to a new era.

Bibliography

1. Tarascon, J. M. & Armand, M. Issues and challenges facing rechargeable lithium batteries. *Nature* **414,** 359–67 (2001).
2. Armand, M. & Tarascon, J.-M. Building better batteries. *Nature* **451,** 652–657 (2008).
3. Nishi, Y. Lithium ion secondary batteries; past 10 years and the future. *J. Power Sources* **100,** 101–106 (2001).
4. International Energy Agency. *Global EV Outlook 2016 Electric Vehicles Initiative. Iea* (2016).
5. Du, J. & Ouyang, D. Progress of Chinese electric vehicles industrialization in 2015: A review. *Appl. Energy* **188,** 529–546 (2017).
6. MacDonald, J. & Finance, B. N. E. Electric vehicles to be 35% of global new car sales by 2040. *Bloom. New Energy Financ. Press release, Feb* **25,** (2016).
7. Smith, B. Chevrolet Volt Battery Incident Overview Report. *US Dep. Transp. Natl. Highw. Traffic Saf. Adm.* **1,** 1 (2012).
8. Wierzbicki, T. & Sahraei, E. Homogenized mechanical properties for the jellyroll of cylindrical Lithium-ion cells. *J. Power Sources* **241,** 467–476 (2013).
9. Sahraei, E., Campbell, J. & Wierzbicki, T. Modeling and short circuit detection of 18650 Li-ion cells under mechanical abuse conditions. *J. Power Sources* **220,** 360–372 (2012).
10. Sahraei, E., Kahn, M., Meier, J. & Tomasz, W. Modelling of cracks developed in lithium-ion cells under mechanical loading. *RSC Adv.* **5,** 80369–80380 (2015).
11. Cannarella, J. & Arnold, C. B. State of health and charge measurements in lithium-ion batteries using mechanical stress. *J. Power Sources* **269,** 7–14 (2014).
12. Gor, G. Y., Cannarella, J., Prévost, J. H. & Arnold, C. B. A model for the behavior of battery separators in compression at different strain/charge rates. *J. Electrochem. Soc.* **161,** F3065--F3071 (2014).

13. Sheidaei, A., Xiao, X., Huang, X. & Hitt, J. Mechanical behavior of a battery separator in electrolyte solutions. *J. Power Sources* **196,** 8728–8734 (2011).

14. Shi, D., Xiao, X., Huang, X. & Kia, H. Modeling stresses in the separator of a pouch lithium-ion cell. *J. Power Sources* **196,** 8129–8139 (2011).

15. Lai, W.-J., Ali, M. Y. & Pan, J. Mechanical behavior of representative volume elements of lithium-ion battery cells under compressive loading conditions. *J. Power Sources* **245,** 609–623 (2014).

16. Ali, M. Y., Lai, W.-J. & Pan, J. Computational models for simulations of lithium-ion battery cells under constrained compression tests. *J. Power Sources* **242,** 325–340 (2013).

17. Meier, J. D. Material characterization of high-voltage lithium-ion battery models for crashworthiness analysis. (Cambridge, Massachussetts, Massachussetts Institute of Technology, 2013).

18. Xu, J., Liu, B., Wang, X. & Hu, D. Computational model of 18650 lithium-ion battery with coupled strain rate and SOC dependencies. *Appl. Energy* **172,** 180–189 (2016).

19. McClintock, F. A. A Criterion for Ductile Fracture by the Growth of Holes. *J. Appl. Mech.* **35,** 363–371 (1968).

20. Rice, J. R. & Tracey, D. M. On the ductile enlargement of voids in triaxial stress fields. *J. Mech. Phys. Solids* **17,** 201–217 (1969).

21. Gurson, A. L. Continuum theory of ductile rupture by void nucleation and growth: Part I: Yield criteria and flow rules for porous ductile media. *J. Eng. Mater. Technol.* **99,** 2–15 (1977).

22. Tvergaard, V. & Needleman, A. Analysis of the cup-cone fracture in a round tensile bar. *Acta Metall.* **32,** 157–169 (1984).

23. Nahshon, K. & Hutchinson, J. W. Modification of the Gurson Model for shear failure. *Eur. J. Mech. - A/Solids* **27,** 1–17 (2008).

24. Ghahremaninezhad, A. & Ravi-Chandar, K. Ductile failure behavior of

polycrystalline Al 6061-T6 under shear dominant loading. *Int. J. Fract.* **180,** 23–39 (2013).

25. Bao, Y. & Wierzbicki, T. On fracture locus in the equivalent strain and stress triaxiality space. *Int. J. Mech. Sci.* **46,** 81–98 (2004).

26. Xue, L. Damage accumulation and fracture initiation in uncracked ductile solids subject to triaxial loading. *Int. J. Solids Struct.* **44,** 5163–5181 (2007).

27. Bai, Y. & Wierzbicki, T. Application of extended Mohr--Coulomb criterion to ductile fracture. *Int. J. Fract.* **161,** 1–20 (2010).

28. Johnson, G. R. & Cook, W. H. Fracture characteristics of three metals subjected to various strains, strain rates, temperatures and pressures. *Eng. Fract. Mech.* **21,** 31–48 (1985).

29. Dunand, M. & Mohr, D. On the predictive capabilities of the shear modified Gurson and the modified Mohr–Coulomb fracture models over a wide range of stress triaxialities and Lode angles. *J. Mech. Phys. Solids* **59,** 1374–1394 (2011).

30. Bai, Y. & Wierzbicki, T. A comparative study of three groups of ductile fracture loci in the 3D space. *Eng. Fract. Mech.* **135,** 147–167 (2015).

31. Wang, K., Luo, M. & Wierzbicki, T. Experiments and modeling of edge fracture for an AHSS sheet. *Int. J. Fract.* **187,** 245–268 (2014).

32. Pack, K., Luo, M. & Wierzbicki, T. Sandia Fracture Challenge: blind prediction and full calibration to enhance fracture predictability. *Int. J. Fract.* **186,** 155–175 (2014).

33. Mohr, D. & Marcadet, S. J. Micromechanically-motivated phenomenological Hosford-Coulomb model for predicting ductile fracture initiation at low stress triaxialities. *Int. J. Solids Struct.* **67–68,** 40–55 (2015).

34. Roth, C. C. & Mohr, D. Ductile fracture experiments with locally proportional loading histories. *Int. J. Plast.* **79,** 328–354 (2015).

35. Luo, M., Li, Y., Gerlach, J. & Wierzbicki, T. Prediction of Shear-induced Crack Initiation in AHSS Deep Drawing Operation with a Phenomenological Fracture

Model. in *NUMIFORM 2010: Proceedings of the 10th International Conference on Numerical Methods in Industrial Forming Processes Dedicated to Professor OC Zienkiewicz (1921--2009)* **1252,** 464–472 (2010).

36. Luo, M. & Wierzbicki, T. Numerical failure analysis of a stretch-bending test on dual-phase steel sheets using a phenomenological fracture model. *Int. J. Solids Struct.* **47,** 3084–3102 (2010).

37. Baldwin, R. S., Bennet, W. R., Wong, E. K., Lewton, M. R. & Harris, M. K. Battery Separator Characterization and Evaluation Procedures for NASA's Advanced Lithium-Ion Batteries. (2010).

38. Huang, X. Separator technologies for lithium-ion batteries. *J. Solid State Electrochem.* **15,** 649–662 (2011).

39. Arora, P. & Zhang, Z. Battery separators. *Chem. Rev.* **104,** 4419–4462 (2004).

40. Lee, H., Yanilmaz, M., Toprakci, O., Fu, K. & Zhang, X. A review of recent developments in membrane separators for rechargeable lithium-ion batteries. *Energy Environ. Sci.* **7,** 3857–3886 (2014).

41. Zhang, S. S. A review on the separators of liquid electrolyte Li-ion batteries. *J. Power Sources* **164,** 351–364 (2007).

42. Isaacson, R. B. & Bierenbaum, H. S. Process for preparing microporous film. (1971).

43. Hay, I., Bierenbaum, H., Daley, L. & Zimmerman, D. Process for preparing a thermoplastic microporous film involving a cold stretching step and multiple hot stretching steps. (1974).

44. Jacoby, P. & Bauer, C. W. Oriented porous polypropylene films. (1990). at <US4975469>

45. Druin, M., Loft, J. & Plovan, S. Novel open-celled microporous film. (1974).

46. Call, R. W. *et al.* Multilayer separator exhibiting improved strength and stability. (2013).

47. Tabatabaei, S. H., Carreau, P. J. & Ajji, A. Microporous membranes obtained from

PP/HDPE multilayer films by stretching. *J. Memb. Sci.* **345,** 148–159 (2009).

48. Zhang, X. *et al.* Biaxially oriented porous membranes, composites, and methods of manufacture and use. (2011).

49. Zhang, Z. *et al.* Separator memberanes for lithium ion battery and related methods. (2014). doi:US 2013/0154292 A1

50. Zhang, Z. *et al.* Coated separators for lithium batteries and related methods. (2016).

51. Huang, X. & Hitt, J. Lithium ion battery separators: Development and performance characterization of a composite membrane. *J. Memb. Sci.* **425–426,** 163–168 (2013).

52. Huang, X. Development and characterization of a bilayer separator for lithium ion batteries. *J. Power Sources* **196,** 4 (2011).

53. Doughty, D. H. *SAE J2464 EV & HEV Rechargeable Energy Storage System (RESS) Safety and Abuse Testing Procedure.* (2010).

54. Sahraei, E., Hill, R. & Wierzbicki, T. Calibration and finite element simulation of pouch lithium-ion batteries for mechanical integrity. *J. Power Sources* **201,** 307–321 (2012).

55. Greve, L. & Fehrenbach, C. Mechanical testing and macro-mechanical finite element simulation of the deformation, fracture, and short circuit initiation of cylindrical Lithium ion battery cells. *J. Power Sources* **214,** 377–385 (2012).

56. Sahraei, E., Wierzbicki, T., Hill, R. & Luo, M. Crash Safety of Lithium-Ion Batteries Towards Development of a Computational Model. (2010). doi:10.4271/2010-01-1078

57. Xia, Y., Wierzbicki, T., Sahraei, E. & Zhang, X. Damage of cells and battery packs due to ground impact. *J. Power Sources* **267,** 78–97 (2014).

58. Bai, Y. & Wierzbicki, T. A new model of metal plasticity and fracture with pressure and Lode dependence. *Int. J. Plast.* **24,** 1071–1096 (2008).

59. Dunand, M. & Mohr, D. Hybrid experimental--numerical analysis of basic ductile

fracture experiments for sheet metals. *Int. J. Solids Struct.* **47,** 1130–1143 (2010).

60. Kim, S.-H., Kim, S.-H. & Huh, H. Design modification in a multi-stage rectangular cup drawing process with a large aspect ratio by an elasto-plastic finite element analysis. *J. Mater. Process. Technol.* **113,** 766–773 (2001).

61. Wang, K., Greve, L. & Wierzbicki, T. FE simulation of edge fracture considering pre-damage from blanking process. *Int. J. Solids Struct.* **71,** 206–218 (2015).

62. Luo, M., Dunand, M. & Mohr, D. Experiments and modeling of anisotropic aluminum extrusions under multi-axial loading--Part II: Ductile fracture. *Int. J. Plast.* **32,** 36–58 (2012).

63. Reyes, A., Eriksson, M., Lademo, O.-G., Hopperstad, O. S. & Langseth, M. Assessment of yield and fracture criteria using shear and bending tests. *Mater. Des.* **30,** 596–608 (2009).

64. Abaqus, V. 6.10. *User subroutines Ref. Man.* (2010).

65. Sahraei, E., Kahn, M., Meier, J. & Wierzbicki, T. Modelling of cracks developed in lithium-ion cells under mechanical loading. *RSC Adv.* (2015).

66. Sahraei, E., Meier, J. & Wierzbicki, T. Characterizing and modeling mechanical properties and onset of short circuit for three types of lithium-ion pouch cells. *J. Power Sources* **247,** 503–516 (2014).

67. Meier, J. D., Sahraei, E., Salk, M., Kisters, T. & Huberth, F. State of Charge vs . Thermal Runaway for Lithium Ion Large Pouch Cells. in *Battery Congress* (2013).

68. Feng, X. *et al.* Characterization of penetration induced thermal runaway propagation process within a large format lithium ion battery module. *J. Power Sources* **275,** 261–273 (2015).

69. Troffkin, H., Rein, B., Spotnitz, R., Giovannoni, R. & Guo, Y. United States Patent [191. (1993).

70. Lin, Y. *et al.* A semi-quantitative deformation model for pore formation in isotactic polypropylene microporous membrane. *Polym. (United Kingdom)* **80,** 214–227 (2015).

71. Bierenbaum, H., Daley, L., Zimmerman, D. & Hay, I. Process for preparing a thermoplastic microporous film involving a cold stretching step and multiple hot stretching steps. (1974).

72. Xue, Z., Zhang, Z. & Zhang, S. S. Rechargeable Batteries. 337–352 (2015). doi:10.1007/978-3-319-15458-9

73. Wang, S., Saffar, A., Ajji, A., Wu, H. & Guo, S. Fabrication of microporous membranes from melt extruded polypropylene precursor films via stretching: Effect of annealing. *Chinese J. Polym. Sci.* **33,** 1028–1037 (2015).

74. Huang, X. Separator technologies for lithium-ion batteries. *J. Solid State Electrochem.* **15,** 649–662 (2011).

75. Friedl, N., Rammerstorfer, F. G. & Fischer, F. D. Buckling of stretched strips. *Comput. Struct.* **78,** 185–190 (2000).

76. Cannarella, J. *et al.* Mechanical Properties of a Battery Separator under Compression and Tension. *J. Electrochem. Soc.* **161,** F3117–F3122 (2014).

77. A123 Systems. Battery Pack Design , Validation , and Assembly Guide using A123 Systems AMP20M1HD-A Nanophosphate Cells. 1–71 (2014). at <http://www.formula-hybrid.org/wp-content/uploads/A123_AMP20_battery_Design_guide.pdf>

78. ASTM. F1306 − 90 Standard Test Method for Slow Rate Penetration Resistance of Flexible Barrier Films and Laminates. (2008).

79. Deimede, V. & Elmasides, C. Separators for Lithium-Ion Batteries: A Review on the Production Processes and Recent Developments. *Energy Technol.* n/a-n/a (2015). doi:10.1002/ente.201402215

80. Yuzawa, K., Yang, Y., Bhandari, N., Sugiyama, M. & Nakamura, S. Charging the future: Asia leads drive to next-generation EV battery market. *Goldman Sachs Equity Res.* 59 (2016).

81. Qi, H. J. & Boyce, M. C. Stress-strain behavior of thermoplastic polyurethanes. *Mech. Mater.* **37,** 817–839 (2005).

82. Broussely, M. *et al.* Main aging mechanisms in Li ion batteries. *J. Power Sources* **146,** 90–96 (2005).

83. Sarre, G., Blanchard, P. & Broussely, M. Aging of lithium-ion batteries. *J. Power Sources* **127,** 65–71 (2004).

84. Pannala, S. *et al.* Multiscale modeling and characterization for performance and safety of lithium-ion batteries. *J. Appl. Phys.* **118,** (2015).

85. Wen, J., Yu, Y. & Chen, C. A review on lithium-ion batteries safety issues: existing problems and possible solutions. *Mater. Express* **2,** 197–212 (2012).

86. Jeon, D. H. & Baek, S. M. Thermal modeling of cylindrical lithium ion battery during discharge cycle. *Energy Convers. Manag.* **52,** 2973–2981 (2011).

87. Shah, K., Vishwakarma, V. & Jain, A. Measurement of Multiscale Thermal Transport Phenomena in Li-ion Cells: A Review. *J. Electrochem. Energy Convers. Storage* **13,** (2016).

88. Xu, J., Wang, L., Guan, J. & Yin, S. Coupled effect of strain rate and solvent on dynamic mechanical behaviors of separators in lithium ion batteries. *Mater. Des.* **95,** 319–328 (2016).

89. Stuart, B. *Infrared spectroscopy*. (Wiley Online Library, 2005).

90. Luongo, J. P. Infrared study of polypropylene. *J. Appl. Polym. Sci.* **3,** 302–309 (1960).

91. Love, C. T. Thermomechanical analysis and durability of commercial micro-porous polymer Li-ion battery separators. *J. Power Sources* **196,** 2905–2912 (2011).

92. Cser, F. About the Lorentz correction used in the interpretation of small angle X-ray scattering data of semicrystalline polymers. *J. Appl. Polym. Sci.* **80,** 2300–2308 (2001).

93. Goldstein, J. *et al. Scanning electron microscopy and X-ray microanalysis: a text for biologists, materials scientists, and geologists*. (Springer Science & Business Media, 2012).

94. Wu, T., Xiang, M., Cao, Y., Kang, J. & Yang, F. Influence of lamellar structure on double yield behavior and pore size distribution in β nucleated polypropylene stretched membranes. *RSC Adv.* **4,** 43012–43023 (2014).

95. Chen, J., Yan, Y., Sun, T., Qi, Y. & Li, X. Deformation and fracture behaviors of microporous polymer separators for lithium ion batteries. *RSC Adv.* **4,** 14904–14914 (2014).

96. Amir Saffar Pierre J. Carreau, A. A. & Kamal, M. R. Influence of Stretching on the Performance of Polypropylene-Based Microporous Membranes. *Am. Chem. Soc.* **53,** 8 (2014).

97. Argon, A. S. *The physics of deformation and fracture of polymers*. (Cambridge University Press, 2013).

98. Agubra, V. & Fergus, J. Lithium Ion Battery Anode Aging Mechanisms. *Materials (Basel).* **6,** 16 (2013).

99. Vetter, J. *et al.* Ageing mechanisms in lithium-ion batteries. *J. Power Sources* **147,** 269–281 (2005).

100. Ebner, M., Marone, F., Stampanoni, M. & Wood, V. Visualization and Quantification of Electrochemical and Mechanical Degradation in Li Ion Batteries. *Sceince* **342,** 716–721 (2013).

101. Sahraei, E., Bosco, E., Dixon, B. & Lai, B. Microscale failure mechanisms leading to internal short circuit in Li-ion batteries under complex loading scenarios. *J. Power Sources* **319,** 56–65 (2016).

102. Lagadec, M. F., Ebner, M., Zahn, R. & Wood, V. Communication—Technique for Visualization and Quantification of Lithium-Ion Battery Separator Microstructure. *J. Electrochem. Soc.* **163,** A992–A994 (2016).

103. Vu-Khanh, T. & El Majdoubi, M. Entropy change with yielding and fracture of polypropylene. *Theor. Appl. Fract. Mech.* **51,** 111–116 (2009).

104. Hutchinson, J. M., Smith, S., Horne, B. & Gourlay, G. M. Physical aging of polycarbonate: enthalpy relaxation, creep response, and yielding behavior. *Macromolecules* **32,** 5046–5061 (1999).